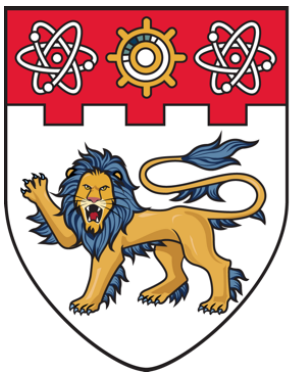

NANYANG TECHNOLOGICAL UNIVERSITY
SINGAPORE

FLEXIBLE TACTILE SENSORS FOR IN-SITU QUANTIFYING OBJECT FEATURES

TU JIAQI

SCHOOL OF MATERIALS SCIENCE AND ENGINEERING

2024

FLEXIBLE TACTILE SENSORS FOR IN-SITU QUANTIFYING OBJECT FEATURES

TU JIAQI

SCHOOL OF MATERIALS SCIENCE AND ENGINEERING

A thesis submitted to the Nanyang Technological University
in partial fulfilment of the requirement for the degree of
Doctor of Philosophy

2024

Statement of Originality

I hereby certify that the work embodied in this thesis is the result of original research, is free of plagiarised materials, and has not been submitted for a higher degree to any other University or Institution.

2 Aug 2024

. . . . . .

Date

. . . . . .

Tu Jiaqi

Supervisor Declaration Statement

I have reviewed the content and presentation style of this thesis and declare it is free of plagiarism and of sufficient grammatical clarity to be examined. To the best of my knowledge, the research and writing are those of the candidate except as acknowledged in the Author Attribution Statement. I confirm that the investigations were conducted in accord with the ethics policies and integrity standards of Nanyang Technological University and that the research data are presented honestly and without prejudice.

2 Aug 2024

. . . . . .

Date

. . . . . .

Prof. Chen Xiaodong

Authorship Attribution Statement

(B) This thesis contains material from 2 papers published in the following peer-reviewed journal(s) / from papers accepted at conferences in which I am listed as an author.

Chapter 4 is published as Jiaqi Tu, Zheren Cai, Zhihua Liu, Jiangtao Su, Yanzhen Li, Xue Feng, Zequn Cui, Xiaodong Chen. Quantitative Tactile Sensing of Surface Microstructures Through Time-Domain Analysis of Piezoelectric Twin Signals. Advanced Materials e10393 (2025). DOI: 10.1002/adma.202510393.

The contributions of the co-authors are as follows:

- X.C., Z.Q.C., and J.T. conceived the idea.
- J.T. and Z.Q.C. designed the work and developed the tactile profiling method for surface microstructures.
- Z.R.C. and J.T. performed finite element analysis.
- Z.L. constructed the test ing platform.
- J.T., J.S., Y.L., and Z.Q.C. prepared sensors with testing samples and carried out tests. J.T., X.F., Z.Q.C., and X.C. composed the paper.
- All authors discussed the results and commented on the manuscript. X.C. and X.F. supervised the work.

Chapter 5 is published as Jiaqi Tu, Ming Wang, Wenlong Li, Jiangtao Su, Yanzhen Li, Zhisheng Lv, Haicheng Li, Xue Feng, Xiaodong Chen. Electronic skins with multimodal sensing and perception. *Soft Sci* 3:25 (2023). DOI: 10.20517/ss.2023.15.

The contributions of the co-authors are as follows:

- Conceptualization: Tu J, Wang M
- Methodology: Tu J, Wang M

- Writing - Original Draft: Tu J, Wang M
- Writing - Review & Editing: Li W, Su J, Li Y, Lv Z, Li H, Feng X, Chen X
- Supervision: Feng X, Chen X

2 Aug 2024

. . . .

Date

TuJiaqi

. . . .

Tu Jiaqi

Abstract

Tactile, the perception of human touch, is a complex and multifaceted sensory experience crucial for daily interactions and communication. Researchers have been developing tactile sensing technology that imitates human skin, aiming to precisely measure and analyze physical properties like size, shape, texture, and hardness. Replicating this intricate sensory process in artificial systems and extending biological tactile senses holds significant potential, particularly in quantitative object sensing. Artificial tactile systems are especially useful in fields like robotics and healthcare, where precise data about textures and object characteristics can significantly impact performance and diagnosis. Quantitative object sensing enhances machines' capability to perform delicate and precise tasks, improves the accuracy of medical assessments, and enriches the realism of virtual environments. Advancements in this technology are essential for the future of robotics, medical diagnostics, and virtual reality. This thesis underscores the importance of bridging the gap between human tactile perception and artificial sensing technologies to drive innovation and improve various applications. New approaches are explored here to enhance how we sense and interpret textures and objects using advanced technology.

The research focuses on two main innovations: The first hypothesis is dynamic force sensing for in-situ measurement of micro-scale surface profile: These sensors can detect textures by measuring vibrations. This technology allows for a more detailed and accurate analysis of different surfaces. The second hypothesis is a tactile system for in-situ quantifying object features. In which, gloves are equipped with a dense array of pressure sensors can measure object characteristics, such as size and softness, with high precision. This system haw significant potential for quantitative medical diagnostics, offering a non-invasive way to detect abnormalities. The research also includes the development of a piezoelectric tactile sensor, which provides detailed 3D reconstruction of micro-scale textures without the need for controlled scanning speeds. Additionally, simulations of the piezoelectric tactile sensor’s mechanisms were conducted to better understand how it works and to validate its effectiveness. Overall, this thesis presents significant

advancements in touch-based technology, paving the way for improved object recognition and medical diagnostics.

Lay Summary

This thesis explores innovative advancements in tactile sensing technology aimed at enhancing the precision and versatility of texture and object recognition through touch-based feedback systems. The research introduces two key technological innovations:

Piezoelectric tactile Sensors: These sensors are developed to characterize textures by detecting vibrations induced by varying surface properties. Unlike conventional methods that depend on steady speeds, these piezoelectric sensors function effectively across a range of speeds, making them adaptable to real-world conditions. The sensors' ability to capture variations in vibration frequency and amplitude enables detailed and accurate surface analysis, providing a more nuanced understanding of different textures.

Pressure-Sensing Gloves: The research includes the design and fabrication of gloves embedded with a dense array of 142 pressure sensors. These gloves are capable of precise measurements of object characteristics such as size, shape, and softness. The high sensor density improves the system's accuracy, which is particularly beneficial for medical diagnostics. This non-invasive approach allows for the detailed assessment of tissue properties and the detection of abnormalities, offering a significant advancement in healthcare technology.

A notable contribution of this research is the development of the piezoelectric tactile sensor. The sensor provides detailed three-dimensional imaging of surface textures without the need for controlled scanning speeds. This technology enables high-resolution texture analysis, making it suitable for applications in fields such as robotics and material science. The research also includes simulations of the piezoelectric sensor’s mechanisms to validate its effectiveness and to provide a deeper understanding of its operational principles.

Overall, this thesis presents significant advancements in tactile sensing technologies, offering new solutions for accurate object recognition and enhanced medical diagnostics.

The innovative approaches and findings contribute to the development of more effective tools for real-time, non-invasive assessments of textures and object properties.

Acknowledgements

This dissertation was made possible through funding from the Postgraduate Programme Funding Agreement in Flexible Electronics Technology (NTU Ref: REQ0131578), a collaboration between the Institute of Flexible Electronics Technology of Tsinghua, Zhejiang (IFET-THU), NTU, and the Collaborative Innovation Center for Flexible Electronics Technology, China (CICFE).

I extend my sincere gratitude to my research project supervisors, Professor Chen Xiaodong, for their unwavering guidance and support. I am also thankful to my Thesis Advisory Committee (TAC) members and co-supervisor, Professor Feng Xue, for their valuable insights and contributions.

Special thanks go to Dr. Cui Zequn, Dr. Xia Huarong, Dr. Liu Zhihua, Dr. Cai Zheren, Dr. Wang Ming, Mr. Su Jiangtao, and Mr. Li Yanzhen for their assistance throughout the research.

I appreciate the support of Mr. Gan Zi Li, Mr. Wilson Lim, Mr. Patrick Lai, and all the technicians in the MSE labs, whose help with facility training was indispensable.

I am fortunate to have had the support of my group members in Professor Chen's lab, particularly Mr. Chen Lixun and Ms. Wong Yi Jing.

Lastly, I am deeply grateful to my family and friends, especially my parents and Dr. Lao Jiazheng, for their encouragement and companionship throughout my PhD journey.

Table of Contents

Table Captions

Figure Captions

based robotic hands. Reproduced with permission from ref.[18]. Copyright 2024 American Chemical Society. (d) Bimodal sensing array for robust object recognition. Reproduced with permission from ref.[19]. Copyright 2022 Springer Nature. (e)Piezoelectric skin tele-tactile system for texture classification. Reproduced with permission from ref.[20]. Copyright 2022 Springer Nature. (f) Ionic skin for fingertip-like tactile sensation. Reproduced with permission from ref.[21]. Copyright 2011 Wiley. (g) Bimodal-sensitive tactile systems. Reproduced with permission from ref.[22]. Copyright 2023 American Chemical Society. (h) CNN-based tactile sensor system for roughness recognition. Reproduced with permission from ref.[23]. Copyright 2019 Elsevier.

Figure 2.5 Venn diagram of machine learning algorithms learning concepts and classes.

Figure 2.6 AI for artificial tactile sensing systems. (a) CNN + Sparse NN for gesture recognition. Reproduced with permission from ref.[24]. Copyright 2020 Springer Nature. (b) kNN for expression recognition. Reproduced with permission from ref.[25]. Copyright 2020 Springer Nature. (c) SVM for sign language recognition. Reproduced with permission from ref.[26]. Copyright 2020 Springer Nature. (d) Decision trees for texture recognition. Reproduced with permission from ref.[27]. Copyright 2023 Wiley. (e) Adaboost for blood pressure monitoring. Reproduced with permission from ref.[28]. Copyright 2022 Springer Nature. (f) Multilayer perception for object detection. Reproduced with permission from ref.[29]. Copyright 2020 American Association for the Advancement of Science

Figure 2.7 (a) Schematic diagrams of the ductal anatomy of the breast. Structure of human breasts[30]. 1. Chest wall. 2. Pectoral muscles. 3. Lobules. 4. Nipple surface. 5. Areola. 6. Lactiferous duct. 7. Fatty tissue. 8. Skin. (b) Schematic diagrams of breast nodules, including cyst, fibroadenoma, and tumor. (c) Schematic figures for palpation on human breast.

Figure 2.8 Tactile sensing gloves. (a) A scalable tactile glove human grasp classification. Reproduced with permission from ref. [31]. Copyright 2019 Springer Nature. (b) Bimodal sensing data for tactile body-feature identification. Reproduced with

permission from ref. [32]. Copyright 2022 Wiley. (c) Tactile glove enabling dynamic object classification. Reproduced with permission from ref. [33]. Copyright 2024 American Association for the Advancement of Science (d) Tactile gloves for Health and Tactile Touch Monitoring. Reproduced with permission from ref.[34]. Copyright 2017 Wiley. (e) Smart textile gloves for object interaction. Reproduced with permission from ref.[35]. Copyright 2024 Springer Nature. (f) Stretchable sensor arrays on hands for sign-to-speech. Reproduced with permission from ref.[26]. Copyright 2020 Springer Nature. (g) A portable rehabilitation gloves. Reproduced with permission from ref.[36]. Copyright 2023 Springer Nature. (h) Smart gloves both sensing and feedback for VR/AR. Reproduced with permission from ref.[37]. Copyright 2020 American Association for the Advancement of Science.

Figure 3.1 Common construction of tactile sensors. Substates. (a) Ultra-slim glass substrates. Reproduced with permission from ref.[38]. Copyright 2012 John Wiley and Sons. (b) PET/PI substrates. Reproduced with permission from ref.[39]. Copyright 2020 Elsevier. (c) PDMS substrates. Electrodes. Reproduced with permission from ref.[40]. Copyright 2021 American Association for the Advancement of Science (d)Ag nanowires. Reproduced with permission from ref.[41]. Copyright 2020 American Association for the Advancement of Science (e) MWCNTs. Reproduced with permission from ref.[42]. Copyright 2018 Wiley. (f) Hydrogel. Functional materials. Reproduced with permission from ref.[43]. Copyright 2022 Elsevier. (g) Piezoresistive layer. Reproduced with permission from ref.[6]. Copyright 2020 Springer Nature. (h) capacitive layer. Reproduced with permission from ref.[44]. Copyright 2019 Springer Nature. (i) Piezoelectric/triboelectric layer. Reproduced with permission from ref.[45]. Copyright 2022 Springer Nature.

Figure 3.2 Simulation results of cantilever beam using COMSOL Multiphysics simulation. (a) Finite element model of piezoelectric cantilever beam. Reproduced with permission from ref.[46]. Copyright 2024 Elsevier. (b) The eigenfrequency of the 1st, 2nd, and 3rd-order resonance mode with COMSOL Multiphysics simulation. Reproduced with permission from ref.[47]. Copyright 2021 Wiley.

Figure 3.3 Schematic diagrams of matrix with parasitic path. (a) Crossover circuits, and (b) equivalent circuits. The blue path is the intended path, and the orange path is the parasitic path.

Figure 3.4 Schematic diagrams of reading circuit designs for countering parasitic resistance. (a) Circuit A with feedback design. Buffers and a switch are used to apply the output voltage to the rows and columns, respectively, to counteract crosstalk and the effects of row-row and column-column couplings (Rrr and Rcc). (b) Circuit B with feedback design. Each row is powered by a constant voltage source through independent buffers. (c) Circuit C with grounding design. This circuit is similar to Circuit A, but it counteracts crosstalk by inserting buffers on both the rows and columns. Reproduced with permission from ref.[48]. Copyright 1999 Elsevier.

Figure 3.5 A schematic diagram of 2D classification by SVM. Finding a line can completely separate all input points.

Figure 4.1 Fabrication processes of a single piezoelectric vibration sensor.

Figure 4.2 Principal support for vibration-induced quantitative texture sensing. (a) a schematic cantilever beams for force sensing. (b) Simulation results of vibration and generated voltage results.

Figure 4.3 Configuration of the piezoelectric tactile sensor. (a) A schematic structure of piezoelectric tactile sensor. (b) Picture of top view of a single piezoelectric vibration sensor. The scale bar is 4 mm (c) Picture of side view of the piezoelectric tactile sensor. The scale bar is 4 mm (d) The second schematic structure of piezoelectric tactile sensor showing the parallel distribution of vibration sensors. (e) Picture of side of a 3D printed structural materials integrated with vibration sensors.

Figure 4.4 Grating textures based on photolithography. (a) Schematic side view image

of grating-textures. t is thickness of the textures. d_1 is the width of the textures. d_2 is the distance of the textures. (b) Picture of side view of grating-textures on a silicon wafer. Optical images of different grating textures with different width and distance. (c) d_1 = 50 μm. d_2 = 400 μm. (d) d_1 = 100 μm. d_2 = 400 μm. (e) d_1 = 200 μm. d_2 = 400 μm. (f) d_1 = 600 μm. d_2 = 400 μm. The scale bar is 200 μm.

Figure 4.5 Response of the piezoelectric vibration sensor on piezoelectric tactile sensor. (a) Mechanism of dynamic force sensing. (b) Piezoelectric voltage signals while gliding over a grating-texture (d_1 = 600 μm. d_2 = 400 μm) under speed of 25 mm/s. (c) Zoom-in figure of voltage signals. (d) Picture of a 3-axis moving platform.

Figure 4.6 Thickness and 2D scanning of surface profiler (Alpha-Step D600). The 2D information of grating-structures on silicon wafers (d_1 = 200 μm. d_2 = 400 μm) under speed of 0.2 mm/s.

Figure 4.7 Mechanism of quantitative texture sensing on the dimension of width and distance. The inserted optical image shows the parameters of the tested grating-textures (d1 = 200 μm and d2 = 400 μm). The scale bar is 200 μm.

Figure 4.8 Quantitative texture sensing test on unknown grating parameters. (a) Piezoelectric voltage signals while gliding over an unknown grating-texture. (b) Optical image of the unknown grating-texture showing the actual width and distance.

Figure 4.9 Piezoelectric voltage signals while gliding over a grating-texture (d_1 = 100 μm. d_2 = 300 μm) under different speed: (a) 5 mm/s. (b) 20 mm/s. (c) 30 mm/s.

Figure 4.10 Cyclic scanning test of our device on a micro-step showed good durability.

Figure 4.11 Mechanism explanation of the time-independent peak F. (a) Equivalent circuit of a single piezoelectric vibration sensor. (b) Schematic change of slow deformation which generate the peak C. (c) Schematic change of transient deformation which generate

the peak F.

Figure 4.12 Simulation results of piezoelectric vibration sensor. (a) Configuration of grating-texture testing using MATLAB (b) piezoelectric voltage generated by a single piezoelectric vibration sensor.

Figure 4.13 Linear relationship between the amplitude of peak F and thickness of gratings. (a) The testing results of peak F changes with thickness of grating. (b) The simulation results of peak F changes with thickness of grating.

Figure 4.14 Theoretical analysis of the piezoelectric tactile sensor for quantifying height, width of surface features. Height measurement and feature analysis in piezoelectric signal when the first sensing tip (blue) scans across a step-like microstructure. Insets illustrate different states during measurement: state i, the tip fully positioned on the step surface; state ii: the tip is at the point of departing from the step edge; state iii, the tip just returns to the base level. b) Width measurement methodology based on three critical parameters: the spacing between two tips (Δd), time delay in the twin signals (Δt_1), and time interval between two states (Δt_2; states iv and v in (a)). Insets illustrate the states of the second sensing tip (red): it fully positioned on the step surface (state iv), and it is departing from the step edge (v).

Figure 4.15 Portable piezoelectric tactile sensor and its piezoelectric voltages when operating. (a) Schematic picture of side view of the tested grating structures. (b) Picture of operation of portable piezoelectric tactile sensor. (c) Piezoelectric voltages of portable piezoelectric tactile sensor with two vibration sensors.

Figure 4.16 The influence of film spacing (Δd) on device performance: a) 0.88 mm, b) 1.94 mm, and c) 2.66 mm. Where Δt is the time delay between two signals.

Figure 4.17 Piezoelectric tactile sensor for micro-scale patterns imaging. (a) Schematic picture of a Chinese knot patterns. Three different gliding direction are shown. (b) Optical

image of the Chinese know pattern. The scale bar is 500 μm. (c) Piezoelectric voltage of the piezoelectric tactile sensor gliding test with direction A, B, and C. The calculated thickness changes with time.

Figure 4.18 Micro-scale pattern 3D-reconstruction using piezoelectric tactile sensor. (a) 3D heatmap of 3D-reconstruction results. (b) 2D heatmap of 3D-reconstuction results.

Figure 4.19 Frequency-domain signals of surface scans for six 3D-printed workpieces, obtained via Fourier transform of time-domain voltage signals, each figure containing 80 signals.

Figure 4.20 Machine learning-based roughness classification training: a) Time-domain piezoelectric signals for different textures. b) Frequency-domain signals obtained through Fourier transform, revealing distinct differences in the number of peaks, peak coordinates, and peak amplitudes. c) Feature extraction where the number of peaks, peak coordinates, and peak amplitudes are used as features for LDA analysis of texture signals, showing excellent peak classification with well-separated points. d) Classification using SVM with the extracted features, achieving 100% classification accuracy. The test set consists of 40 samples, and the training set consists of 480 samples.

Figure 4.21 Theoretical analysis and modeling of piezoelectric vibration sensor for quantifying height, width, and edge profiles of surface features. a) Schematic showing the piezoelectric twin-film architecture (two tips) with interlayer distance (Δd) as it scans a surface microstructure. b) Schematic showing piezoelectric twin signals with a time delay (Δt_1), generated by the operation in (d) (top). Key features in the twin signals—such as peaks, valleys and time delay (Δt_1)—are systematically analyzed to extract microstructural characteristics including height (h), width (w) and edge profile. The surface profile is subsequently reconstructed (bottom). c) Schematic representation of the edge profile reconstruction. The slope angle β at each point of the edge profile can be calculated based on the piezoelectric signal $V(t)$. The x-coordinate (w) can be calculated

from the *t*, and the y-coordinate (*h*) can be calculated by: $w \cdot \tan\beta$. d) The relationship between simulated slope β and calculated β showing a mean average percentage error of only 0.61%.

Figure 4.22 Three-dimensional rational function fitting illustrating the relationship between microstructure angle cotβ, maximum voltage derivative, and initial voltage V(0) through comprehensive parametric mathematical modeling, establishing a predictive framework for microstructure geometry characterization.

Figure 4.23 Parametric mathematical modeling for trapezoidal edge angle prediction. (a) Correlation between actual and predicted $cot\beta$ values, showing strong linear relationship with $R^2 > 0.99$ across the full range of tested angles. (b) Distribution of $cot\beta$ prediction errors, demonstrating a narrow Gaussian distribution centered near zero with standard deviation < 0.02. (c) Direct comparison between actual and predicted angle β values in degrees, illustrating excellent agreement between measured geometric parameters and model predictions. (d) Histogram of angle β prediction errors showing consistent accuracy below 1% error threshold, with most predictions falling within ±0.5%, validating the reliability of our parametric mathematical model for non-invasive microstructure characterization in flexible electronic systems.

Figure 4.24 Edge profile reconstruction in three distinctive edge configurations (convex, linear, and concave edges) exhibited minimal measurement errors, with MAPE values being 2.14%, 2.50% and 1.92%, respectively. Dashed red curves: reconstructed profiles; dark line: actual edge profiles.

Figure 5.1 Preparation steps of pressure sensors

Figure 5.2 Preparation steps of tactile sensing array.

Figure 5.3 Images of single electrodes and electrodes array. (a) Optical microscope image of a single interdigital circle-like electrodes. Scale bar is referred to 200μm. (b)

Figure 5.11 Mechanical testing of adhesion performance. (a) Stretching force changes with the displacement of three samples, including 1. PU + PI + WPU adhered under 120°C using hot-press (0.1 MPa). 2. PU + PU + WPU adhered under 80°C. 4. PU + PU adhered under 80°C. (b) Sheer strength comparison of the samples.

Figure 5.12 Cyclic mechanical test of the stability-enhanced pressure sensor. (a) Picture of a laboratory-made pressure testing platform. (b) Four cycles of pressure testing. All cycles are processed under moving speed of 35 μm/s, (c) Resistance change with pressure. (d) 100 cycles of contrast pressure sensors without surface modification. (e) 300 cycles of contrast pressure sensors with surface modification. (f) The response times of stability-enhanced pressure sensor.

Figure 5.13 Data acquisition designs of hand-like tactile gloves. (a) The schematic crosstalk effect in traditional arrays of piezoresistive sensors. (b) Circuit based on grounding design for sensor arrays data acquisition against crosstalk. (c) The Bluetooth data acquisition circuit design of hand-like tactile gloves contains time-division multiplexers with 10 Hz data reading rate for 142 channels.

Figure 5.14 PCB & Flexible PCB for data acquisition systems. (a) Hardboard PCB with Bluetooth transmission USB interface. (b) Flexible PCB connected with 3000 mA·h Lithium battery.

Figure 5.15 The stability-enhanced tactile gloves and the array signals User-Interface (UI). (a) Picture of the tactile glove. (b) The distribution of sensors on the palm and the corresponding serial port channel numbers. (c) Data-visualized UI of the tactile glove.

Figure 5.16 Force distribution analysis of tactile gloves. (a) Initial state of force detection UI. (b) New state when ‘N’ word-shape acrylic sheet placing on tactile glove. (c) New state when ‘T’ word-shape acrylic sheet placing on tactile glove. (d) New state when ‘U’ word-shape acrylic sheet placing on tactile glove

Abbreviations

2D	Two-dimensional
3D	Three-dimensional
ATR	Attenuated Total Reflectance
AI	Artificial Intelligence
Au	Gold
ANN	Artificial Neural Networks
CNT	Carbon Nanotubes
CNN	Convolutional Neural Networks
FTIR	Fourier Transform Infrared Spectroscopy
ML	Machine Learning
PET	Polyethylene terephthalate
PI	Polyimide
PU	Polyurethane
RNN	Recurrent Neural Networks
SVM	Support Vector Machine
XPS	X-ray Photoelectron Spectroscopy

Chapter 1

Introduction

This thesis investigates advanced tactile sensing systems for object recognition and texture characterization. It tests two hypotheses: the use of piezoelectric vibration sensors for quantitative texture analysis under variable conditions, and tactile sensing gloves for quantitative object sensing and medical diagnostics. The research includes the development of piezoelectric sensors, integration of a 142-channel pressure sensing array into tactile gloves, and the creation of a piezoelectric tactile sensor for detailed texture analysis. Findings demonstrate the effectiveness of these technologies in providing accurate, real-time data for both object recognition and medical applications, offering new insights and advancements in tactile sensing.

1.1 Hypothesis/Problem Statement

Tactile sensing systems play a critical role in object recognition and texture sensing by providing information that can be analyzed to understand surface properties and object characteristics[1]. Traditional methods for texture and object sensing often rely on visual or manual inspection, which may lack precision or be limited by environmental conditions. Tactile sensing systems, however, offer a more detailed and accurate means of assessing textures and objects by capturing tactile interactions[2-4]. In particular, in-situ object recognition is increasingly important for applications requiring real-time feedback, such as robotic manipulation and medical diagnostics. This need for immediate and precise data drives the development of advanced tactile sensing technologies that can function effectively in dynamic and variable environments.

The hypothesis in this thesis is to realize in-situ object recognition with softness, size and texture. The first hypothesis is that piezoelectric tactile sensors can accurately quantify textures by sensing dynamic forces. By employing two calibrated sensors, the system aims to provide precise texture analysis without needing machine-controlled speeds. The sensors' ability to detect variations in vibration frequency and amplitude is expected to deliver detailed surface information, making the system adaptable to variable speed conditions. The second hypothesis is tactile system with a pressure sensing array enabling quantitative object sensing. It is hypothesized that the number of activated sensors correlates with the object's size, and greater sensor density improves accuracy. This approach could enhance the measurement of object characteristics and advance medical diagnostics by providing precise, non-invasive tissue assessments.

1.2 Objectives and Scope

Based on the above hypotheses, the following objectives are to be accomplished by the end of the study:

1. To develop piezoelectric sensors and texture sensing systems for quantitative texture sensing

2. To realize micro-scale patterns reconstruction with the texture sensing systems.

3. To enhance the stability of pressure sensors for accurate medical diagnostic tasks.

4. To integrate the developed materials for on skin conformal electrodes, and further integrate with wearable and wireless electronics to realize conformal on-skin biopotential measurement.

This research encompasses the design, development, and validation of tactile sensing systems focused on object recognition and texture sensing. The scope includes:

1. Fabrication of piezoelectric tactile Sensors: Development of piezoelectric vibration sensors and a texture sensing system to achieve detailed and accurate texture characterization.

2. Characterization of piezoelectric tactile sensors' response: Comprehensive analysis of the piezoelectric tactile sensor to ensure its speed-independent property, verifying that texture characterization remains accurate regardless of scanning speed.

3. Simulation for response of piezoelectric tactile sensor: Conducting simulations of the piezoelectric tactile sensor to support and explain its operational mechanisms, providing insights into how it achieves precise texture characterization.

4. Integration of intelligent tactile system: Creation of tactile gloves featuring a 142-channel pressure sensing array, evaluating their performance in object sensing and medical diagnostics.

5. Machine Learning-based medical classification tasks: Implementation of machine

learning algorithms for object classification tasks, demonstrating the potential for advanced object recognition and analysis.

1.3 Dissertation Overview

The thesis consists of the following 6 chapters:

Chapter 1: Introduction
This chapter introduces the research, providing a rationale and outlining the goals. It focuses on the design and validation of tactile sensing systems for object recognition, including texture sensing and medical palpation.

Chapter 2: Literature Review
This chapter reviews current tactile sensing technologies and their applications. It covers human tactile perception, various tactile force sensors, machine learning algorithms in tactile systems, and advances in tactile gloves for robotics and healthcare.

Chapter 3: Experimental Methodology
The methodology chapter details the selection and use of piezoelectric and pressure sensing technologies. It describes the construction of tactile sensors, mechanical simulations, data acquisition methods, and the use of SVMs for classifying tactile stimuli.

Chapter 4: A piezoelectric tactile sensor for in-situ measurement of micro-scale surface profile
This chapter introduces a piezoelectric tactile sensor, which uses piezoelectric sensors for quantitative texture analysis. Unlike traditional systems, the sensor provides detailed micro-scale morphology characterization and can be integrated into robotic systems for real-time texture reconstruction.

Chapter 5: An intelligent piezoresistive tactile system for in-situ quantifying object features

This chapter describes the design and fabrication of stability-enhanced tactile gloves. It details the integration of pressure sensing arrays, stability reinforcement methods, and the application of the gloves in healthcare classification tasks, showing their potential for diagnostic use.

Chapter 6: Conclusions and Recommendations
The conclusion summarizes the findings on tactile sensing technologies. It validates the use of piezoelectric sensors for in-situ quantification of micro-scale object texture and a intelligent tactile systems for quantitative clinic classification. The chapter proposes future work integrating these technologies with robotics and AI for enhanced diagnostics.

1.4 Findings and Outcomes/Originality

This research led to several novel outcomes by:

1. Developing a piezoelectric tactile sensor and designing a texture sensing system.

2. Utilizing microscale Chinese knot patterns, fabricated via photolithography, for 3D structure reconstruction.

3. Creating tactile sensing systems by integrating a 142-channel pressure sensing array with fabric gloves.

4. Enhancing sensor stability through both surface modification and encapsulation techniques.

5. Conducting object classification tasks using machine learning methods.

References

[1] Li N, Yin Z, Zhang W, Xing C, Peng T, Meng B, Yang J and Peng Z. *Nano Energy*. **2022**, 96, 107063.

[2] Huang S, Liu Y, Zhao Y, Ren Z and Guo CF. *Advanced Functional Materials.* **2019**, 29, 1805924.

[3] Heng W, Solomon S, Gao W. *Advanced Materials.* **2022**, 34, 2107902.

[4] Li G, Liu S, Wang L and Zhu R. *Science Robotics.* **2020**, 5, eabc8134.

Chapter 2

Literature Review

This chapter reviews the current state of tactile sensing technologies and their applications. It explores human touch sensing, including biological mechanisms of tactile perception. The chapter examines various tactile force sensors, focusing on their sensing mechanisms and uses in object and texture detection. It also discusses machine learning algorithms employed in tactile systems, their categories, and applications. Further, it covers the role of tactile sensors in medical palpation and highlights advancements in tactile sensing gloves for rehabilitation and virtual reality. This overview provides a snapshot of the progress and trends in the field of tactile sensing.

2.1 The sense of human touch

Skin, the human body's largest organ, plays a crucial role in providing a gateway to vital biological signals originating from internal organs, blood vessels, muscles, and the various layers of the skin itself[1, 2]. This unique characteristic makes skin an invaluable source of information, as it can both generate and transmit biological signals that reveal important health metrics. The intricate construction of the skin can be broken down into several key layers, each with distinct functions and characteristics.

The structure of human skins is demonstrated in the Figure 2.1. The outermost layer of the skin, known as the epidermis, acts as a protective barrier against environmental hazards[3]. The epidermis is composed of multiple sub-layers, including the stratum corneum, which consists of dead, flattened cells known as corneocytes. These cells are stacked in layers and play a vital role in water retention, which is crucial for maintaining hydration. Beneath the stratum corneum are living basal cells that continuously reproduce, ensuring the regeneration of the skin. The epidermis also serves as a route for the excretion of sweat, which contains various biomarkers such as pH, mineral ions, glucose, water, lactic acid, and urea. These components can provide valuable insights into a person’s health status. Beneath the epidermis lies the dermis, a thicker layer that contains a network of blood vessels, nerves, and connective tissues. This layer is critical for regulating body temperature and supplying the skin with nutrients. Major arteries within the dermis carry cardiovascular information that can be detected at the skin's surface, including metrics like heart rate, blood pressure, oxygen levels, and pulse wave velocity. The dermis also houses nerve endings that respond to stimuli, providing the sensation of touch and pain. These nerves include major ones like the median nerve from the brachial plexus, which innervates muscle fibers to stimulate physical contraction. This activity produces a summation of action potentials, which can be recorded by electrodes placed near the targeted muscle group, revealing crucial biopotential signals.

The innermost layer of the skin is the hypodermis, also known as the subcutaneous layer. This layer primarily consists of fat and connective tissues that provide cushioning and insulation for the body. The hypodermis also plays a role in storing energy and serves as a conduit for larger blood vessels and nerves that extend into the dermis and epidermis. Additionally, this layer helps anchor the skin to the underlying structures, allowing for flexibility and mobility.

The construction of the skin and its rich array of bio-signals make it an ideal platform for developing application-specific electronic sensing devices. These devices often utilize polymer-based skin-mounted substrates, which can adhere to the skin surface and accurately detect and monitor various physiological parameters. By leveraging the skin's natural properties and the advanced capabilities of modern sensors, these technologies have the potential to revolutionize the way we monitor and understand human health.

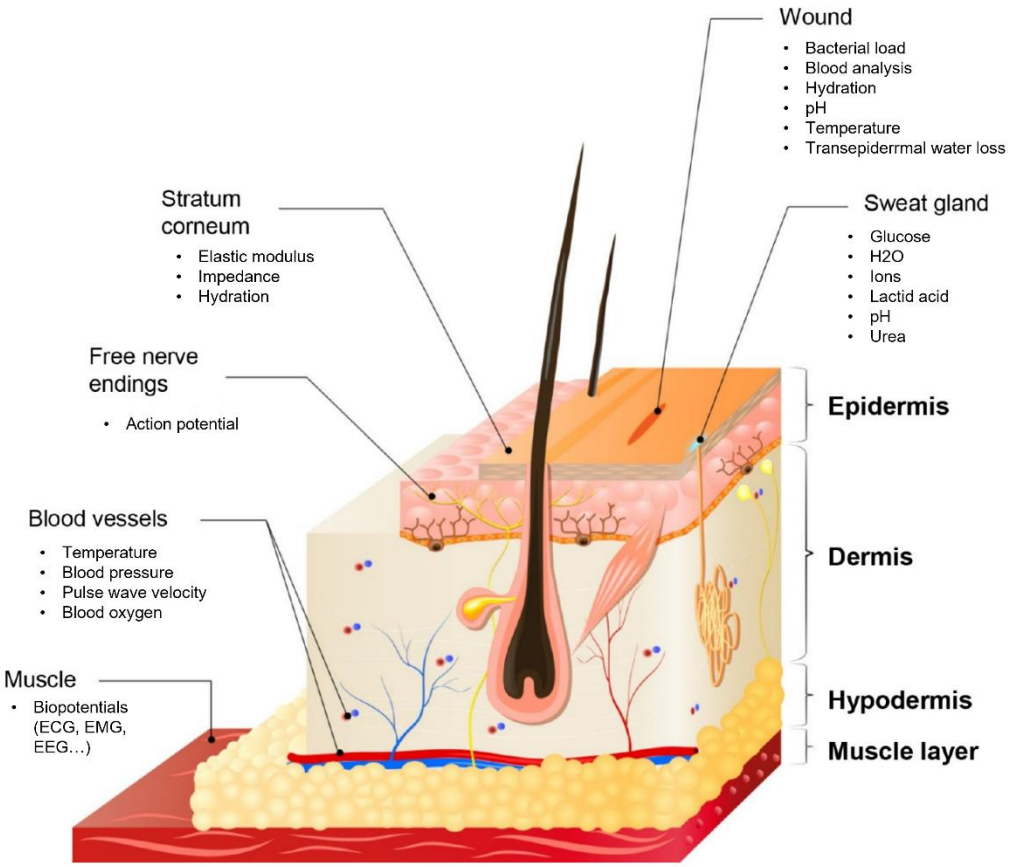

Figure 2.1 Structure of human skins. Reproduced with permission from ref.[3].

Restoring a natural sense of touch involves replicating the sensory properties of biological skin, which requires a deep understanding of the key factors that influence these properties. Human skin contains a variety of sensory receptors. Other than pain receptors, cold receptors, warm receptors, four types of mechanoreceptors that detect non-painful mechanical stimuli are of great importance to understand the sense of interactive touch[4, 5]. These receptors encode sensory information through action potentials, where the timing between voltage spikes conveys different types of sensory data.

Among the mechanoreceptors, there are four distinct types, each specialized to respond to different mechanical stimuli with varying temporal and spatial sensitivities. These mechanoreceptors include Slow Adapting type I (SA-I), Slow Adapting type II (SA-II), Fast Adapting type I (FA-I), and Fast Adapting type II (FA-II) receptors. They are distinguished by their response to the frequency of stimuli, as well as the size of their receptive fields—the area of skin that triggers a response[5-7]. Here is the location and response characteristics of the four mechanoreceptors:

SA-I receptors are located near the surface of the skin, particularly in high-density areas like the fingertips. They are highly sensitive to skin indentations, providing detailed information about static pressure[8]. These receptors produce a sustained signal in response to a constant stimulus, which is why they are termed ‘slow adapting’. This continuous signal allows for the perception of steady pressure and fine details, making them crucial for tasks that require high-resolution force discrimination, such as identifying object shapes and textures.

In addition to SA-I receptors, SA-II receptors are situated deeper within the skin and are primarily responsible for detecting skin stretch, which is essential for proprioception—the sense of the relative position of body parts. Similar to SA-I receptors, SA-II receptors also produce sustained signals but are specifically sensitive to lateral skin deformation[9]. This

sensitivity makes them key for detecting changes in body posture and for maintaining balance and coordination.

FA-I receptors are located in the upper layers of the skin and are involved in detecting low-frequency (5–50 Hz) vibrations. They are particularly important for sensing changes in object position and detecting textures during manipulation. These receptors respond rapidly to dynamic forces and vibrations, producing transient signals in response to changes in stimuli. This quick adaptation allows them to detect fine textures and provide feedback necessary for adjusting grip force during tasks like holding and manipulating objects.

FA-II receptors are found deeper in the skin and are specialized in detecting high-frequency vibrations, up to 400 Hz. They cover larger areas of the skin compared to FA-I receptors. FA-II receptors are crucial for detecting fine textures and the onset of slip between the skin and an object[10]. They respond quickly to high-frequency stimuli, providing the brain with detailed information about the surface qualities of objects and the dynamics of interactions, such as slipping.

The sensory signals generated by these mechanoreceptors are transmitted through nerve fibers, each of which carries information from multiple receptors. The brain interprets the combined input from these receptors to form a complex picture of the body's position and the properties of objects being touched, such as size, shape, texture, and hardness. The time delay for these signals to travel from the skin to the brain is typically in the range of several tens of milliseconds, allowing for rapid and accurate sensory perception. Understanding and mimicking the function of these receptors is crucial in the development of artificial skin technologies and prosthetics that aim to restore a natural sense of touch[11].

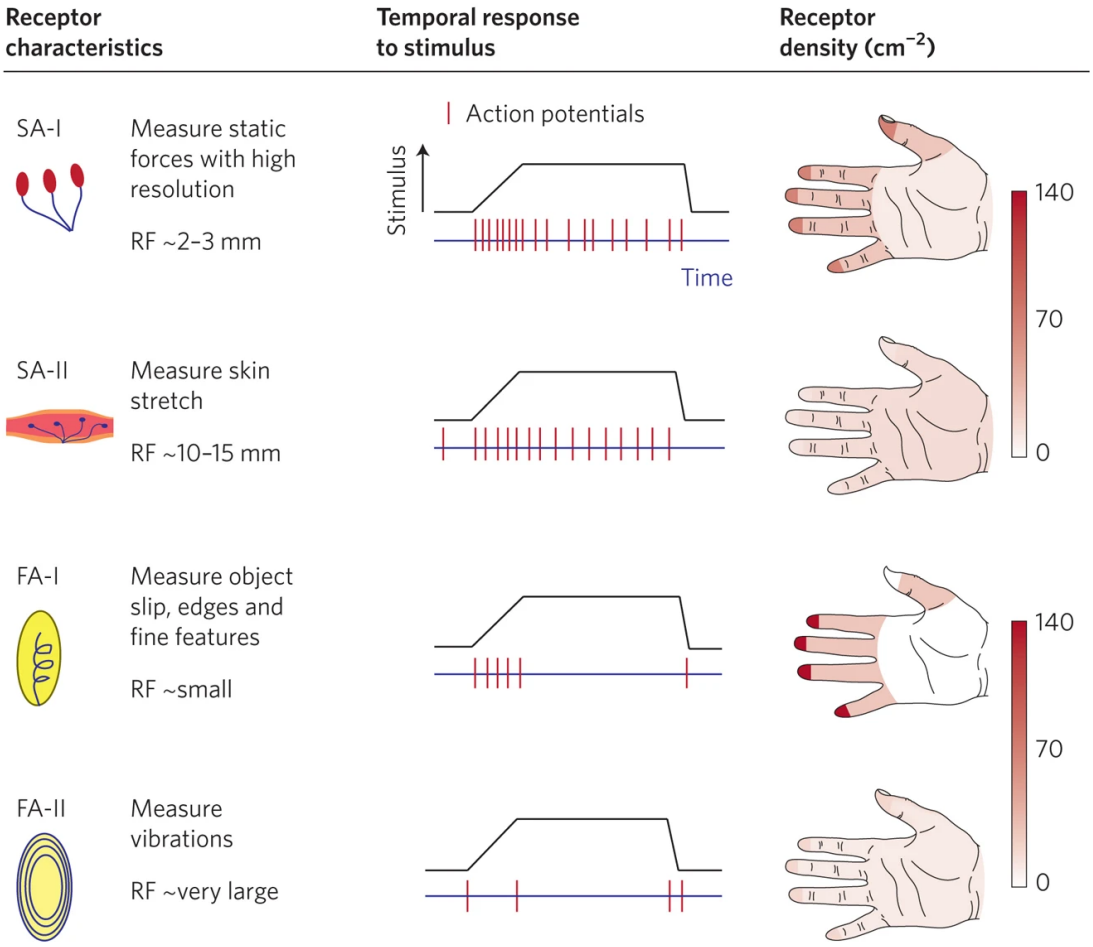

Figure 2.2 Four types of mechanoreceptors, including SA-I and SA-II, slow adapting receptors; FA-II and FA-II, fast adapting receptors. Reproduced with permission from ref.[6]. Copyright 2016 Springer Nature.

2.2 Artificial tactile sensing

Artificial sensing devices, known as tactile or tactile sensors, are designed based on the sensory capabilities of human skin. These tactile sensors, commonly referred to as strain and pressure sensors, are capable of gathering data on the mechanical properties of the human body and its surrounding environment, providing valuable insights into human health, human-machine interfaces (HMIs) and supporting artificial intelligence systems. By incorporating high levels of wearability, including bendability and stretchability, tactile sensors can significantly improve their interaction with contact surfaces, ensuring reliable

long-term performance[12-14]. This flexibility allows wearable tactile sensors to conform to various curved surfaces without damage, positioning them as a promising technology for Internet of Things (IoT) applications[15].

The fundamental parameters of wearable tactile sensors, such as sensitivity and stretchability, have seen remarkable advancements thanks to progress in device fabrication techniques and material structural engineering. The development of new smart materials and robust sensor designs has enabled these sensors to integrate multiple functionalities, such as simultaneous detection of force, temperature, and humidity, as well as discrimination between pressure and strain. These sensors also possess exciting properties like biocompatibility, biodegradability, self-healing, self-powering, and visualization, expanding their potential applications. Furthermore, the compatibility of tactile sensors with printing processes heralds a new era of wearable technology, offering the possibility of large-area and high-throughput production. Beyond sensor development, the integration of other system components, such as data storage, signal conversion, power supply, wireless communication, and feedback actuators, into a comprehensive wearable platform has become a major area of research in recent years.

In this part, it aims to summarize the current advancements in wearable tactile sensors, covering sensing mechanisms, static force sensing, dynamic force sensing.

2.2.1 Mechanisms, materials, and sensors

Five types of sensing mechanisms commonly used in tactile sensors, each leveraging different physical principles to detect and measure various stimuli. These mechanisms are piezoresistive, capacitive, piezoelectric, optical, and magnetic. Here's a summary of each mechanism (shown in Figure 2.3):

1. Piezoresistive Mechanism: The piezoresistive mechanism relies on changes in electrical resistance due to mechanical deformation of a material. The deformation can be caused by various factors such as geometrical effects, crack propagation,

disconnection mechanisms, and tunneling effects. As the material is deformed, the electrical resistance changes, allowing the sensor to detect and measure the magnitude of the applied force or pressure. There are mainly fours kinds of mechanisms that contributes to piezoresistive change: 1. Geometrical effect: The change in resistance is due to the stretching or compressing of the material, which alters the length and cross-sectional area of the conductive paths. 2. Crack propagation: Cracks in the material can change the conduction pathways, thereby affecting the resistance. 3. Disconnection mechanism: When parts of the conductive material disconnect due to deformation, it causes a significant change in resistance. 4. Tunneling effect: At the nanoscale, quantum tunneling can occur between conductive particles in a dielectric matrix, and this effect is sensitive to changes in distance between particles due to mechanical strain. Systems based on the piezoresistive mechanism are typically easy to fabricate, feature simple readout circuits, and are well suited for large-scale array integration. Although they are often challenged by consistency issues, their relatively low cost has made them widely adopted in artificial tactile systems.

2. Capacitive Mechanism: The capacitive mechanism is based on changes in capacitance due to the deformation of the sensor. This can be influenced by changes in the distance between conductive plates, the dielectric constant of the material between the plates, or the relative area of the overlapping conductive surfaces. There are three mechanisms: 1. Distance change. The capacitance changes as the distance between two conductive plates changes. 2. Dielectric constant change. Variations in the dielectric material's properties, often due to pressure or other environmental factors, alter the capacitance. 3. Relative area change. The effective overlapping area of the conductive plates changes due to mechanical deformation, affecting the capacitance. Systems based on the capacitive mechanism generally offer high sensitivity; however, in large-area arrays they are prone to crosstalk and environmental noise (e.g., humidity and temperature), leading to limited signal stability.

3. Piezoelectric/triboelectric mechanism: These mechanisms involve materials that generate an electric charge in response to mechanical stress. This property is inherent

in certain materials, such as quartz and some ceramics, which generate a voltage when subjected to mechanical deformation. These mechanisms can be further classified into four types, including vertical contact mode, single electrode mode, sliding mode, and freestanding mode. Piezoelectric and triboelectric effect are widely used for detecting vibrations, pressure, and other mechanical changes by converting these physical changes into electrical signals. Systems based on piezoelectric or triboelectric mechanisms exhibit very fast response speeds, making them highly suitable for high-frequency applications. Nevertheless, due to the transient nature of their signals, they are not well suited for measuring static mechanical loads.

4. Optical Mechanism: Optical mechanisms utilize light-based technologies to detect changes in light strength in optical fibers or optical light pathway. Optical Detection: The mechanism can involve LEDs and photodiodes where mechanical movements alter the path or properties of light, such as through reflection, refraction, or occlusion, which can be detected and measured. Systems based on the optical mechanism achieve excellent stability and fast response due to light-based detection, but their structural complexity hinders dense array integration.

5. Magnetic Mechanism: Magnetic mechanisms detect changes in magnetic fields or properties due to mechanical interactions. Magnetic This involves sensors that detect variations in magnetic fields, which can occur due to the movement or deformation of magnetic materials or components. These changes can be translated into electrical signals for further processing. Systems based on the magnetic mechanism also provide high stability and rapid response; however, they are susceptible to interference from external magnetic fields and, similarly, face challenges of system complexity that limit scalability for high-density integration.

Each of these mechanisms offers unique advantages and can be selected based on the specific requirements of the application, such as sensitivity, range, response time, and environmental conditions.

The choice of piezoresistive and piezoelectric mechanisms is primarily based on their complementary application needs. Piezoelectric sensors can respond rapidly and sensitively to dynamic loads and vibration signals, making them suitable for high-frequency and high-speed surface microstructure scanning. In contrast, piezoresistive sensors perform stably in static pressure and strain detection, while offering simple circuit readout and scalability for large-area array integration. The combination of the two enables simultaneous acquisition of both dynamic and static information, thereby achieving comprehensive tactile perception. Capacitive mechanisms, despite their high sensitivity, are prone to crosstalk and environmental noise in large-scale arrays, leading to insufficient signal stability. Triboelectric-based systems are generally more complex in design compared with piezoelectric systems. In our work, by leveraging the mechanical characteristics of the cantilever beam, the piezoelectric effect provides a direct and efficient means of capturing high-frequency dynamic mechanical signals and reconstructing the surface microstructure of the target.

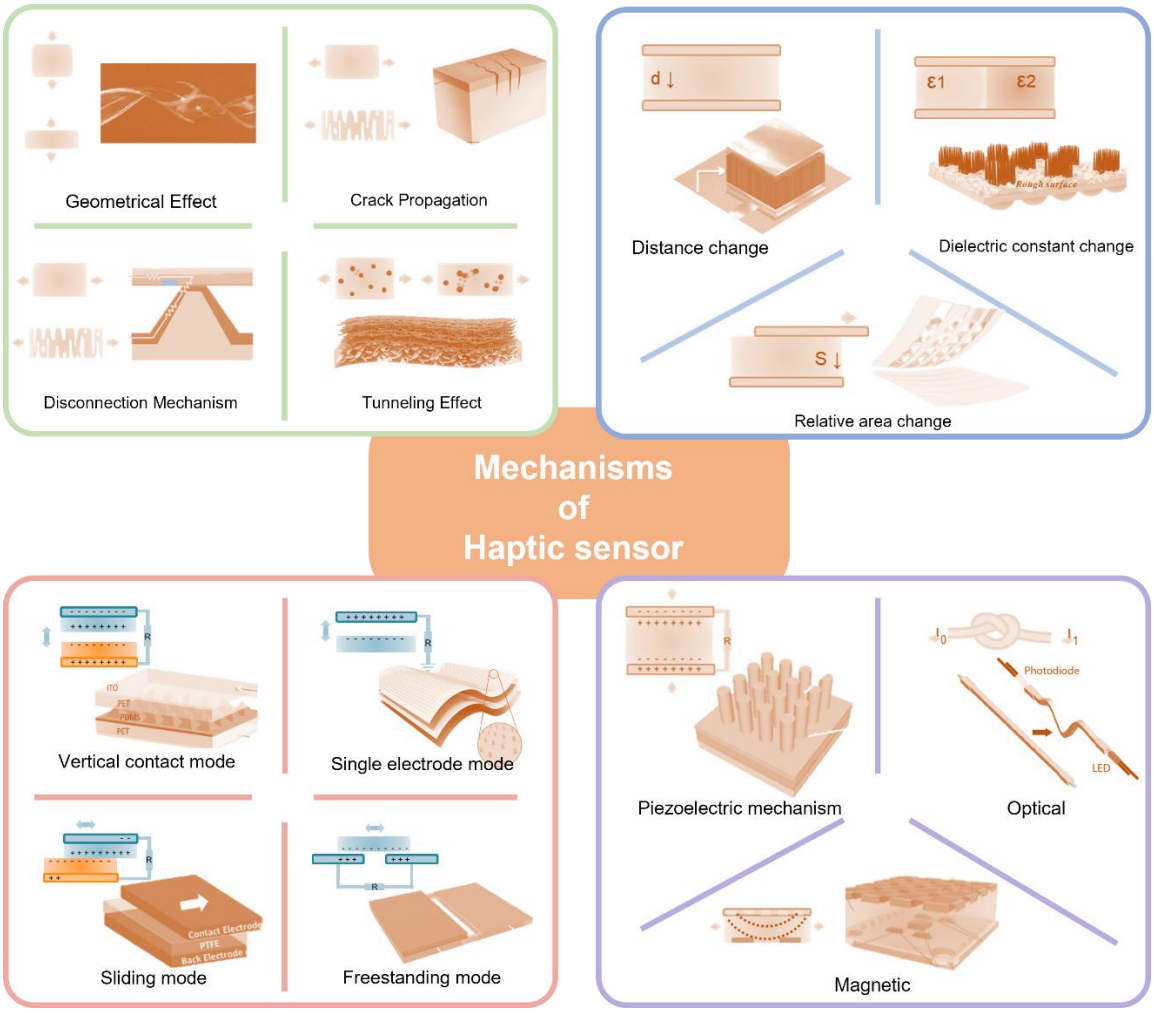

Figure 2.3 Different sensing mechanisms of tactile force sensors, including piezoresistive, capacitive, piezoelectric/triboelectric, light and magnet. Reproduced with permission from ref.[16]. Copyright 2009 Wiley. Reproduced with permission from ref.[17]. Copyright 2014 Wiley. Reproduced with permission from ref.[18]. Copyright 2014 Springer Nature. Reproduced with permission from ref[19]. Copyright 2020 Springer Nature. Reproduced with permission from ref.[20]. Copyright 2016 Wiley. Reproduced with permission from ref.[21]. Copyright 2020 American Chemical Society. Reproduced with permission from ref.[22]. Copyright 2021 Wiley. Reproduced with permission from ref.[23]. Copyright 2012 American Chemical Society. Reproduced with permission from ref.[24]. Copyright 2014 American Chemical Society. Reproduced with permission from ref.[25]. Copyright 2014 Wiley. Reproduced with permission from ref.[26]. Copyright 2014 Wiley. Reproduced with permission from ref[27]. Copyright 2015 Springer Nature. Reproduced with permission from ref[28]. Copyright 2016 American Association for the Advancement

of Science. Reproduced with permission from ref[29]. Copyright 2024 MDPI, Basel, Switzerland.

2.2.2 Flexible tactile sensors for object classification

In recent years, advancements in tactile sensing systems have significantly enhanced our ability to recognize and interact with objects in various environments. These systems, which mimic the sense of touch, provide critical information about an object's shape, texture, stiffness, and other properties. This capability is particularly valuable in robotics, prosthetics, and human-computer interaction, where accurate object recognition can lead to more interactive and responsive systems.

Recent innovations in tactile sensing have led to the development of highly sensitive and precise systems. Zhao et al. developed stretchable optical waveguides for strain sensing in prosthetic hands. These photonic sensors, known for easy fabrication, chemical inertness, low hysteresis, and high precision, were used as curvature, elongation, and force sensors in a fiber-reinforced soft prosthetic hand[28]. Shi et al. created an iontronic e-skin with a dense array of sensing elements, offering high sensitivity and real-time pressure mapping without crosstalk[30]. Zhang et al. developed a biomimetic e-skin for robots, combining triboelectric and piezoresistive elements for dynamic and static pressure sensing. Using a microstructure-enhanced template method, the BES achieved high sensitivity and a wide detection range. Multimodal sensing systems are utilized for more complicated application scenarios[31]. Liu et al. introduced a tactile-olfactory sensing array for a mechanical hand, allowing real-time detection of an object's topography, stiffness, and odor. Using a bioinspired machine-learning approach, this system mimics neural processes in animals, potentially aiding in human identification[32].

The future of tactile sensing systems for object recognition looks promising, with continued advancements expected in sensor sensitivity, integration, and data processing capabilities. Innovations in materials and fabrication techniques will likely result in more durable and versatile tactile sensors, capable of withstanding diverse environmental conditions. The

integration of machine learning algorithms will further enhance the ability of these systems to accurately interpret complex tactile data, enabling more nuanced and sophisticated object recognition. As these technologies evolve, we can anticipate their broader application in areas such as robotics, assistive devices, and virtual reality, providing more natural and interactive interactions between humans and machines.

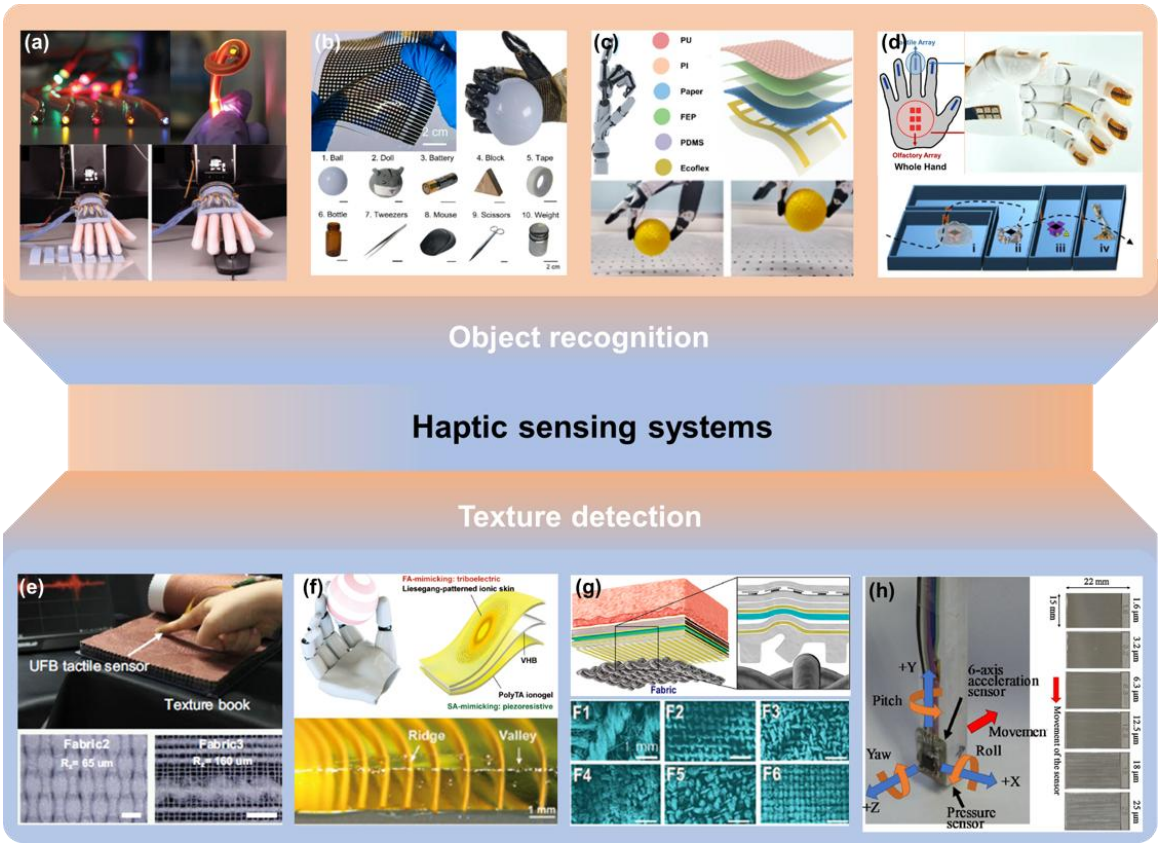

Figure 2.4 Tactile sensing systems for object recognition and tactile sensing systems. (a) Soft prosthetic hand using optical waveguides. Reproduced with permission from ref. [28]. Copyright 2016 American Association for the Advancement of Science (b) Iontronic skins for object classification. Reproduced with permission from ref.[30]. Copyright 2020 American Association for the Advancement of Science. (c) Triboelectric-piezoresistive based robotic hands. Reproduced with permission from ref.[31]. Copyright 2024 American Chemical Society. (d) Bimodal sensing array for robust object recognition. Reproduced with permission from ref.[32]. Copyright 2022 Springer Nature. (e)Piezoelectric skin tele-tactile system for texture classification. Reproduced with permission from ref.[33]. Copyright 2022 Springer Nature. (f) Ionic skin for fingertip-like tactile sensation. Reproduced with permission from ref.[34]. Copyright 2011 Wiley. (g) Bimodal-sensitive

tactile systems. Reproduced with permission from ref.[35]. Copyright 2023 American Chemical Society. (h) CNN-based tactile sensor system for roughness recognition. Reproduced with permission from ref.[36]. Copyright 2019 Elsevier.

2.2.3 Flexible tactile sensors for texture sensing

Texture sensing is a critical component of tactile feedback systems, enabling machines to discern fine details about surface properties. This capability is essential for applications in robotics, prosthetics, and virtual environments, where understanding and interacting with various textures can enhance precision and realism. Advanced tactile systems that can accurately detect and interpret texture differences allow for more interactive and effective interactions between humans and machines.

Recent advancements in tactile sensing technologies have demonstrated significant potential for enhancing texture sensing capabilities. Jin et al. developed a skin-attachable, untethered tactile system featuring an ultra-flexible bimodal tactile sensor and a flexible tactile actuator array. This system can capture and replicate tactile stimuli with high spatial resolution, offering a sophisticated and immersive tactile interface[33]. Qiao et al. introduced an ionic skin inspired by fingertip structures, featuring stiff ridges in a soft hydrogel matrix. This design enables strain-undisturbed dynamic pressure sensing and texture recognition, mimicking the multimodal sensations of human fingers[34]. Chun et al. proposed a self-powered neural tactile sensor (NTS) that accurately mimics human finger skin. It integrates a pressure sensor array and a triboelectric nanogenerator (TENG) for detecting both pressure and vibration, achieving 99.1% accuracy in classifying complex fabric patterns[35]. Tsuji et al. presented a tactile sensor system using a convolutional neural CNN to recognize surface roughness. The system, which includes a pressure sensor and a six-axis acceleration sensor, analyzes time-series data to determine roughness, achieving up to 71% recognition accuracy with a simple and cost-effective design[36].

The future of tactile sensing systems for texture sensing is promising, with ongoing advancements in sensor technology, materials science, and data processing. Future

developments are likely to focus on enhancing the sensitivity and specificity of these systems, enabling more precise detection and differentiation of textures. Innovations in flexible and stretchable materials will improve the durability and adaptability of tactile sensors, making them suitable for a wider range of applications, including wearable devices and soft robotics. Additionally, the integration of advanced machine learning algorithms will allow for more sophisticated interpretation of sensory data[37, 38], improving the accuracy and reliability of texture recognition. As these technologies continue to evolve, we can expect tactile sensing systems to become increasingly integral to fields such as virtual reality, telemedicine, and robotic-assisted surgery, where nuanced tactile feedback is crucial for user experience and functionality.

2.3 Intelligent tactile systems

In the era of the Fourth Industrial Revolution (Industry 4.0), vast amounts of data—encompassing IoT data, cybersecurity data, mobile data, business data, social media data, and health data—are being generated. The intelligent analysis of this data and the creation of smart, automated applications rely heavily on knowledge in artificial intelligence (AI), particularly machine learning (ML). This field brings together concepts from various disciplines, including artificial intelligence, probability and statistics, computer science, information theory, psychology, control theory, and philosophy. In machine learning, techniques such as classification analysis, regression, data clustering, feature engineering, dimensionality reduction, association rule learning, and reinforcement learning are employed to build effective data-driven systems. The convergence of AI and tactile sensing systems heralds a new era of innovation, overcoming past limitations and endowing human-machine interfaces (HMIs) and robotics with cognitive capabilities for perception, learning, and intelligent decision-making. Overall, integrating AI into artificial sensing systems leads to unprecedented advancements in applications of HMIs and robotics.

2.3.1 Machine learning algorithms

AI, ML, and deep learning (DL)[39] are essential in artificial sensing systems for complicated task in various scenarios. ML models and artificial neural networks, including DL, are integral to the field of robotics, as illustrated in Figure 47. Within machine learning, basic methods and artificial neural networks are further divided into shallow and deep neural networks. Traditional ML algorithms encompass techniques such as Support Vector Machines (SVM), decision trees, k-Nearest Neighbors (kNNs), and Adaboost. The random forest (RF) model, which comprises multiple decision trees, utilizes a "parallel ensembling" approach. This method involves fitting several decision tree classifiers in parallel on different subsets of data and aggregating their predictions through majority voting or averaging to produce a final result.

In sensor-related research, supervised learning techniques, particularly kNNs, SVM, and supervised deep learning models, are predominantly used. These algorithms are primarily employed for classification tasks, enabling robots to distinguish between various objects upon contact. Unlike random forests, which use parallel ensembling, Adaboost employs a "sequential ensembling" technique. It creates a strong classifier by combining multiple weak classifiers, iteratively focusing on misclassified data points to improve accuracy.

Deep learning algorithms encompass a range of architectures, including Convolutional Neural Networks (CNNs), Recurrent Neural Networks (RNNs), Multilayer Perceptrons (MLPs), Autoencoders, and Transformers[39-41]. CNNs are particularly effective for image recognition tasks due to their ability to capture spatial patterns within data. This makes them ideal for analyzing sensor data with two-dimensional arrays, such as electronic skin (e-skin) applications, where they are used for tasks like object contact classification. RNNs, including their advanced variant Long Short-Term Memory (LSTM) networks, are adept at processing sequential data, making them invaluable for tasks such as speech recognition and natural language processing. These algorithms excel in handling time-series data, making them suitable for time-series classification and execution tasks in robotics. MLPs are versatile neural networks used for a variety of tasks, including classification and regression[42]. They are sensitive to feature scaling and offer numerous tunable hyperparameters, such as the number of hidden layers, neurons, and training iterations.

This flexibility allows MLPs to model complex relationships in data, but it also means they can be computationally intensive. Autoencoders are a type of unsupervised learning model used for feature learning and data compression. They work by encoding input data into a lower-dimensional representation and then decoding it back to reconstruct the original input. This process is particularly useful for tasks such as anomaly detection, data denoising, and dimensionality reduction. Transformers[43], known for their attention mechanisms, have revolutionized natural language processing tasks, particularly in machine translation, text summarization, and text generation. Their ability to focus on different parts of the input data when making predictions has made them a powerful tool for understanding and generating human language.

The integration of these ML and DL techniques in robotics has significantly enhanced the capabilities of robots, enabling them to perform complex tasks with greater intelligence, autonomy, and efficiency. This convergence of advanced algorithms and robotics technology is paving the way for innovative applications across various industries, from manufacturing and healthcare to service and entertainment sectors.

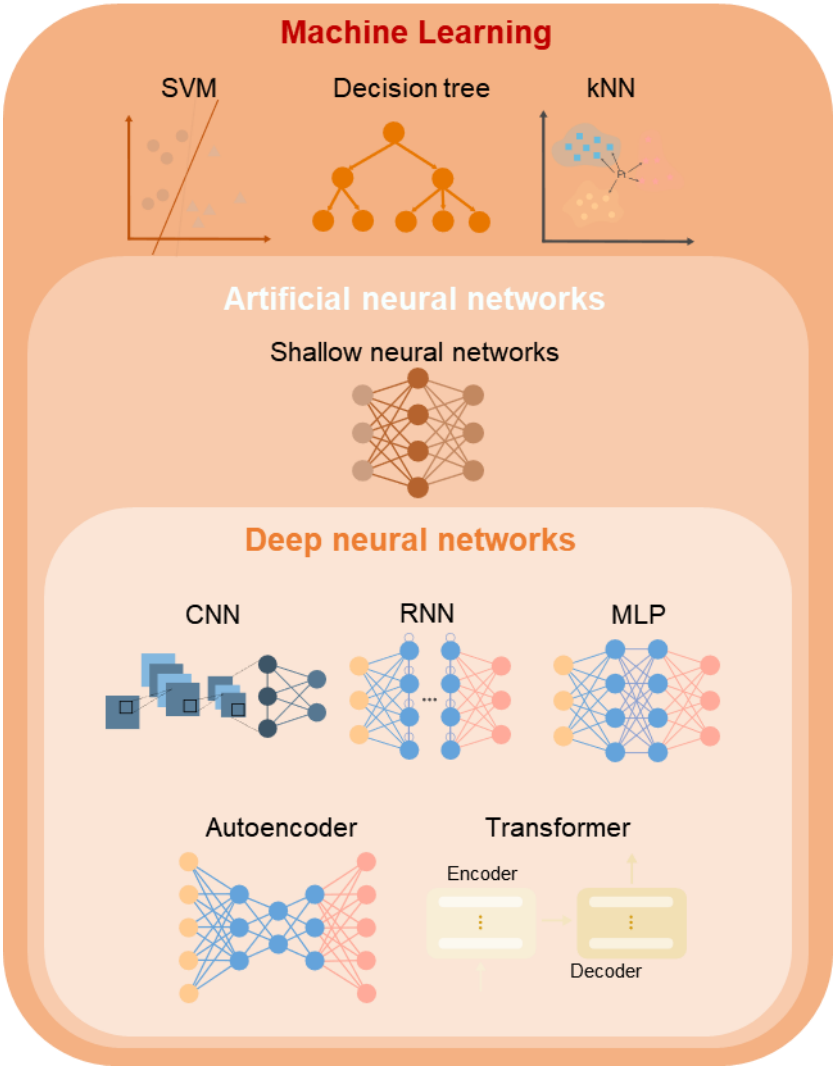

Figure 2.5 Venn diagram of machine learning algorithms learning concepts and classes.

2.3.2 Machine learning-empowered intelligent tactile systems

Tactile sensing systems have seen significant advancements in recent years, largely driven by the integration of sophisticated machine learning techniques. These systems, which mimic the human sense of touch, are increasingly being utilized in various applications, from gesture recognition and facial expression decoding to sign language translation and robotic manipulation. By leveraging different machine learning methods, such as convolutional neural networks and sparse neural networks, these systems can efficiently process and integrate data from various sensors, including stretchable strain sensors,

piezoelectric thin films, and yarn-based sensor arrays. This fusion of tactile data with machine learning algorithms enables precise and real-time interpretation of complex physical interactions, enhancing the capabilities of both wearable and robotic technologies. The development of such systems, as demonstrated by recent studies, highlights the potential for tactile technologies to revolutionize fields like medical diagnostics, assistive devices, and human-computer interaction.

Wang et al. developed a bioinspired system for human gesture recognition that combines visual data with somatosensory data from stretchable strain sensors made of single-walled carbon nanotubes. The system uses a convolutional neural network for visual data processing and a sparse neural network for integrating sensor data at the feature level[44]. Sun et al. designed a system for decoding facial strains and predicting facial movements using mass-manufacturable piezoelectric thin films. The system includes multiphysics modeling for analyzing device interactions with the skin and 3D digital image correlation for dynamic surface reconstruction. It successfully decodes facial movements in both healthy individuals and ALS patients[45]. Zhou et al. demonstrated a wearable system for translating American Sign Language into speech. The system uses yarn-based stretchable sensor arrays and a wireless circuit board, achieving a 98.63% recognition rate and less than 1-second recognition time[46]. Shu et al. introduced a shape-sensing electronic skin (SSES) that allows soft robots to detect and reconstruct their shape during movement, providing proprioception. The system also uses machine learning to recognize different terrains, enhancing robotic autonomy in complex environments[47]. Kireev et al. developed a continuous blood pressure monitoring platform using graphene electronic tattoos, offering accurate and non-invasive BP readings for over 300 minutes. The system records diastolic and systolic pressures with high accuracy[48]. Li et al. integrated quadruple tactile sensors into a robotic hand for precise object recognition through grasping. The sensors detect thermal conductivity, contact pressure, and temperature, enabling the robot to accurately classify various objects, including for tasks like garbage sorting[49].

The future of tactile sensing systems is poised to expand into even more sophisticated and versatile applications, driven by ongoing advancements in materials science, sensor

technologies, and machine learning algorithms. One promising direction is the development of more adaptive and intelligent systems capable of learning and refining their sensory perceptions in real-time, akin to human sensory adaptation. This could be achieved through the integration of advanced neural networks and deep learning techniques, enabling these systems to handle increasingly complex and dynamic environments. Moreover, the miniaturization and enhanced sensitivity of sensors, such as graphene-based electronic tattoos and multilayer microstructures, will likely lead to more comfortable and unobtrusive wearable devices. These innovations could significantly impact healthcare, providing continuous monitoring and early detection of physiological changes. Additionally, the improvement in robotic tactile feedback systems will enhance human-robot interaction, enabling robots to perform delicate tasks with greater precision. As these technologies evolve, ethical considerations and data privacy issues will also need to be addressed, particularly in applications involving sensitive personal data. Overall, the integration of machine learning with tactile sensing systems holds immense potential for creating more interactive and responsive technologies across various domains.

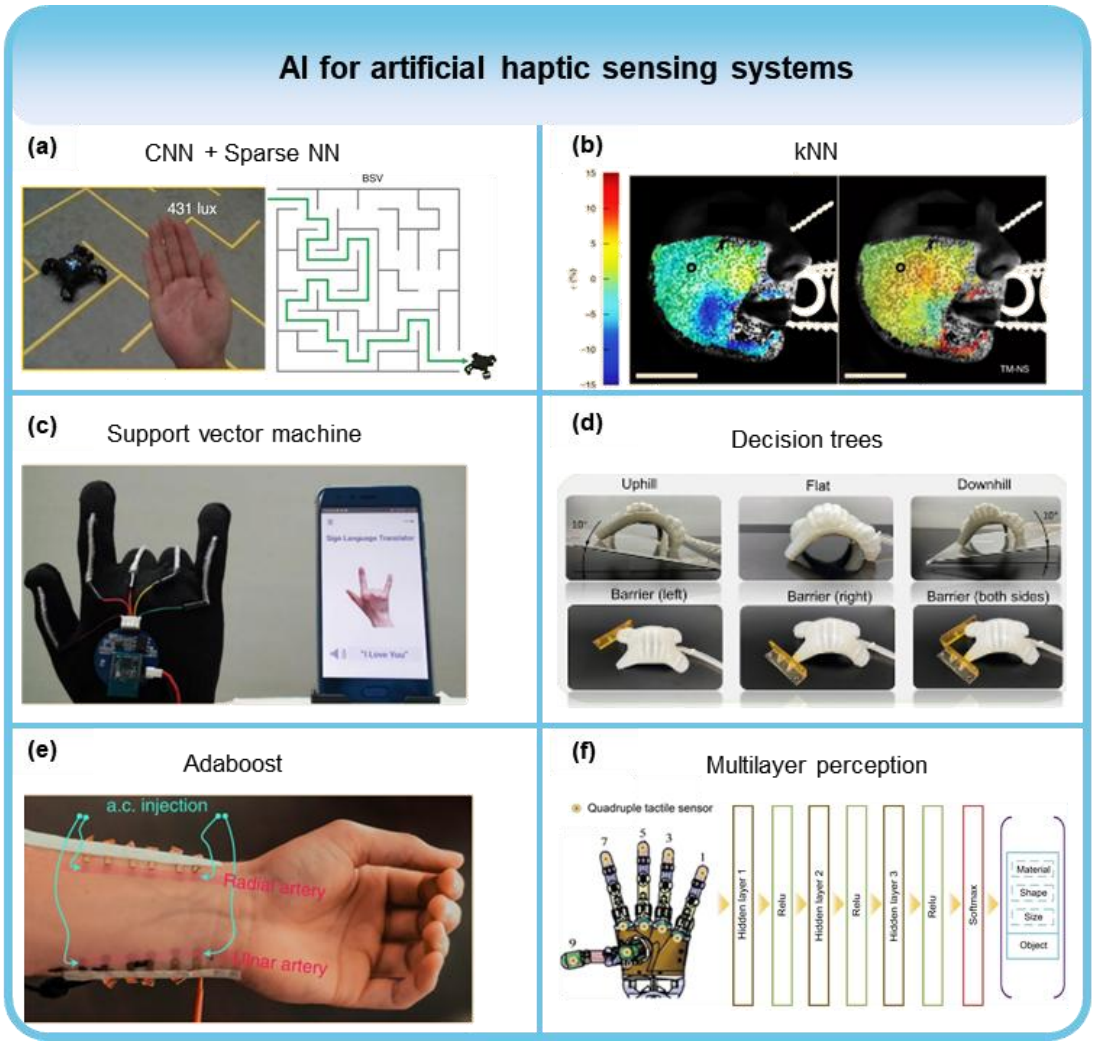

Figure 2.6 AI for artificial tactile sensing systems. (a) CNN + Sparse NN for gesture recognition. Reproduced with permission from ref.[44]. Copyright 2020 Springer Nature. (b) kNN for expression recognition. Reproduced with permission from ref.[45]. Copyright 2020 Springer Nature. (c) SVM for sign language recognition. Reproduced with permission from ref.[46]. Copyright 2020 Springer Nature. (d) Decision trees for texture recognition. Reproduced with permission from ref.[47]. Copyright 2023 Wiley. (e) Adaboost for blood pressure monitoring. Reproduced with permission from ref.[48]. Copyright 2022 Springer Nature. (f) Multilayer perception for object detection. Reproduced with permission from ref.[49]. Copyright 2020 American Association for the Advancement of Science

2.4 Applications of intelligent tactile systems

The development of intelligent tactile systems has unlocked a myriad of applications across various fields, with particularly significant impacts in medical palpation and robotics. These advanced systems integrate high-resolution sensing technologies, machine learning algorithms, and real-time data processing to achieve precise and versatile touch-based interactions. Advancements in intelligent tactile systems are paving the way for transformative applications in both medical palpation and robotics[50-52]. In medical palpation, these systems offer the potential to revolutionize diagnostic procedures by providing more accurate, reliable, and non-invasive methods for detecting and assessing various conditions. The integration of tactile sensing with robotic tools enhances surgical precision and safety, leading to improved patient outcomes. In robotics, the incorporation of tactile sensing capabilities significantly expands the functional range of robots. The ability to perceive and respond to tactile information enables robots to perform more complex and delicate tasks, making them invaluable in industries ranging from manufacturing to healthcare[53]. As these technologies continue to evolve, we can expect even more innovative applications that leverage the sophisticated capabilities of intelligent tactile systems, ultimately enhancing the quality of life and advancing various technological frontiers.

Palpation is a fundamental clinical technique employed by healthcare professionals to examine the body through the sense of touch. This method enables doctors to evaluate the size, shape, firmness, and position of various body parts, as well as to detect abnormalities such as lumps, swelling, tenderness, or changes in texture. Palpation is integral in diagnosing somatic issues, formulating treatment plans, and assessing the outcomes of treatments. By accurately identifying the specific tissues involved in a patient's complaint, clinicians can tailor the rest of the evaluation to address the affected areas appropriately. Understanding the importance of palpation is crucial for medical students, as it can significantly enhance their diagnostic and evaluation skills[54]. Despite this, over the past three decades, there has been a growing reliance on advanced technology in medical practice, leading some to question the relevance and value of physical examinations, including palpation, in contemporary patient care.

To gauge the current perspective on physical examinations, a structured online survey was conducted with 2,684 practicing clinicians of varying ages and from multiple countries. The results showed that 70% of the respondents believed that physical examinations were "almost always valuable" in acute general medical referrals. Specifically, the survey indicated that most doctors (over 70%) found palpation techniques—such as abdominal palpation for tenderness, palpation of arterial pulses, and abdominal palpation and percussion for assessing spleen size—both useful and essential in clinical practice[55].

The need for digital palpation arises from several challenges associated with traditional palpation methods. One key issue is the subjectivity and variability inherent in traditional palpation, which heavily relies on the clinician's experience and skill level. This dependence can lead to subjective interpretations and varying findings, as different practitioners may have different levels of sensitivity and may interpret physical signs differently. Additionally, traditional palpation has limited sensitivity; human fingers naturally have limitations in detecting subtle differences in tissue properties, such as minor variations in texture, elasticity, or temperature. These limitations can sometimes result in missed diagnoses or an inability to detect early signs of certain conditions. Finally, quantification challenges are another significant issue, as manual palpation often lacks the precision needed to accurately measure findings. For example, assessing the exact size of a lump or the degree of tenderness can be challenging without objective measurement tools, leading to inconsistencies and affecting the reproducibility of clinical assessments. Digital palpation technologies can address these challenges by providing more objective, sensitive, and quantifiable data, enhancing the accuracy and reliability of clinical evaluations.

Given these challenges, the development of digital palpation technologies is becoming increasingly important. These technologies can provide objective, quantifiable data that complement the clinician's sensory input, enhancing diagnostic accuracy and consistency. Digital palpation tools can also overcome the limitations of human touch, offering greater sensitivity and specificity in detecting subtle tissue changes. Additionally, such technologies can standardize the assessment process, reducing variability and improving the reliability of findings across different practitioners.

The human breast is primarily composed of glandular tissue, fatty tissue, and connective tissue. The glandular tissue, which includes lobes and lobules, is responsible for milk production, while the fatty tissue gives the breast its shape and volume. Ducts transport milk to the nipple, and the breast also contains blood vessels, lymph nodes, and nerves that are supported by connective tissue[56, 57].

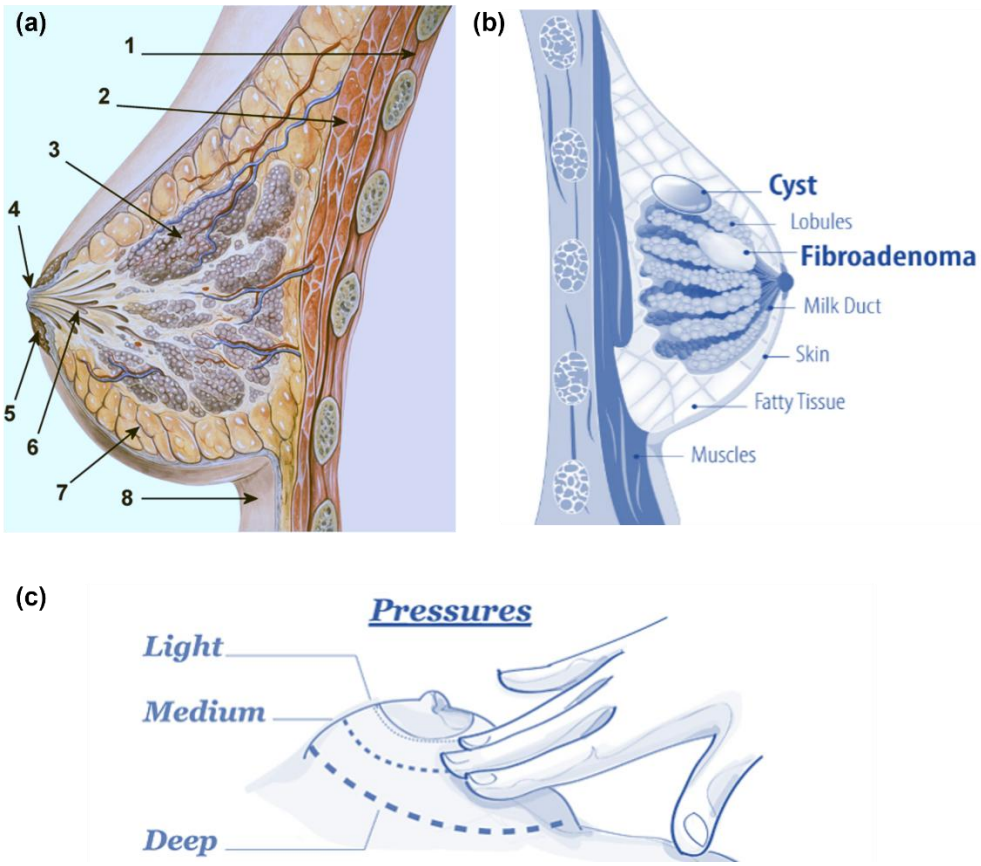

Figure 2.7 (a) Schematic diagrams of the ductal anatomy of the breast. Structure of human breasts[57]. 1. Chest wall. 2. Pectoral muscles. 3. Lobules. 4. Nipple surface. 5. Areola. 6. Lactiferous duct. 7. Fatty tissue. 8. Skin. (b) Schematic diagrams of breast nodules, including cyst, fibroadenoma, and tumor. (c) Schematic figures for palpation on human breast.

In this context, nodules, or lumps, can form within the breast and vary widely in size, texture, and mobility. These nodules may be benign, such as cysts or fibroadenomas, or malignant, indicating the presence of breast cancer. The early detection and accurate

characterization of these nodules are crucial for effective treatment and management, as identifying potential issues early significantly improves patient outcomes.

Palpation is a key manual examination technique used by healthcare providers to evaluate the breast for abnormalities. This process involves feeling the breast tissue to detect any lumps, changes in texture, or areas of tenderness. Palpation remains an essential part of routine breast exams and is instrumental in identifying potential problems early on.

Looking forward, the advent of quantitative digital palpation technologies presents an exciting advancement in breast cancer detection. These technologies can offer precise measurements of nodules, including their size, texture, and elasticity, which are often challenging to assess accurately with manual palpation alone. By providing objective and quantifiable data, digital palpation tools can enhance the accuracy of breast examinations, facilitating earlier detection of tumors. This improved detection capability can lead to more timely and effective interventions, ultimately benefiting patient outcomes. Additionally, digital palpation can contribute to standardizing breast exams, reducing variability in assessments, and improving overall diagnostic reliability.

Wearable human-machine interfaces (HMIs), such as smart gloves, have gained significant attention recently. The effectiveness of these technologies in enhancing interactions with both real and virtual environments hinges on their ability to provide interactive, real-time tactile feedback. This review examines various smart glove solutions and their applications in interaction, rehabilitation, virtual reality (VR), augmented reality (AR), and augmentative and alternative communication[58]. Initially, these systems relied on commercial touch sensors and displays, but recent developments focus on electronic skin (e-skin) technologies with integrated touch sensing and vibrotactile actuation. These advancements offer a richer user experience and greater comfort. The review also discusses the challenges and benefits of these technologies, including their potential for improving robotics, healthcare, sensory augmentation, and tactile internet applications.

In terms of pressure sensing gloves, Sundaram et al. utilized a scalable tactile glove equipped with deep convolutional neural networks to demonstrate that sensors distributed uniformly across the hand can identify objects, estimate their weight, and explore tactile patterns during object handling. The glove, with 548 sensors embedded in a knitted fabric and connected by conductive threads, captured a comprehensive dataset of 135,000 frames from interactions with 26 different objects, highlighting key correlations between hand regions during manipulation[59]. This research offers insights into the design of prosthetics, robotic grasping tools, and human–robot interactions by mimicking natural mechanoreceptor networks. Cui et al. developed a force-softness bimodal sensor (FSS) array for wearable tactile platforms, enabling a glove with 112 FSSs to distinguish body features using machine learning. The FSS sensors, enhanced with a protrusion atop piezoresistive elements, can discern pressure and softness simultaneously[60]. Chen et al. reported a neuromorphic tactile system that uses a spike timing mechanism for rapid object classification, with a time resolution of 1.2 ms. This system integrates a tactile spiking neural network (t-SNN) for dynamic feature extraction and robust performance, demonstrating real-time object classification through a biological motor nerve-like perception-actuation loop[61]. Gao et al. introduced a microfluidic tactile sensor based on a diaphragm pressure sensor design, leveraging an embedded Wheatstone bridge circuit to achieve high sensitivity and temperature compensation[62].

In addition to gloves based solely on pressure sensing, there are also other gloves that combine strain sensors for bending detection for object interaction or gesture recognition. Tashakori et al. showcased smart textile gloves with stretchable helical sensor yarns, achieving precise hand movement tracking with minimal error, surpassing conventional systems' accuracy and overcoming limitations such as occlusion and setup times[63]. Zhou et al. developed a wearable sign-to-speech translation system using triboelectric signals to convert sign language into audio speech with high accuracy and durability, capable of recognizing 660 ASL gestures with a 98.63% success rate[46].

Based on the sensor gloves, the feedback system will expand the application scenarios of smart gloves. Sui et al. presented a portable rehabilitation glove with real-time sensory

feedback and a closed-loop control system for diverse finger motion sensing, employing Hall sensors and SMA actuators[64]. Zhou et al. also proposed a smart glove with triboelectric-based sensors and piezoelectric stimulators for multidirectional detection and tactile feedback, achieving 96% accuracy in object recognition through machine learning, and demonstrating potential applications in various fields such as entertainment, healthcare, and sports training[65].

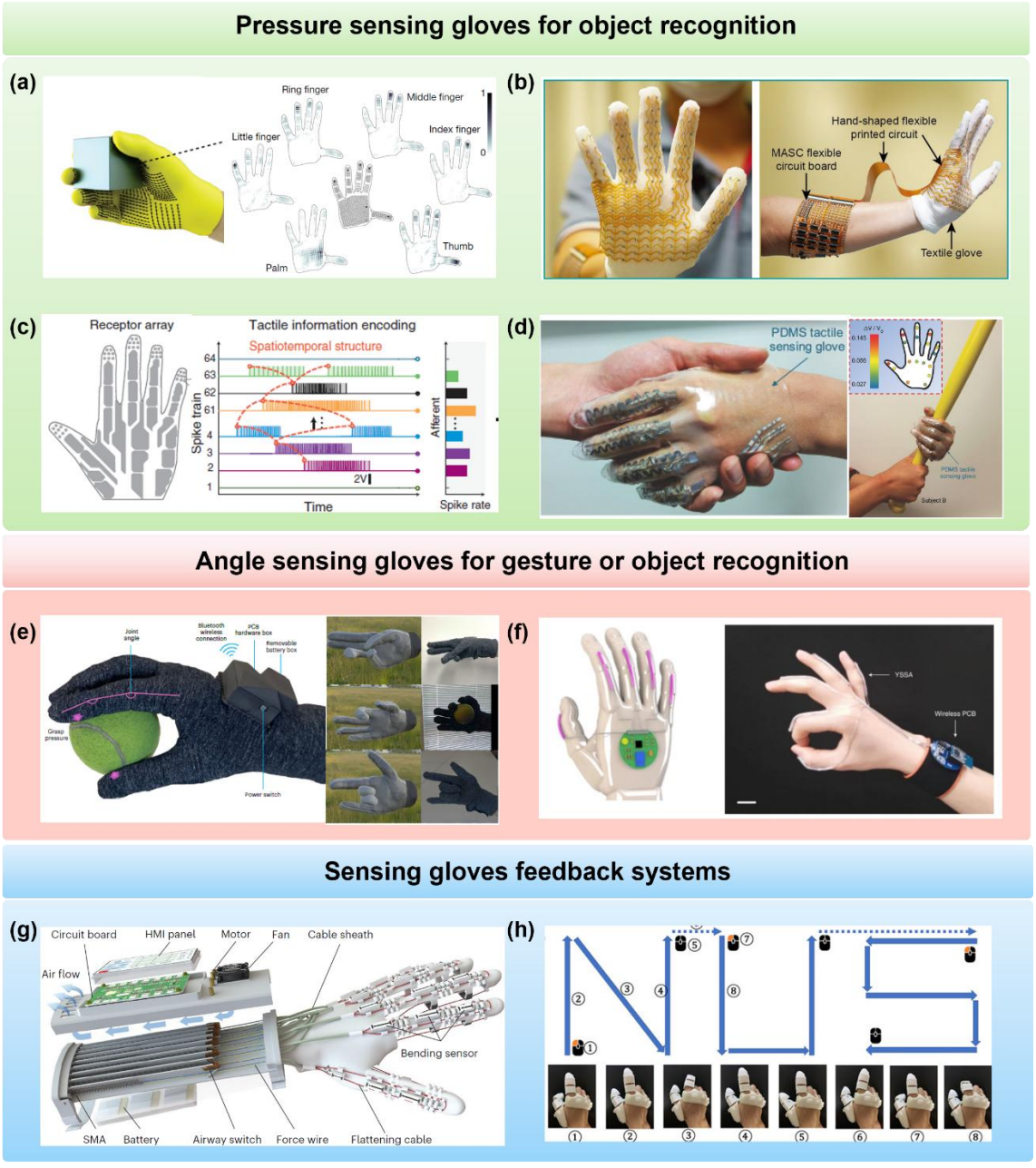

Figure 2.8 Tactile sensing gloves. (a) A scalable tactile glove human grasp classification. Reproduced with permission from ref. [59]. Copyright 2019 Springer Nature. (b) Bimodal sensing data for tactile body-feature identification. Reproduced with permission from ref. [60]. Copyright 2022 Wiley. (c) Tactile glove enabling dynamic object classification. Reproduced with permission from ref. [61]. Copyright 2024 American Association for the Advancement of Science (d) Tactile gloves for Health and Tactile Touch Monitoring. Reproduced with permission from ref.[62]. Copyright 2017 Wiley. (e) Smart textile gloves for object interaction. Reproduced with permission from ref.[63]. Copyright 2024 Springer Nature. (f) Stretchable sensor arrays on hands for sign-to-speech. Reproduced with permission from ref.[46]. Copyright 2020 Springer Nature. (g) A portable rehabilitation gloves. Reproduced with permission from ref.[64]. Copyright 2023 Springer Nature. (h) Smart gloves both sensing and feedback for VR/AR. Reproduced with permission from ref.[65]. Copyright 2020 American Association for the Advancement of Science.

The recent advancements in tactile glove technology highlight a promising trajectory for HMI and robotics. Cutting-edge sensor arrays, including piezoresistive, triboelectric, and neuromorphic systems, provide detailed tactile feedback and accurate object recognition, which are essential for enhancing the dexterity and sensitivity of robotic systems. This makes them better equipped for delicate tasks and improves their interaction with humans. The incorporation of machine learning and deep learning algorithms to process sensory data further boosts the adaptability and intelligence of these systems, enabling more nuanced and context-aware responses. Tactile gloves are therefore set to become pivotal in a wide range of applications, from prosthetics and rehabilitation to virtual reality and beyond. Ongoing research and development are likely to lead to even more sophisticated HMI solutions, narrowing the gap between human sensory experiences and machine capabilities, and paving the way for more interactive and effective human-robot collaborations.

References

[1] Mostafavi Yazdi SJ, Baqersad J. *Journal of Biomechanics.* **2022**, 130, 110864.

[2] Graham HK, Eckersley A, Ozols M, Mellody KT and Sherratt MJ. 2019;1.

[3] Liu Y, Pharr M, Salvatore GA. *ACS Nano.* **2017**, 11, 9614.

[4] Catton WT. *Physiological Reviews.* **1970**, 50, 297-318.

[5] Johnson KO. *Current Opinion in Neurobiology.* **2001**, 11, 455.

[6] Chortos A, Liu J, Bao Z. *Nature Materials.* **2016**, 15, 937.

[7] Iheanacho, F., & Vellipuram, A. R. (2023). Physiology, Mechanoreceptors. *In StatPearls*., PMID: 31082112

[8] Park J, Kim M, Lee Y, Lee HS and Ko H. *Science Advances.* 1, e1500661.

[9] Chun K-Y, Son YJ, Jeon E-S, Lee S and Han C-S. *Advanced Materials.* **2018**, 30, 1706299.

[10] Loewenstein WR, Mendelson M. *J Physiol.* **1965**, 177, 377.

[11] Lee Y, Park J, Choe A, Cho S, Kim J and Ko H. *Advanced Functional Materials.* **2020**, 30, 1904523.

[12] Liu E, Cai Z, Ye Y, Zhou M, Liao H and Yi Y. *Sensors* **2023**, 23, 81.

[13] Luo Y, Abidian MR, Ahn J-H, Akinwande D, Andrews AM, Antonietti M, Bao Z, Berggren M, Berkey CA, Bettinger CJ, Chen J, Chen P, Cheng W, Cheng X, Choi S-J, Chortos A, Dagdeviren C, Dauskardt RH, Di C-A, Dickey MD, Duan X, Facchetti A, Fan Z, Fang Y, Feng J, Feng X, Gao H, Gao W, Gong X, Guo CF, Guo X, Hartel MC, He Z, Ho JS, Hu Y, Huang Q, Huang Y, Huo F, Hussain MM, Javey A, Jeong U, Jiang C, Jiang X, Kang J, Karnaushenko D, Khademhosseini A, Kim D-H, Kim I-D, Kireev D, Kong L, Lee C, Lee N-E, Lee PS, Lee T-W, Li F, Li J, Liang C, Lim CT, Lin Y, Lipomi DJ, Liu J, Liu K, Liu N, Liu R, Liu Y, Liu Y, Liu Z, Liu Z, Loh XJ, Lu N, Lv Z, Magdassi S, Malliaras GG, Matsuhisa N, Nathan A, Niu S, Pan J, Pang C, Pei Q, Peng H, Qi D, Ren H, Rogers JA, Rowe A, Schmidt OG, Sekitani T, Seo D-G, Shen G, Sheng X, Shi Q, Someya T, Song Y, Stavrinidou E, Su M, Sun X, Takei K, Tao X-M, Tee BCK, Thean AV-Y, Trung TQ, Wan C, Wang H, Wang J, Wang M, Wang S, Wang T, Wang ZL, Weiss PS, Wen H, Xu S, Xu T, Yan H, Yan X, Yang H, Yang L, Yang S, Yin L, Yu C, Yu G, Yu J, Yu S-H, Yu X, Zamburg E, Zhang H, Zhang X, Zhang X, Zhang X, Zhang Y, Zhang Y, Zhao S, Zhao

X, Zheng Y, Zheng Y-Q, Zheng Z, Zhou T, Zhu B, Zhu M, Zhu R, Zhu Y, Zhu Y, Zou G, Chen X. *ACS Nano.* **2023**, 17, 5211.

[14] Chen H, Zhuo F, Zhou J, Liu Y, Zhang J, Dong S, Liu X, Elmarakbi A, Duan H and Fu Y. *Chemical Engineering Journal.* **2023**, 464, 142576.

[15] Yang T, Xie D, Li Z and Zhu H. *Materials Science and Engineering: R: Reports.* **2017**, 115, 1.

[16] So J-H, Thelen J, Qusba A, Hayes GJ, Lazzi G and Dickey MD. *Adv Funct Mater.* **2009**, 19, 3632.

[17] Choong C-L, Shim M-B, Lee B-S, Jeon S, Ko D-S, Kang T-H, Bae J, Lee SH, Byun K-E, Im J, Jeong YJ, Park CE, Park J-J and Chung UI. *Advanced Materials.* **2014**, 26, 3451.

[18] Kang D, Pikhitsa PV, Choi YW, Lee C, Shin SS, Piao L, Park B, Suh K-Y, Kim T-I and Choi M. *Nature.* **2014**, 516, 222.

[19] Tan C, Dong Z, Li Y, Zhao H, Huang X, Zhou Z, Jiang J-W, Long Y-Z, Jiang P, Zhang T-Y and Sun B. *Nature Communications.* **2020**, 11, 3530.

[20] Nassar JM, Cordero MD, Kutbee AT, Karimi MA, Sevilla GaT, Hussain AM, Shamim A and Hussain MM. *Advanced Materials Technologies.* **2016**, 1, 1600004.

[21] Zhang Y, Liu S, Miao Y, Yang H, Chen X, Xiao X, Jiang Z, Chen X, Nie B and Liu J. *ACS Applied Materials & Interfaces.* **2020**, 12, 27961.

[22] Ji B, Zhou Q, Hu B, Zhong JW, Zhou J and Zhou BP. *Advanced Materials.* **2021**, 33, e2100859.

[23] Fan FR, Lin L, Zhu G, Wu WZ, Zhang R and Wang ZL. *Nano Lett.* **2012**, 12, 3109.

[24] Zhu G, Yang WQ, Zhang T, Jing Q, Chen J, Zhou YS, Bai P and Wang ZL. *Nano Lett.* **2014**, 14, 3208.

[25] Zhu G, Zhou YS, Bai P, Meng XS, Jing Q, Chen J and Wang ZL. *Advanced Materials.* **2014**, 26, 3788.

[26] Wang S, Xie Y, Niu S, Lin L and Wang ZL. *Advanced Materials.* **2014**, 26, 2818.

[27] Choi Y-Y, Yun TG, Qaiser N, Paik H, Roh HS, Hong J, Hong S, Han SM and No K. *Sci Rep.* **2015**, 5, 10728.

[28] Zhao H, O'brien K, Li S and Shepherd RF. *Science Robotics.* **2016**, 1, eaai7529.

[29] Dai H, Wu Z, Meng C, Zhang C and Zhao P. *Magnetochemistry* 2024, 10, 6.

[30] Shi J, Dai Y, Cheng Y, Xie S, Li G, Liu Y, Wang J, Zhang R, Bai N, Cai M, Zhang Y, Zhan Y, Zhang Z, Yu C and Guo CF. *Science Advances.* **2023,** 9, eadf8831.

[31] Zhang H, Li H, Li Y. *Nano Letters.* **2024**, 24, 4002.

[32] Liu M, Zhang Y, Wang J, Qin N, Yang H, Sun K, Hao J, Shu L, Liu J, Chen Q, Zhang P and Tao TH. *Nature Communications.* **2022**, 13, 79.

[33] Jin H, Kim Y, Youm W, Min Y, Seo S, Lim C, Hong C-H, Kwon S, Park G, Park S and Kim HJ. *npj Flexible Electronics.* **2022**, 6, 82.

[34] Qiao H, Sun S, Wu P. *Advanced Materials.* **2023**, 35, 2300593.

[35] Chun S, Son W, Kim H, Lim SK, Pang C and Choi C. *Nano Letters.* **2019**, 19, 3305.

[36] Tsuji S, Kohama T. *Sensors and Actuators A: Physical.* **2019**, 291, 7.

[37] Xu S, Xu Z, Li D, Cui T, Li X, Yang Y, Liu H and Ren T. *Polymers.* **2023**, 15, 2699

[38] Bai N, Xue Y, Chen S, Shi L, Shi J, Zhang Y, Hou X, Cheng Y, Huang K, Wang W, Zhang J, Liu Y and Guo CF. *Nature Communications.* **2023**, 14, 7121.

[39] Lecun Y, Bengio Y, Hinton G. *Nature.* **2015**, 521, 436.

[40] Soori M, Arezoo B, Dastres R. *Cognitive Robotics.* **2023**, 3, 54.

[41] Aggarwal K, Singh SK, Chopra M, Kumar S and Colace F. 2022, 1.

[42] Romero E, Sopena JM. *IEEE Transactions on Neural Networks.* **2008**, 19, 431.

[43] Khan S, Naseer M, Hayat M, Zamir SW, Khan FS and Shah M. *ACM Comput. Surv.* **2022**, 54, 200.

[44] Wang M, Yan Z, Wang T, Cai P, Gao S, Zeng Y, Wan C, Wang H, Pan L, Yu J, Pan S, He K, Lu J and Chen X. *Nature Electronics.* **2020**, 3, 563.

[45] Sun T, Tasnim F, Mcintosh RT, Amiri N, Solav D, Anbarani MT, Sadat D, Zhang L, Gu Y, Karami MA and Dagdeviren C. *Nature Biomedical Engineering.* **2020**, 4, 954.

[46] Zhou Z, Chen K, Li X, Zhang S, Wu Y, Zhou Y, Meng K, Sun C, He Q, Fan W, Fan E, Lin Z, Tan X, Deng W, Yang J and Chen J. *Nature Electronics.* **2020**, 3, 571.

[47] Shu S, Wang Z, Chen P, Zhong J, Tang W and Wang ZL. *Advanced Materials.* **2023**, 35, 2211385.

[48] Kireev D, Sel K, Ibrahim B, Kumar N, Akbari A, Jafari R and Akinwande D. *Nature Nanotechnology.* **2022**, 17, 864.

[49] Li G, Liu S, Wang L and Zhu R. *Science Robotics.* **2020**, 5, eabc8134.

[50] Nguyen T-D, Lee JS. *Sensors*. **2022**, 22, 50.

[51] Pyo S, Lee J, Bae K, Sim S and Kim J. *Advanced Materials.* **2021**, 33, 2005902.

[52] Gao S, Dai Y, Nathan A. *Advanced Intelligent Systems.* **2022**, 4, 2100074.

[53] Wang C, Liu C, Shang F, Niu S, Ke L, Zhang N, Ma B, Li R, Sun X and Zhang S. *Biosensors and Bioelectronics.* **2023**, 220, 114882.

[54] Eberman LE, Finn ME. *Athletic Training Education Journal.* **2010**, 5, 170.

[55] Elder AT, Mcmanus IC, Patrick A, Nair K, Vaughan L and Dacre J. *Clin Med (Lond).* **2017**, 17, 490.

[56] Rehnke RD, Groening RM, Van Buskirk ER and Clarke JM. *Plastic and Reconstructive Surgery.* **2018**, 142,

[57] Jütte J, Hohoff A, Sauerland C, Wiechmann D and Stamm T. *BMC Pregnancy and Childbirth.* **2014**, 14, 124.

[58] Ozioko O, Dahiya R. *Advanced Intelligent Systems.* **2022**, 4, 2100091.

[59] Sundaram S, Kellnhofer P, Li Y, Zhu J-Y, Torralba A and Matusik W. *Nature.* **2019**, 569, 698.

[60] Cui Z, Wang W, Xia H, Wang C, Tu J, Ji S, Tan JMR, Liu Z, Zhang F, Li W, Lv Z, Li Z, Guo W, Koh NY, Ng KB, Feng X, Zheng Y and Chen X. *Advanced Materials.* **2022**, 34, 2207016.

[61] Chen L, Karilanova S, Chaki S, Wen C, Wang L, Winblad B, Zhang S-L, Özçelikkale A and Zhang Z-B. *Science.* **2024**, 384, 660.

[62] Gao Y, Ota H, Schaler EW, Chen K, Zhao A, Gao W, Fahad HM, Leng Y, Zheng A, Xiong F, Zhang C, Tai L-C, Zhao P, Fearing RS and Javey A. *Advanced Materials.* **2017**, 29, 1701985.

[63] Tashakori A, Jiang Z, Servati A, Soltanian S, Narayana H, Le K, Nakayama C, Yang C-L, Wang ZJ, Eng JJ and Servati P. *Nature Machine Intelligence.* **2024**, 6, 106.

[64] Sui M, Ouyang Y, Jin H, Chai Z, Wei C, Li J, Xu M, Li W, Wang L and Zhang S. *Nature Machine Intelligence.* **2023**, 5, 1149.

[65] Zhu M, Sun Z, Zhang Z, Shi Q, He T, Liu H, Chen T and Lee C. *Science Advances.* 2020, 6, eaaz8693.

Chapter 3

Experimental Methodology

This chapter outlines the experimental methodology employed in the development and analysis of tactile sensors. The rationale for selecting piezoelectric materials and pressure sensing technologies is detailed, highlighting the advantages in achieving high sensitivity and responsiveness in tactile applications. The construction of tactile sensors is elaborated, focusing on the integration of substrates, electrodes, and functional materials to optimize performance. Mechanical simulation techniques are utilized to model the sensor's behavior under various conditions, providing insights into its structural and functional properties. Data acquisition methods for multi-channel sensor arrays are discussed, emphasizing the importance of accurate and efficient data collection for real-time processing. Additionally, the chapter explores the use of SVM for classification tasks, demonstrating how SVMs can effectively differentiate between various tactile stimuli, thereby enhancing the sensor's ability to provide precise and reliable feedback. This comprehensive methodology sets the foundation for the development of advanced tactile sensing systems.

3.1 Rationale for mechanisms and materials selection

Piezoelectric materials are chosen for their ability to convert mechanical stress into electrical signals rapidly[1, 2]. This fast response is crucial for applications requiring real-time data acquisition and processing, such as dynamic force sensing and texture discrimination. The instantaneous generation of electrical signals upon deformation allows for precise detection and measurement of mechanical changes (vibration, bending, pressure, and strain), making them ideal for tactile sensors.

Polyvinylidene fluoride (PVDF) is selected for its flexibility, which is important in applications where the sensor needs to conform to complex surfaces or move without damaging the material[3-5]. Additionally, PVDF is compatible with the deposition of gold electrodes, which can be easily fabricated through processes like thermal evaporation or sputtering. The combination of PVDF and gold electrodes provides a robust and reliable system for capturing piezoelectric signals, while the flexibility of PVDF enhances the durability and versatility of the sensor.

Piezoresistive films are chosen for their straightforward processing and integration capabilities. These films change their electrical resistance in response to applied pressure, making them effective for measuring static and quasi-static forces. The simplicity of processing, such as printing or coating techniques, allows for easy fabrication and integration into various substrates and devices[6, 7]. This ease of processing also supports scalable manufacturing, making it practical for producing pressure-sensitive components.

A pressure sensing array is implemented to provide spatial resolution and detect pressure distribution across a surface. This array can measure variations in pressure at different points, enabling detailed mapping of pressure profiles and tactile information[8, 9]. The use of a pressure sensing array enhances the ability to capture complex interactions with surfaces, which is essential for applications in robotics, medical diagnostics, and tactile interfaces. The array configuration allows for comprehensive data collection, improving the accuracy and effectiveness of the sensing system.

Support Vector Machines (SVM) were chosen for the classification task due to their effectiveness in high-dimensional spaces and their ability to handle both linear and non-linear data through the use of kernel functions[10]. SVMs are particularly well-suited for situations where the number of features is greater than the number of samples, as they focus on maximizing the margin between classes, which often leads to better generalization on unseen data. Additionally, SVMs are less prone to overfitting, especially in cases with limited training data, due to their emphasis on the most informative data points, known as support vectors. In contrast, neural networks, while powerful, often require large amounts of data and extensive tuning of hyperparameters, such as learning rates and network architecture, to perform well. They can also be computationally intensive and time-consuming to train, which might not be feasible in scenarios with limited resources[11].

3.2 Constructions of tactile sensors

Tactile sensing systems are designed to mimic the human sense of touch, enabling machines and devices to perceive and interact with their environment through tactile feedback. The construction of these systems involves a careful selection of substrates, electrodes, and functional materials, each playing a crucial role in the sensor's performance, which were reviewed in Figure 3.1. Substrates provide the foundational structure, ranging from rigid inorganic materials to flexible organic options, influencing the sensor's durability and adaptability. Electrodes, which can be metal, semiconductor, or gel-based, are essential for transmitting electrical signals corresponding to tactile stimuli. Functional materials, such as piezoresistive, capacitive, and piezoelectric layers, are critical in converting mechanical stimuli into measurable electrical signals[12]. Together, these components create sophisticated tactile sensors capable of high sensitivity, resolution, and reliability, enabling applications in fields like robotics, healthcare, and consumer electronics.

The construction of tactile sensors involves using various substrates, including inorganic materials, hard organic materials, and soft organic materials. Garner et al. introduced ultra-

slim flexible glass substrates (⩽200 μm thick), which are ideal for high-quality and long-lasting displays (Figure 3.1a)[13]. Qiu et al. developed a bimodal tactile sensor that captures multidimensional static and dynamic stimuli, quantifying both softness and texture features. This sensor enables robotic manipulators to identify delicate objects with high accuracy and stability (Figure 3.1b)[14]. Tan et al. designed a soft tactile sensor using a sinusoidally magnetized flexible film, which allows for precise measurement of normal and shear forces. This design enhances robots' abilities to handle fragile objects and perform complex tasks (Figure 3.1c)[15].

The electrodes used in tactile sensors include metal, semiconductor, and gel types[16]. Peng et al. reported a breathable, biodegradable, and antibacterial e-skin based on all-nanofiber triboelectric nanogenerators, utilizing silver nanowire (Ag NW) between polylactic-co-glycolic acid (PLGA) and polyvinyl alcohol (PVA). This e-skin offers high sensitivity and is suitable for real-time physiological monitoring (Figure 3.1d)[17]. Yang et al. developed an air-permeable and washable triboelectric nanogenerator using multiwalled carbon nanotube-coated air-laid paper electrodes, which are flexible, durable, and comfortable for wearable applications (Figure 3.1e)[18]. Another study by Yang et al. introduced a triboelectric nanogenerator with PVA/PA hydrogel for self-powered human-machine interface sensing, featuring excellent mechanical and electrical properties (Figure 3.1f)[19].

The functional materials in tactile sensors often include piezoresistive, capacitive, and piezoelectric/triboelectric layers[20]. Tan et al. created a stretchable strain sensor with superior thermal management capabilities, combining high stretchability, sensitivity, and thermal conductivity (Figure 3.1g)[21]. Ge et al. developed bifunctional electronic skins with a compliant magnetic microelectromechanical system, capable of distinguishing tactile and touchless interactions (Figure 3.1h)[22]. Kim et al. utilized a kirigami design with PVDF film to fabricate a stretchable strain sensor, optimizing its performance through finite element analysis (Figure 3.1i)[23].

The future design of tactile sensors should focus on enhancing multifunctionality, sensitivity, and durability. Advancements in substrate materials, such as flexible and

biodegradable options, will support the development of eco-friendly and wearable tactile systems. Innovations in electrode materials, particularly those offering breathability and flexibility, will further enhance the user comfort and functionality of these devices. The integration of advanced functional materials, like piezoelectric and triboelectric layers, will allow for more accurate and diverse sensory feedback[24]. Additionally, optimizing the design through computational methods, such as finite element analysis, will ensure that sensors are not only well performing but also customizable for specific applications[25, 26]. The development of tactile sensors will continue to benefit fields such as robotics, healthcare, and wearable technology, providing more nuanced and reliable sensory interactions.

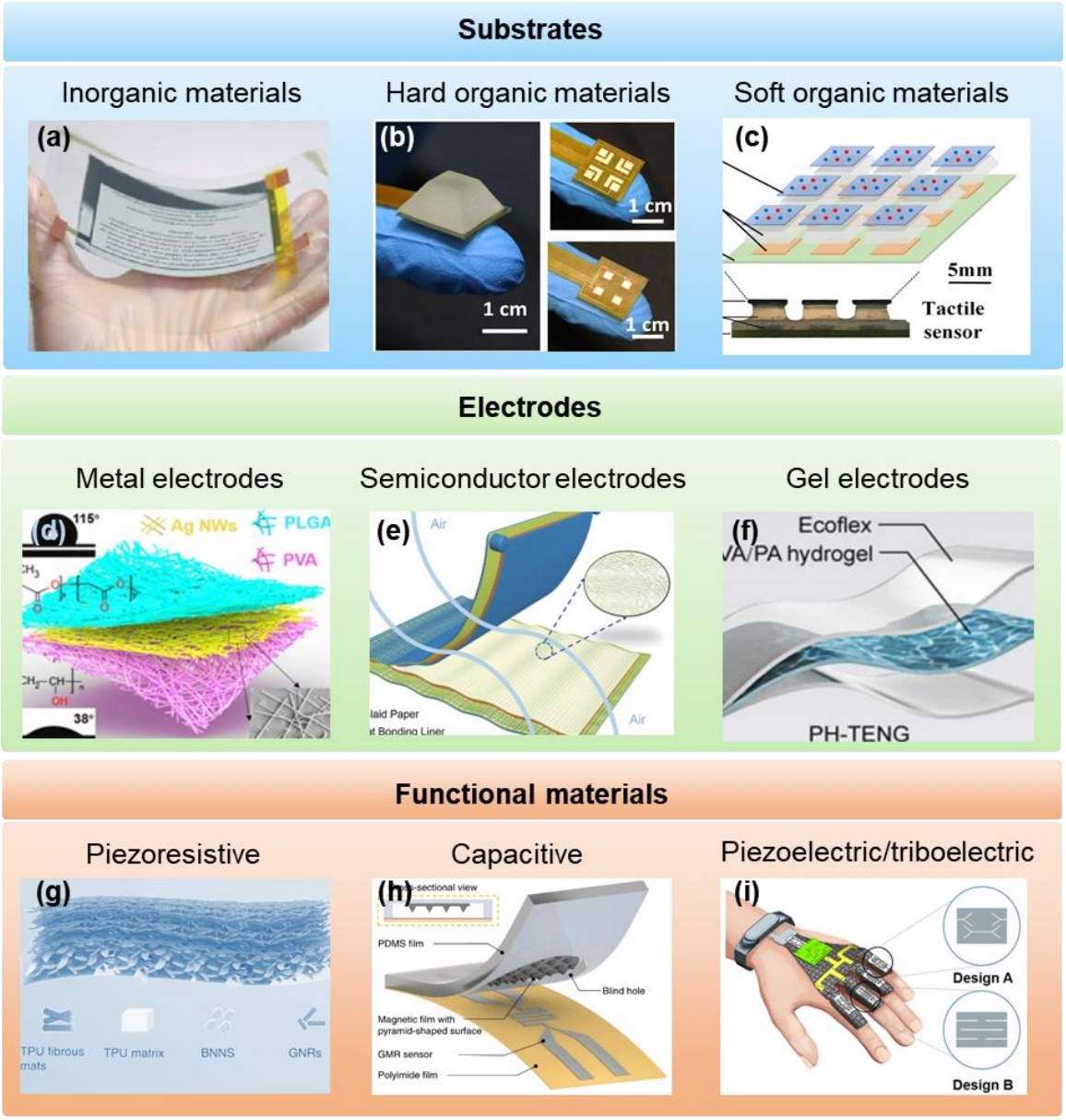

Figure 3.1 Common construction of tactile sensors. Substates. (a) Ultra-slim glass substrates. Reproduced with permission from ref.[13]. Copyright 2012 John Wiley and Sons. (b) PET/PI substrates. Reproduced with permission from ref.[14]. Copyright 2020 Elsevier. (c) PDMS substrates. Electrodes. Reproduced with permission from ref.[15]. Copyright 2021 American Association for the Advancement of Science (d)Ag nanowires. Reproduced with permission from ref.[17]. Copyright 2020 American Association for the Advancement of Science (e) MWCNTs. Reproduced with permission from ref.[18]. Copyright 2018 Wiley. (f) Hydrogel. Functional materials. Reproduced with permission from ref.[19]. Copyright 2022 Elsevier. (g) Piezoresistive layer. Reproduced with

permission from ref.[21]. Copyright 2020 Springer Nature. (h) capacitive layer. Reproduced with permission from ref.[22]. Copyright 2019 Springer Nature. (i) Piezoelectric/triboelectric layer. Reproduced with permission from ref.[23]. Copyright 2022 Springer Nature.

3.3 Mechanical simulation

Understanding the piezoelectric properties of materials through mechanical simulations is crucial for optimizing the design and functionality of devices that rely on these properties. Piezoelectric materials, which generate an electric charge in response to mechanical stress, are used in a wide range of applications including sensors, actuators, and energy harvesters. Mechanical simulations allow for the detailed analysis of how these materials behave under different conditions, such as varying stress or electric fields. By simulating piezoelectric properties, engineers and researchers can predict the performance of these materials, identify potential issues, and design devices that maximize efficiency and reliability. The cantilever beam structure is a prevalent design for piezoelectric devices because its simple configuration effectively leverages the piezoelectric effect to convert mechanical stress into electrical signals, making it ideal for applications requiring precise force or vibration sensing.

To simulate a piezoelectric cantilever beam using COMSOL Multiphysics, start by establishing a detailed finite element model (as shown in Figure 3.2a). Begin by defining the geometry of the cantilever beam using COMSOL's geometry tools, either in 2D or 3D based on your design requirements. Accurately specify the beam's dimensions to reflect the actual physical characteristics[27]. Assign material properties to the beam by selecting a suitable piezoelectric material from COMSOL's library or by defining custom properties. These properties should include piezoelectric constants, Young's modulus, and density, which are crucial for accurately modeling the piezoelectric behavior.

In the physics setup, use the Piezoelectric Devices physics interface to couple the mechanical and electrical fields. This interface is essential because the piezoelectric effect

involves an interaction between mechanical deformation and electrical fields. Configure boundary conditions appropriately: for a cantilever beam, fix one end to simulate the anchored side while leaving the other end free. If the simulation involves electrodes, define their positions and apply the necessary electrical potentials[28]. This setup allows the simulation to accurately represent how electrical and mechanical effects interact in the beam. Then, define the frequency range of interest to capture the resonance characteristics of the cantilever beam (Figure 3.2b). Run the simulation to compute the natural frequencies and mode shapes, which reveal the beam's resonant behavior and performance.

After running the simulation, utilize COMSOL's post-processing tools to visualize and interpret the results. Plot the deformation of the beam, the distribution of electric fields, and the resonance modes to gain insights into the beam's behavior. Extract critical data such as resonance frequencies, voltage outputs, and mechanical strain, which are valuable for evaluating the performance and optimizing the design of the piezoelectric cantilever beam. This comprehensive approach allows for a detailed understanding of the beam's mechanical and electrical interactions, supporting effective design and application.

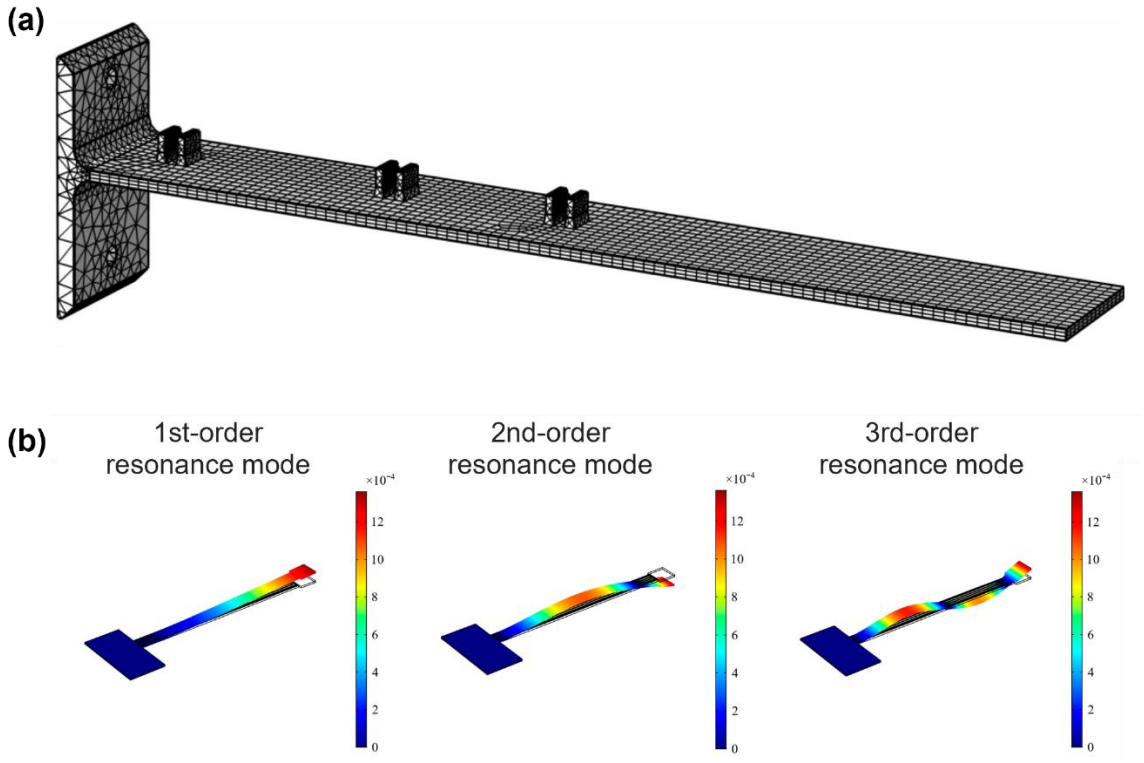

Figure 3.2 Simulation results of cantilever beam using COMSOL Multiphysics simulation. (a) Finite element model of piezoelectric cantilever beam. Reproduced with permission from ref.[29]. Copyright 2024 Elsevier. (b) The eigenfrequency of the 1st, 2nd, and 3rd-order resonance mode with COMSOL Multiphysics simulation. Reproduced with permission from ref.[30]. Copyright 2021 Wiley.

3.4 Data acquisition of multi-channel sensor arrays

Artificial tactile sensors are designed to replicate some fundamental functions of the biological tactile system, such as texture detection, shape discrimination, and assessing the force required for a correct grasp. These sensors find extensive applications in robotics, ergonomics, and rehabilitation, where the task often involves measuring the normal components of force with sufficient spatial resolution. Various types of sensors, including resistive, capacitive, strain gauge, and others, have been proposed for these tasks. Among them, piezoresistive sensors (PRS), also known as Force Sensing Resistors (FSR), are particularly popular. PRS sensors can be easily fabricated as discrete sensors or as arrays with millimeter-level resolution[31, 32]. These sensors operate based on a conductive polymer placed between a film conductive grid. When the sensor is pressed, the resistance of the polymer-grid changes, and an electronic circuit measures the voltage drop across (or the current through) this resistance. With appropriate calibration, the applied force can be determined.

Despite their widespread use, PRS sensors have some limitations due to their transduction mechanism, including issues like non-linearity, hysteresis, and creep. These challenges have been widely discussed in the literature. Furthermore, when using sensor arrays, additional factors such as crosstalk between adjacent elements must be considered. Crosstalk occurs due to parasitic parallel paths that can alter the resistance reading when attempting to measure the voltage corresponding to a taxel (tactile pixel)[33]. While some circuits have been proposed to mitigate this issue, they are often presented in a very schematic manner without thoroughly examining the errors introduced by the electronics.

Moreover, a comprehensive comparative evaluation of the performance of these various circuits is still lacking.

When attempting to read the value of a resistor Rij in a piezoresistive sensor array, parasitic paths of varying lengths and resistances can interfere, causing errors in the voltage reading and, consequently, the measurement of the force acting on Rij (shown in Figure 3.3). For example, a parasitic path composed of the resistances Rim, Rsm, and Rsj in series can appear in parallel with Rij. This interference can distort the sensor's output. In the case of sensors constructed from a single polymer sheet, additional parasitic paths can arise due to the bulk conductivity of the sheet. These are represented by the parasitic resistances Ris=Rrr and Rjm=Rcc, which correspond to row–row and column–column couplings, respectively. These parasitic effects can significantly impact the accuracy of the readings and need to be carefully considered in the design and analysis of sensor arrays.

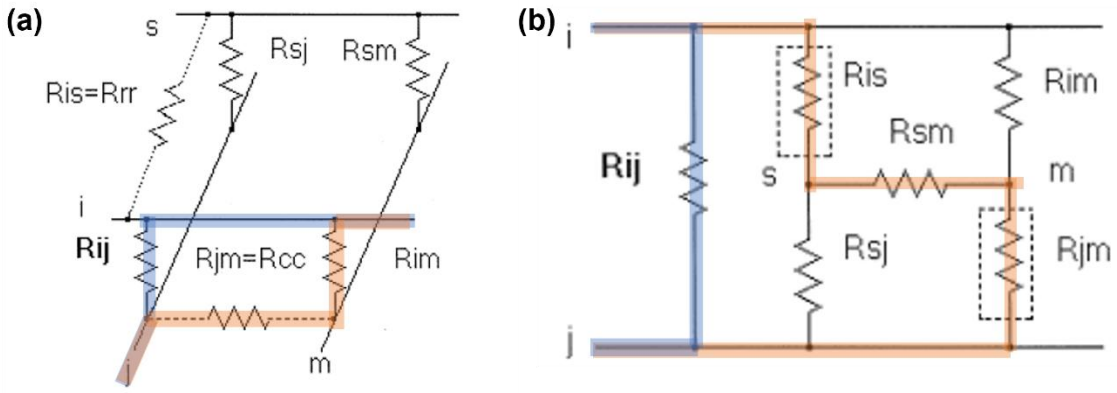

Figure 3.3 Schematic diagrams of matrix with parasitic path. (a) Crossover circuits, and (b) equivalent circuits. The blue path is the intended path, and the orange path is the parasitic path. Reproduced with permission from ref.[34]. Copyright 1999 Elsevier.

The proposed circuits for scanning piezoresistive arrays can be categorized into two main types: those that counteract crosstalk using a feedback loop[35, 36] and those that employ grounding (Figure 3.4)[37, 38]. In Circuit A, multiplexers (mux1 and mux3) connect the resistor Rij in a partition circuit comprising Vcc, Rp, Rmux1 (the on-resistance of mux1), Rij, buffer i, and mux3, with the output voltage Vout being read through mux2 and buffer 1. Crosstalk effects are mitigated by the feedback loop formed by the buffers on the rows

and the switches on the columns. The buffers apply the output voltage to all rows except row i, while the switches connect the non-active columns to Vout, ensuring that all the terminals of the array's resistors, other than Rij, are at the same potential, ideally preventing any current from flowing through them.

Another circuit that uses feedback, outlined in previous studies, inserts buffers on both the inactive rows and columns. A slightly modified version of this circuit, referred to as Circuit B, incorporates both the double multiplexer feature (which compensates for the switch resistance, as in Circuit A) and buffers on both rows and columns. This configuration enhances performance compared to the previous circuits, albeit at the cost of increased electronic complexity.

Circuit C utilizes amplifiers for reading and eliminates crosstalk by inserting a buffer on every column and a trans-resistance amplifier on every row. This setup imposes a near-zero potential difference across the non-active elements, effectively countering the influence of parasitic paths and the resistances *R*rr and *R*cc. This method ensures more accurate readings by minimizing the interference from unwanted electrical paths in the piezoresistive array.

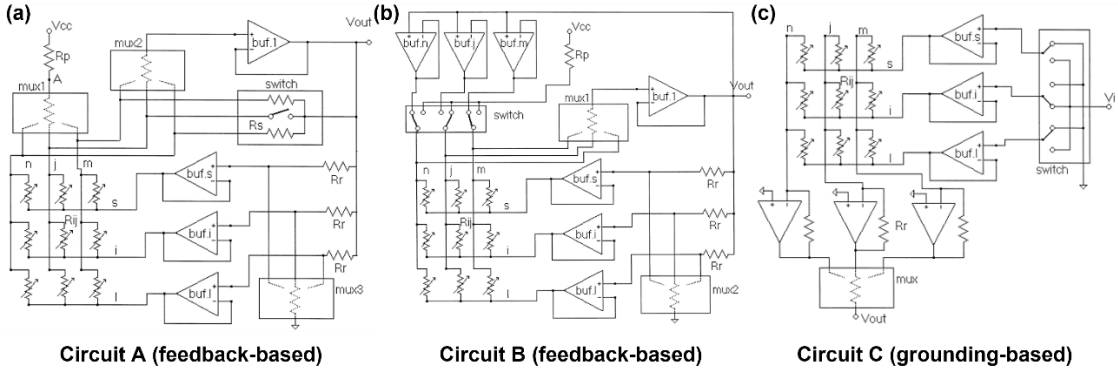

Figure 3.4 Schematic diagrams of reading circuit designs for countering parasitic resistance. (a) Circuit A with feedback design. Buffers and a switch are used to apply the output voltage to the rows and columns, respectively, to counteract crosstalk and the effects of row-row and column-column couplings (Rrr and Rcc). (b) Circuit B with feedback design. Each row is powered by a constant voltage source through independent buffers. (c) Circuit C with grounding design. This circuit is similar to Circuit A, but it counteracts

crosstalk by inserting buffers on both the rows and columns. Reproduced with permission from ref.[34]. Copyright 1999 Elsevier.

3.5 Support Vector Machine (SVM) for classification task

SVMs are highly efficient for handling high-dimensional, heterogeneous, and sparsely labeled datasets, making them versatile for various applications[39-41]. As a maximum margin classifier, the SVM decision function is defined by a hyperplane that maximally separates samples from different classes[42]. The typical process for utilizing SVM involves several steps: first, normalizing the sample data; second, applying a kernel function to map the samples, with commonly used kernels being the Radial Basis Function (RBF) and linear kernels. Linear kernels are particularly effective for linearly separable data; third, optimizing the hyperparameters using cross-validation and grid search; fourth, training the model with the optimal parameters; and finally, testing the model. Figure 3.1d illustrates a conceptual representation of Support Vector Machines (SVM). In Figure 3.5, multidimensional data is mapped into a two-dimensional space, where a line, or decision boundary, is drawn to fully separate data points belonging to different classes.

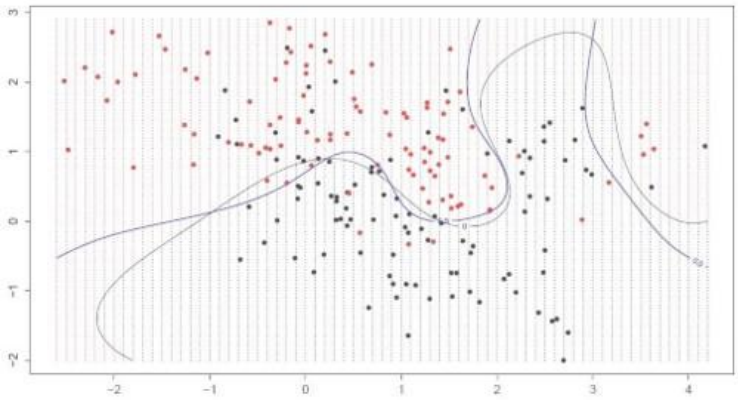

Figure 3.5 A schematic diagram of 2D classification by SVM. Finding a line can completely separate all input points.

The standard formulation of SVM defines it as a maximum margin classifier, meaning it is a classifier whose decision function is a hyperplane that maximally separates samples from

different classes. Notationally, given a labeled training data set, and given a nonlinear mapping $\phi(\cdot)$, the SVM method solves the following optimization problem[43]:

$$min\frac{1}{2}\|\mathrm{w}\|^2 + C\sum_{i=1}^{m}\xi\mathrm{i}$$

subject to the constraints:

$$y_i(\omega^T\phi(x_i)+b) \geq 1-\xi\mathrm{i} \qquad \text{for i} = 1, 2, \ldots, \mathrm{m}$$
$$\xi_i > 0 \qquad \text{for i} = 1, 2, \ldots, \mathrm{m}$$

where w and b define a linear classifier in $\mathbb{R}^N$ since xi are in $\mathbb{R}^N$, and ξ_i are positive slack variables that allow for handling permissible errors. The minimization functional includes two terms with distinct meanings: the first term, $\frac{1}{2}\|\omega\|^2$, aims to minimize the norm of the model weights, which is equivalent to maximizing the margin (the separation between classes). The second term, $C\sum_{i=1}^{m}\xi_i$, seeks to minimize the errors committed during classification. One could simply maximize the margin without considering the committed errors, leading to the concept of a maximum margin SVM. However, by incorporating the slack variablesξ_i, the problem is relaxed, resulting in what is known as the soft-margin SVM. This version of SVM strikes a balance between minimizing training errors and maximizing the margin, providing a more flexible and robust classification approach.

The SVM algorithm has several advantages: it can be used for classification (both binary and multi-class), regression, and outlier detection. It also exhibits strong robustness and generalization ability for unknown data, particularly when the dataset is small, where it often outperforms other traditional machine learning algorithms.

References

[1] Tressler JF, Alkoy S, Newnham RE. *Journal of Electroceramics.* **1998**, 2, 257.

[2] Kim HS, Kim J-H, Kim J. *International Journal of Precision Engineering and Manufacturing.* **2011**, 12, 1129.

[3] Pan M, Yuan C, Liang X, Zou J, Zhang Y and Bowen C. *iScience.* **2020**, 23,

[4] Feng Z, Zhao Z, Liu Y, Liu Y, Cao X, Yu D-G and Wang K. *Advanced Materials Technologies.* **2023**, 8, 2300021.

[5] Qiu X, Bian Y, Mei X, Luo X, Hu Z, Xuan F-Z, Xiang Y and Zhu G. *Advanced Materials Technologies.* **2024**, 9, 2301494.

[6] Fiorillo AS, Critello CD, Pullano SA. *Sensors and Actuators A: Physical.* **2018**, 281, 156.

[7] Park S-J, Kim J, Chu M and Khine M. *Advanced Materials Technologies.* **2018**, 3, 1700158.

[8] Sundaram S, Kellnhofer P, Li Y, Zhu J-Y, Torralba A and Matusik W. *Nature.* **2019**, 569, 698.

[9] Chen L, Karilanova S, Chaki S, Wen C, Wang L, Winblad B, Zhang S-L, Özçelikkale A and Zhang Z-B. *Science.* **2024**, 384, 660.

[10] Mustafa Abdullah D, Mohsin Abdulazeez A. *Qubahan Academic Journal.* **2021**, 1, 81.

[11] Mahesh B. *International Journal of Science and Research (IJSR)..* **2020**, 9, 381.

[12] Li H, Ma Y, Huang Y. *Materials Horizons.* **2021**, 8, 383.

[13] Garner S, Merz G, Glaesemann GS, Tosch J, Chang C, Marshall D, Li X, Tian L, Vasilakos K and Gagov A. *SID Symposium Digest of Technical Papers.* **2012**, 43, 342.

[14] Qiu Y, Wang F, Zhang Z, Shi K, Song Y, Lu J, Xu M, Qian M, Zhang W, Wu J, Zhang Z, Chai H, Liu A, Jiang H and Wu H. *Science Advances.* **2024,** 10, eadp0348.

[15] Yan Y, Hu Z, Yang Z, Yuan W, Song C, Pan J and Shen Y. *Science Robotics.* **2021**, 6, eabc8801.

[16] Li Y, Shi L, Cheng Y, Wang R and Sun J. *Chemical Engineering Journal.* **2023**, 455, 140763.

[17] Peng X, Dong K, Ye C, Jiang Y, Zhai S, Cheng R, Liu D, Gao X, Wang J and Wang ZL. *Science Advances.* **2020**, 6, eaba9624.

[18] Yang W, Cao R, Zhang X, Li H and Li C. *Advanced Materials Technologies.* **2018**, 3, 1800178.

[19] Yang J, An J, Sun Y, Zhang J, Zu L, Li H, Jiang T, Chen B and Wang ZL. *Nano Energy.* **2022**, 97, 107199.

[20] Li W-D, Ke K, Jia J, Pu J-H, Zhao X, Bao R-Y, Liu Z-Y, Bai L, Zhang K, Yang M-B and Yang W. *Small.* **2022**, 18, 2103734.

[21] Tan C, Dong Z, Li Y, Zhao H, Huang X, Zhou Z, Jiang J-W, Long Y-Z, Jiang P, Zhang T-Y and Sun B. *Nature Communications.* **2020**, 11, 3530.

[22] Ge J, Wang X, Drack M, Volkov O, Liang M, Cañón Bermúdez GS, Illing R, Wang C, Zhou S, Fassbender J, Kaltenbrunner M and Makarov D. *Nature Communications.* **2019**, 10, 4405.

[23] Kim Y-G, Song J-H, Hong S and Ahn S-H. *npj Flexible Electronics.* **2022**, 6, 52.

[24] Pyo S, Lee J, Bae K, Sim S and Kim J. *Advanced Materials.* **2021**, 33, 2005902.

[25] Yang W, Qin Y, Wang Z, Yu T and Ge Z. *Journal of Electronic Materials.* **2022**, 51, 6735.

[26] Pierre Claver U, Zhao G. *Advanced Engineering Materials.* **2021**, 23, 2001187.

[27] Ly R, Rguiti M, D'astorg S, Hajjaji A, Courtois C and Leriche A. *Sensors and Actuators A: Physical.* **2011**, 168, 95.

[28] Bhuvana S, Prathiksha H, Sindhu V and Vasudha H. *ICSCA.* **2018**, 1.

[29] Du S, Zhou J, Li F. *Measurement.* **2024**, 227, 114305.

[30] Liu Z, Chen J, Zou X. *Sensors.* **2021**, 21, 87

[31] Dario P, Rossi DD. *IEEE Spectrum.* **1985**, 22, 46.

[32] Xu S, Xu Z, Li D, Cui T, Li X, Yang Y, Liu H and Ren T. *Polymers.* **2023**, 15, 2699.

[33] Wang S, Maillet YY, Wang F, Lai R, Luo F and Boroyevich D. *IEEE Transactions on Industrial Electronics.* **2010**, 57, 3050.

[34] D'alessio T. *Sensors and Actuators A: Physical.* **1999**, 72, 71.

[35] Speeter TH. *The International Journal of Robotics Research.* **1990**, 9, 25-36.

[36] Tise B. *IEEE International Conference on Robotics and Automation.* **1988**;760-64 vol.2.

[37] Lazzarini R, Magni R, Dario P. *IEEE/RSJ International Conference on Intelligent Robots and Systems. Human Robot Interaction and Cooperative Robots.* **1995**, 4.

[38] Hillis WD. *The International Journal of Robotics Research.* **1982**, 1, 33.

[39] Veisi H. Learning with Fractional Orthogonal Kernel Classifiers in Support Vector Machines, **2023**, 3.

[40] Remeseiro B, Bolon-Canedo V. *Computers in Biology and Medicine.* **2019**, 112, 103375.

[41] Kecman V. *Support Vector Machines: Theory and Applications.* 2005;1-47.

[42] Dibike Yonas B, Velickov S, Solomatine D and Abbott Michael B. *Journal of Computing in Civil Engineering.* **2001**, 15, 208.

[43] Salcedo-Sanz S, Rojo-Álvarez JL, Martínez-Ramón M and Camps-Valls G. *WIREs Data Mining and Knowledge Discovery.* **2014**, 4, 234.

Chapter 4

A piezoelectric tactile sensor for in-situ measurement of micro-scale surface profile

Tactile perception is vital for detecting surface textures through touch, yet biological systems are limited to qualitative texture identification. This study introduces a piezoelectric tactile sensor with piezoelectric vibration sensors. The sensor converts surface vibrations into voltage signals, enabling quantitative analysis of texture features like grating width and depth. Unlike traditional systems, this piezoelectric tactile sensor provides detailed in-situ morphology characterization without the need for controlled speed or force. It can be integrated into robotic hands for real-time, three-dimensional texture reconstruction, advancing applications in soft robotics and human-machine interactions.

---

*This section was published substantially as:

Jiaqi Tu, Zheren Cai, Zhihua Liu, Jiangtao Su, Yanzhen Li, Xue Feng, Zequn Cui, Xiaodong Chen. Quantitative Tactile Sensing of Surface Microstructures Through Time-Domain Analysis of Piezoelectric Twin Signals. Advanced Materials e10393 (2025). DOI: 10.1002/adma.202510393. (Reprinted with permission from Wiley-VCH)

4.1 Introduction

Tactile perception plays an essential role in everyday life when we interact with the physical world. Multiple types of information are detected through touch and transmitted into our central nervous systems, generating the sense of touch[1]. As an essential part of tactile perception, texture perception extracts morphology, roughness, and hardness information during object manipulation. Fingertips can distinguish coarse and finer textures. The perception of coarse textures (with features of lateral dimensions more than about 200 μm) relies on spatial variations of the finger/substrate contact stress field and is mediated by the slowly adapting mechanoreceptors. To sense finer textures (<200 μm), fingers need to slide over surfaces where cutaneous vibrations are thus generated. These vibrations are intensively encoded, principally by Pacinian fibers[2]. Among the four embedding mechanoreceptors (slow-adapting receptors SA-I and -II and fast-adapting receptors FA-I and -II), the FA-I and -II contribute to dynamic force sensing (5-400 Hz) which is important for texture discrimination[3, 4]. However, the biological texture sensing is only a qualitative description of object features and shows low spatial resolution (0.94 mm on fingers), restricted by low receptor density (1 mm^2 on fingers) and a limited frequency response range[5-7]. Beyond biological sensing ability, artificial tactile sensory systems that can achieve quantitative morphology characterization will be of great use in emerging soft robotics, human–machine interactions, and tactile recreation.

To achieve the perception of dynamic force sensing for texture discrimination, tactile sensors based on piezoresistive[8-10], capacitive[11-13], triboelectric[14], and piezoelectric[15] mechanisms are commonly used to convert tactile information into electrical signals. Hysteresis of sensor responses limits the acquisition of morphology information. Therefore, flexible piezoelectric and triboelectric tactile sensors stand out with the advantage of fast response and low hysteresis for dynamic force. However, most of the current dynamic force sensing systems can only attain qualitative texture discrimination[15, 16]. They are trained through machine learning-based frequency feature extraction for distinguishing several objects with different roughness. Moreover, seldom research focused on wearability for texture perception under random sliding speed. Most roughness detection systems can only

achieve texture sensing under a fixed sliding system[17]. It remains a challenge to realize quantitative texture identification while testing without steady speed and force.

Herein, we present a piezoelectric tactile sensor consisting of two piezoelectric vibration sensors for quantitative morphology characterization. Two parallel polyethylene glycol terephthalate (PET) tips with fixed spacing are integrated into three-dimension (3D) printed structural materials. Flexible piezoelectric polyvinylidene difluoride (PVDF) films mount on the PET tips. PET tips will bend and recover while sliding the artificial fingertip over uneven surfaces. In the meantime, piezoelectric PVDF films on the tips transform vibrations into voltage signals. Two- tips design enables the identification of instantaneous speed. By correlating voltage signals with the actual moving condition and the calculated instantaneous speed, the time-domain information indicates the groove width, bar width, and groove depth of the grating texture. Therefore, the artificial fingertip can be worn on fingers and generates micro-scale morphology information. Three-dimensional (3D) morphology information can be obtained from multiple slides. The artificial fingertip was further integrated into a robotic hand. A 3D reconstruction of a fine micro-scale pattern was generated through a quick sweep in real-time.

4.2 Experimental methods

4.2.1 Deposition of gold electrodes on piezoelectric materials

First, a 100 μm PET sheet (transparency film, 3M) is laser-cut into masks using a PLS6.150D laser cutter (UNIVERSAL) with a 150W power output. These masks are then placed onto polarized PVDF films (28 μm, PolyK FlexQ Piezo PVDF). Following this, a thermal deposition process is carried out to laminate both sides of the PVDF films with electrodes (Figure 4.1). This process is performed using a thermal deposition system (Nano36, Kurt J Lesker), with the parameters set to deposit 5 nm of chromium (Cr) and 65 nm of gold (Au).

4.2.2 Fabrication of single piezoelectric tactile sensor

The polarized PVDF films with Cr/Au electrodes are securely adhered to a PET substrate layer using fast-drying glue (53573, Deili). The PET substrate layer is laser-cut into an arrow shape to precisely match the design specifications. Subsequently, another PET encapsulation layer, also fabricated by laser cutting, is adhered over the PVDF films on the PET substrate, as illustrated in Figure 4.1. Two copper wires are connected to the setup to enable the measurement of the piezoelectric voltage generated when the film is deformed.

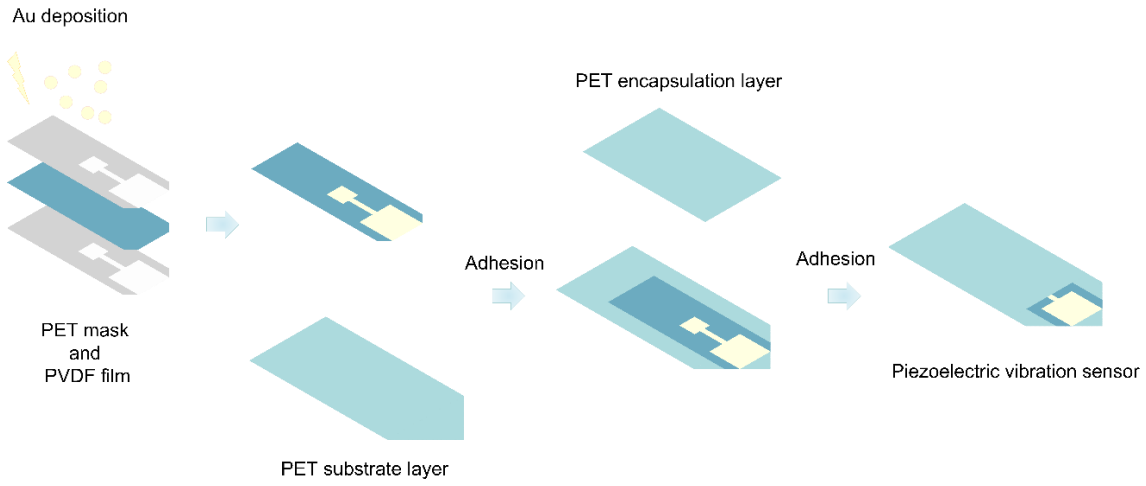

Figure 4.1 Fabrication processes of a single piezoelectric vibration sensor.

4.2.3 Fabrication for piezoresistive tactile sensors using 3D-printing

A 3D-printing structure was designed in Solidwork 2020 and then printed using Vero Clear (3D-printing materials) using a light-curing 3D printer (Stratasys, Objet260 Connex3). This 3D-printing structure has two grooves with a thickness of 0.35 mm and a spacing of 1.6 mm, so that two piezoelectric vibration sensors can be directly inserted into them. The construction of piezoelectric tactile sensor is shown in Figure 4.3a.

4.2.4 Fabrication of grating-structures for texture testing by photolithograph technology

SU-8 is commonly used negative photoresists in microfabrication, particularly for creating accurate microstructures with varying thicknesses. Therefore, SU-8 2007, 2030, 2075 (Kayaku) are elected to obtain rigid structures with different thickness and micro-patterns. The different serial numbers stand for the appropriate thickness. The lithographic process for fabricating SU-8 structures involves several key steps, which can be adjusted to achieve different thicknesses: 1. Cleaning: Clean the silicon wafer with acetone (C_3H_6O, Sigma-Aldrich) to remove any contaminants, which could affect the adhesion and quality of the SU-8 layer. 2. Spinning. Dispense SU-8 photoresist onto the substrate and spin at 500 rpm for 5-10 seconds with acceleration of 100 rpm/second, then spin at 2000 rpm for 30 seconds with acceleration of 300 rpm/second. 3. Soft baking. The recommended Soft Bake temperatures and times for the various SU-8 2000 products at selected film thicknesses. For examples, thickness of 3-5 nm requires 2 minutes of soft baking at 95°C and thickness of 26-40 nm requires 5 minutes of soft baking at 95°C. 4. Exposing. Align a photomask with the desired pattern over the substrate and expose the SU-8 to UV light for 10 seconds. 6. Post baking. Bake the exposed SU-8 layer on a hotplate to further cross-link the photoresist. The temperature and duration again depend on the thickness and specific SU-8 formulation. For examples, thickness of 3-5 nm requires 3 minutes of soft baking at 95°C and thickness of 26-40 nm requires 6 minutes of soft baking at 95°C. 7. Development. Immerse the substrate in a SU-8 developer solution for 2 min and followed by washing with acetone and ethanol. 8. Hard baking. Perform a final bake of 5 min under 200°C to further harden the SU-8 structures and enhance their mechanical properties.

4.2.5 Electrical characterization of piezoelectric tactile sensors and texture sensing systems

To set up the system, the two ends of the counter electrode of the piezoelectric vibration sensor are connected to the oscilloscope (MSO54, Tektronix) using copper wires. One end is connected to the positive terminal, and the other to the ground. This oscilloscope can

detect high-frequency voltage signals up to 500 MHz. For the piezoelectric tactile sensor, the two vibration sensors are connected to two separate channels on the oscilloscope, enabling dual-channel simultaneous detection. This setup allows for accurate, real-time quantitative texture sensing.

4.2.6 Calibration of 2D information testing by surface profiler

To operate the surface profiler (Alpha-Step D600) for measuring the thickness and 2D profile of grating structures on silicon wafers, start by calibrating the device for micrometer-scale resolution. Place the wafer on the stage and set the scanning speed to 0.2 mm/s. The stylus mode is set to up-and-down mode. The sweeping range is set to 3 mm. Perform thickness measurements by lowering the stylus onto the wafer's surface and recording the height profile. For 2D scanning, move the stylus across the wafer to capture detailed profile data. After the 2D information is generated, baseline smoothing is performed though machine’s software.

4.3 Results and discussion

4.3.1 Characterization of the electrical response of piezoelectric tactile sensors

The concept of vibration-induced quantitative texture sensing is inspired by the behavior of a cantilever beam. In this context, consider a rigid sheet acting as a cantilever beam with a piezoelectric layer attached. The rigid sheet is initially bent to a specific angle and then released, allowing it to vibrate freely until it comes to a stop, as illustrated in Figure 4.2a. The resulting changes in piezoelectric voltage over time manifest as a gradually decaying sine wave. Notably, the left side of the y-axis at the end of the cantilever beam also exhibits a gradually decaying sine wave over time. This synchronized trend indicates that the piezoelectric film on the cantilever beam can be used to quantitatively calibrate the beam's degree of deformation by measuring the instantaneous voltage. This phenomenon is crucial in the design of piezoelectric tactile sensor. Furthermore, it has been observed that the bending direction of the cantilever beam influences the polarity of the induced voltage,

with different bending directions producing distinct positive or negative voltages. Consequently, the direction of force deformation of the beam can be determined by analyzing the polarity of the induced voltages.

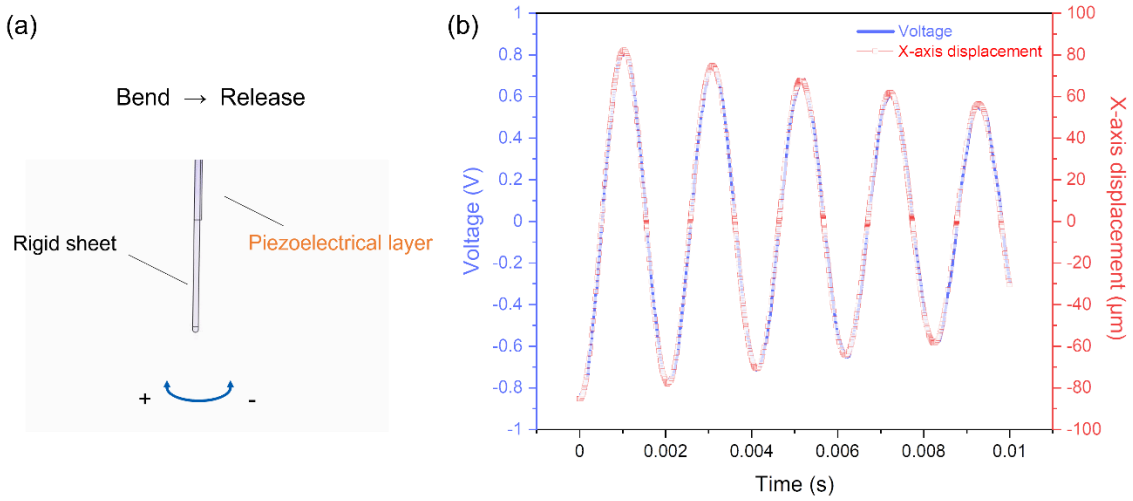

Figure 4.2 Principal support for vibration-induced quantitative texture sensing. (a) a schematic cantilever beams for force sensing. (b) Simulation results of vibration and generated voltage results.

The configuration of the piezoelectric tactile sensor is illustrated in Figure 4.3a. The system includes a single vibration sensor, which consists of a piezoelectric PVDF film with counter Au/Cr electrodes, adhered to 100 μm PET films. Two of these vibration sensors are embedded within a 3D-printed structure, spaced 1.6 mm apart. The overlapping area of the two counter electrodes at the piezoelectric tactile sensor tip measures 16 cm^2, as depicted in Figure 4.3b. The 3D-printed structure is designed with a 75-degree incline at the base, ensuring that the tips of the two piezoelectric vibration sensors make simultaneous contact with the testing surface. This configuration allows for precise vibration sensing and feedback. Additionally, these piezoelectric vibration sensors can be integrated into finger-like 3D-printed structural materials, as shown in Figure 4.3e, further enhancing the system's versatility and application potential.

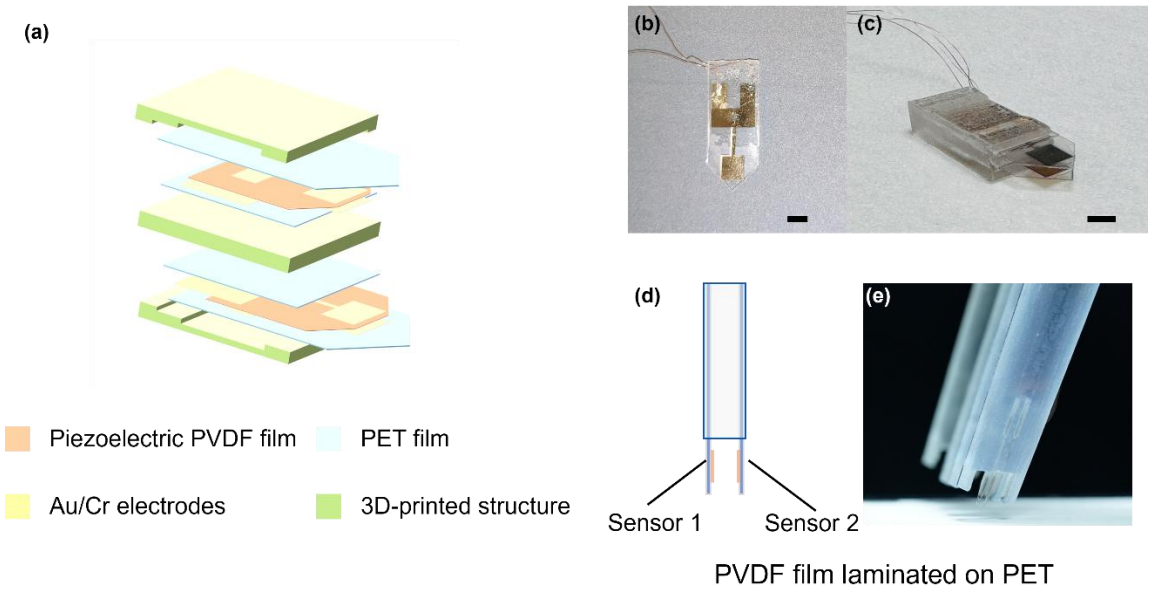

Figure 4.3 Configuration of the piezoelectric tactile sensor. (a) A schematic structure of piezoelectric tactile sensor. (b) Picture of top view of a single piezoelectric vibration sensor. The scale bar is 4 mm (c) Picture of side view of the piezoelectric tactile sensor. The scale bar is 4 mm (d) The second schematic structure of piezoelectric tactile sensor showing the parallel distribution of vibration sensors. (e) Picture of side of a 3D printed structural materials integrated with vibration sensors.

Photolithography was employed to fabricate grating textures using SU-8, a negative photoresist. The process involved varying the spinning speed to achieve different grating parameters. Three key parameters were controlled: width, distance, and thickness of the grating textures. To tune the thickness of the grating textures, different concentrations of SU-8 and spinning speeds were utilized. The width and distance of the grating lines were adjusted using various masking templates. The samples were designed to explore different configurations, including varying the width while keeping the distance constant, varying the distance with a constant width, and varying the thickness while maintaining the same distance and width. This systematic variation allowed for the creation of a diverse range of grating textures, enabling detailed analysis and optimization of the desired properties for quantitative texture sensing.

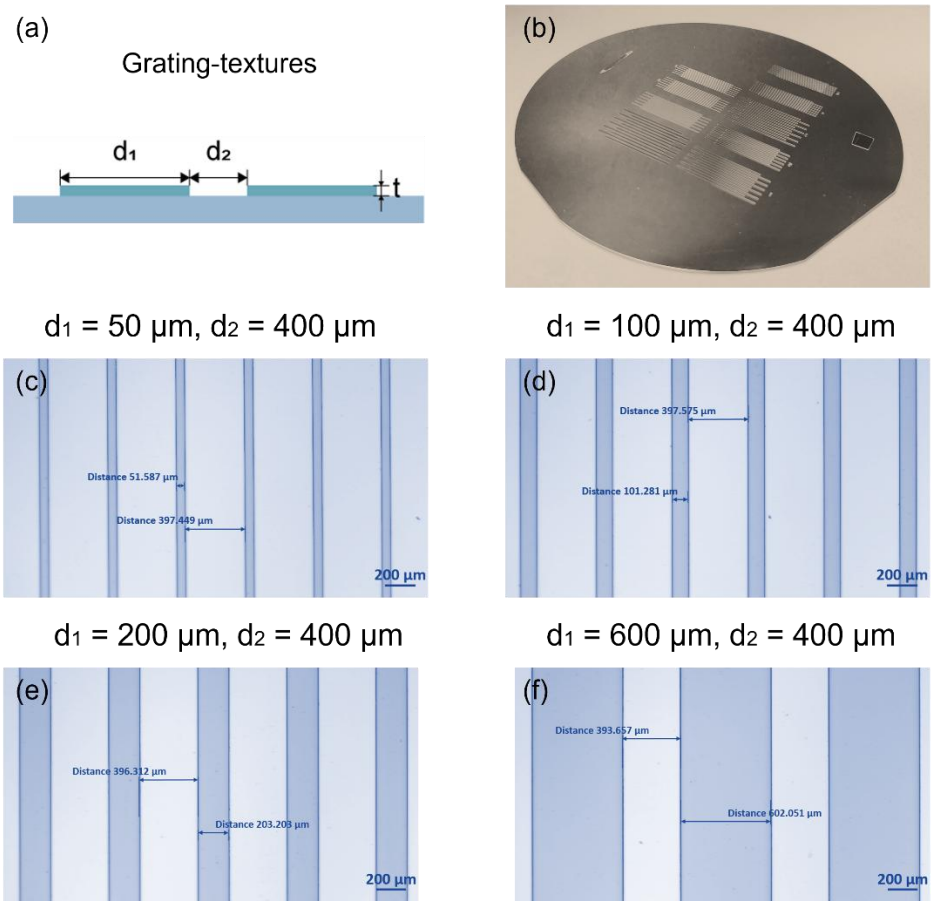

Figure 4.4 Grating textures based on photolithography. (a) Schematic side view image of grating-textures. t is thickness of the textures. d_1 is the width of the textures. d_2 is the distance of the textures. (b) Picture of side view of grating-textures on a silicon wafer. Optical images of different grating textures with different width and distance. (c) d_1 = 50 μm. d_2 = 400 μm. (d) d_1 = 100 μm. d_2 = 400 μm. (e) d_1 = 200 μm. d_2 = 400 μm. (f) d_1 = 600 μm. d_2 = 400 μm. The scale bar is 200 μm.

The primary mechanism for quantitative texture sensing in this system leverages the properties of piezoelectric materials, known for their fast and high-frequency response capabilities. Piezoelectric materials generate an instantaneous voltage when subjected to dynamic forces, making them ideal for dynamic force sensing applications, even though they may not be optimal for continuous monitoring. As the vibration sensor slides across a grating texture, the piezoelectric film generates a voltage peak. When the sensor moves away from the texture, an opposite voltage peak is produced. The time interval between these two peaks, along with the peak amplitude, is crucial for dynamic force sensing. This

setup allows for precise measurement and analysis of surface textures. An example of the voltage signals generated by one channel of the tactile sensor when gliding over a grating texture with dimensions d1 = 100 μm and d2 = 300 μm at a speed of 10 mm/s is shown in Figure 4.5b. A close-up view of these signals is provided in Figure 4.5c. For calibration purposes, the construction of a 3-axis moving platform is depicted in Figure 4.5d, facilitating accurate sensor calibration and ensuring reliable data acquisition.

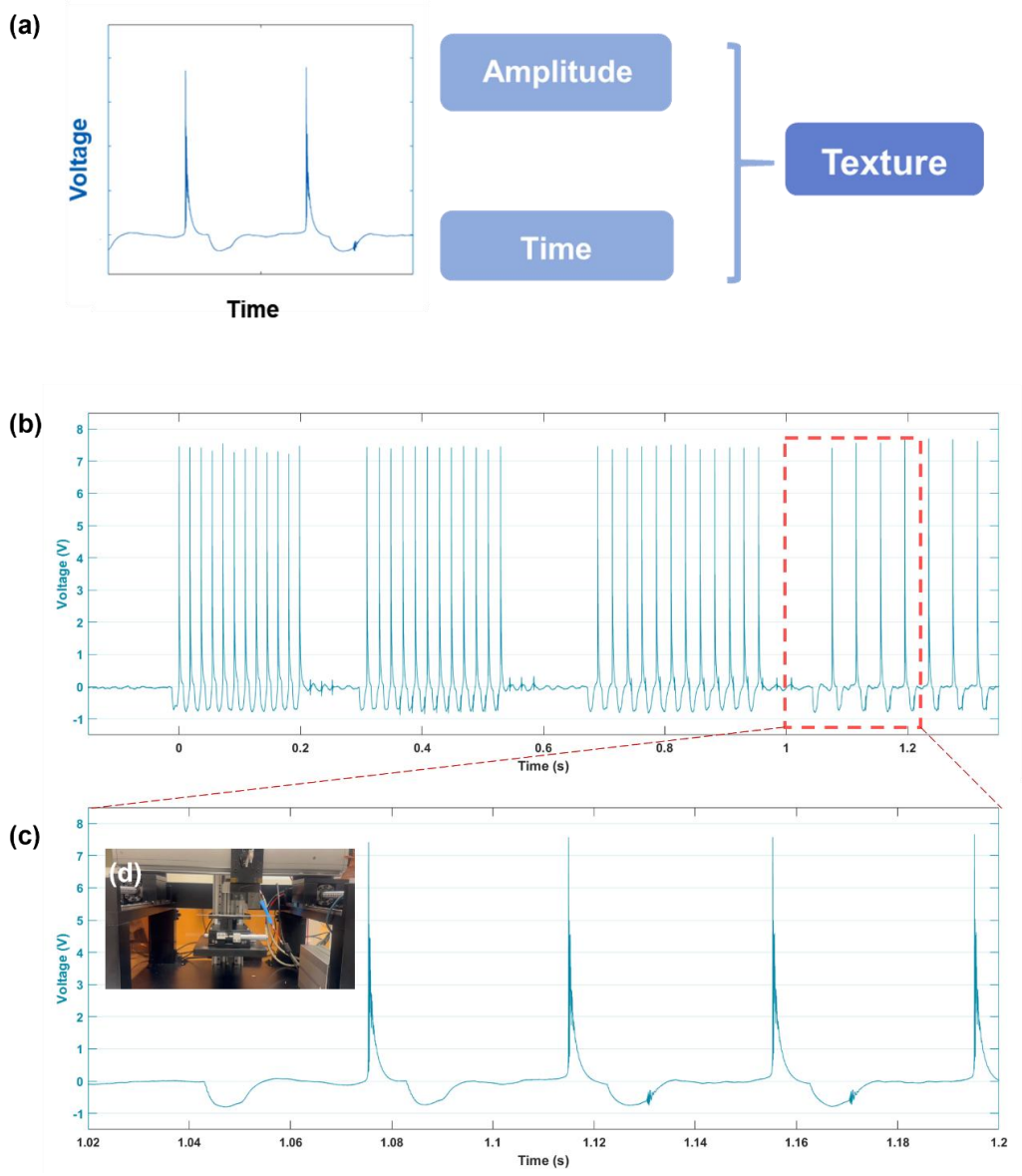

Figure 4.5 Response of the piezoelectric vibration sensor on piezoelectric tactile sensor. (a) Mechanism of dynamic force sensing. (b) Piezoelectric voltage signals while gliding over a grating-texture (d_1 = 600 μm. d_2 = 400 μm) under speed of 25 mm/s. (c) Zoom-in

figure of voltage signals. (d) Picture of a 3-axis moving platform.

A surface profiler (Alpha-Step D600) is used for dimensional calibration, providing height information at the micrometer scale. For example, the profiler measures the 2D information of grating structures on silicon wafers (d1 = 200 μm, d2 = 400 μm) at a speed of 0.2 mm/s (Figure 4.6). However, the scanning speed of the stylus profiler is limited, ranging from 0.01 to 0.4 mm/s, which makes it challenging to quickly acquire comprehensive 2D or 3D surface information. Additionally, at distances around 0.2 mm and 0.4 mm, the edge information collected by the surface profiler tends to be blurry, limiting its precision in these regions.

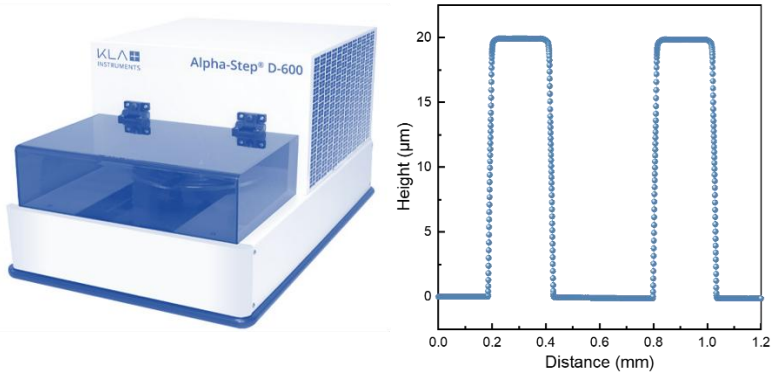

Figure 4.6 Thickness and 2D scanning of surface profiler (Alpha-Step D600). The 2D information of grating-structures on silicon wafers (d_1 = 200 μm. d_2 = 400 μm) under speed of 0.2 mm/s.

The mechanism of quantitative texture sensing involves analyzing the width and distance dimensions of surface textures. The corresponding movements of the vibration sensor and the resulting piezoelectric voltage signals are illustrated in Figure 4.7. A side view of the sensor's movement clearly delineates the stages of interaction between the sensor tip and the grating. State A represents the initial stage where the sensor tip is not in contact with the grating. As the sensor moves, the tip begins to deform upon contact, initiating at state B. By state C, the tip is fully in contact with the grating, and the deformation ceases. At this point, the piezoelectric voltage reaches its peak and begins to decline as the sensor continues to move. As the sensor approaches state E, the tip starts to lift off the grating. Upon complete separation at state F, there is a sudden deformation of the tip, leading to a

pronounced voltage peak known as Peak F. This peak is characterized by high amplitude due to the abrupt nature of the deformation. Additionally, the system exhibits a phenomenon of damped vibration, where the amplitude of the voltage signal gradually decreases over time. This attenuation is caused by factors such as friction, medium resistance, and other forms of energy dissipation within the vibration system. This detailed analysis of the sensor's movement and the resulting piezoelectric response provides valuable insights into the texture characteristics of the surface, allowing for precise quantitative texture sensing.

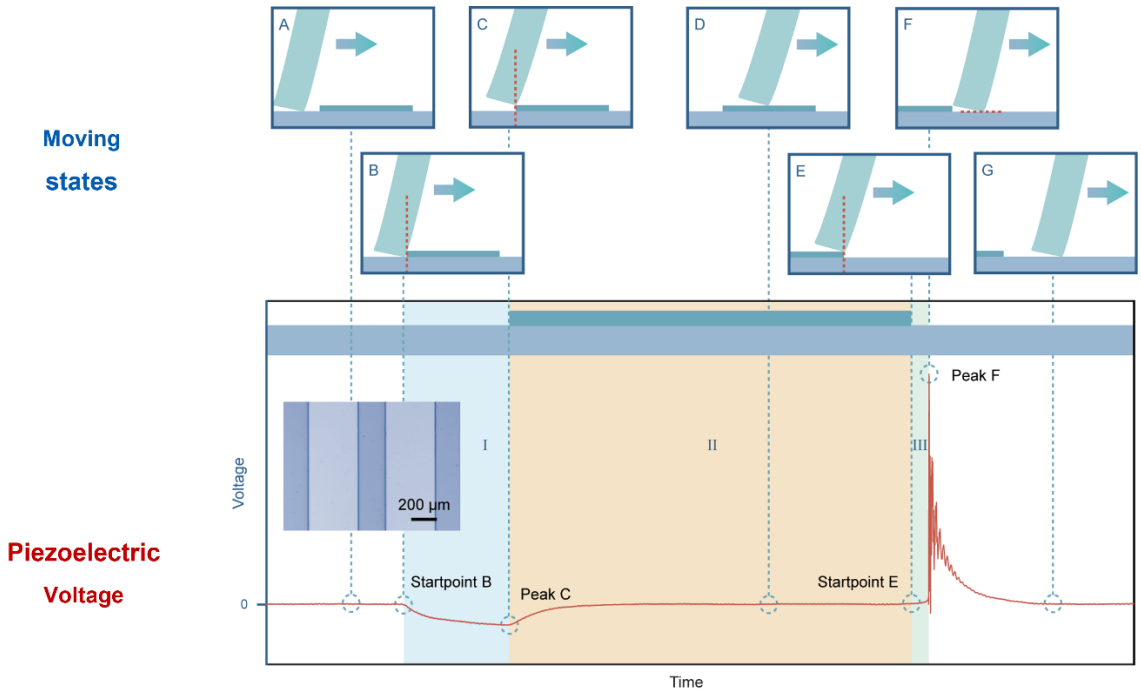

Figure 4.7 Mechanism of quantitative texture sensing on the dimension of width and distance. The inserted optical image shows the parameters of the tested grating-textures (d1 = 200 μm and d2 = 400 μm). The scale bar is 200 μm.

The piezoelectric tactile sensor was employed to detect an unknown grating texture. The piezoelectric voltage signals recorded while the sensor glided over this texture are presented in Figure 4.8a, with the sensor tip moving at a constant speed of 25 mm/s. From the voltage signals, the time intervals corresponding to the grating features were extracted: D_1F = 0.02391s and FD_2 = 0.01612s. Using these intervals, the dimensions of the grating were calculated as follows: the width (d_1) was determined to be 597.5 μm, and the distance

(d_2) between features was calculated as 403.0 μm. For comparison, the actual dimensions were measured to be d_1 = 602.051 μm and d_2 = 393.657 μm, yielding errors of only 0.75% and 2.5%, respectively. This high degree of accuracy demonstrates the piezoelectric tactile sensor's capability for quantitative texture sensing, allowing for precise distinction and measurement of width and distance in grating textures. The system's ability to accurately detect and quantify these parameters highlights its potential for detailed surface characterization in various applications.

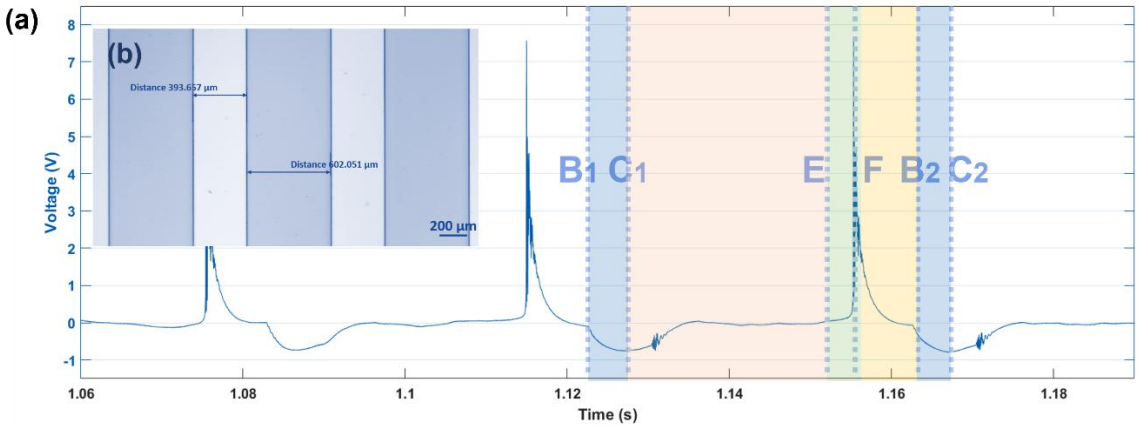

Figure 4.8 Quantitative texture sensing test on unknown grating parameters. (a) Piezoelectric voltage signals while gliding over an unknown grating-texture. (b) Optical image of the unknown grating-texture showing the actual width and distance.

Piezoelectric voltage signals were analyzed while the vibration sensors glided over a grating texture with dimensions d1 = 100 μm and d2 = 300 μm at different speeds: 5 mm/s, 20 mm/s, and 30 mm/s. As shown in Figure 4.9, it was observed that the amplitude of Peak F, generated when the sensor tips leave the grating, remains constant regardless of the speed increase from 5 mm/s to 30 mm/s. This indicates a time-independent phenomenon for Peak F, suggesting that this aspect of the sensor's response is unaffected by the rate of movement. In contrast, the amplitude of Peak C, which corresponds to state C where the sensor tips are fully in contact with the grating, increases with higher speeds. This correlation between speed and amplitude at Peak C demonstrates that the dynamic response of the piezoelectric sensors is sensitive to changes in the speed of movement, likely due to the increased force exerted on the sensors at higher velocities. This differential response to speed highlights the complex interaction between the sensor and the grating texture, which

requires further explanation from the aspect of piezoelectric mechanisms.

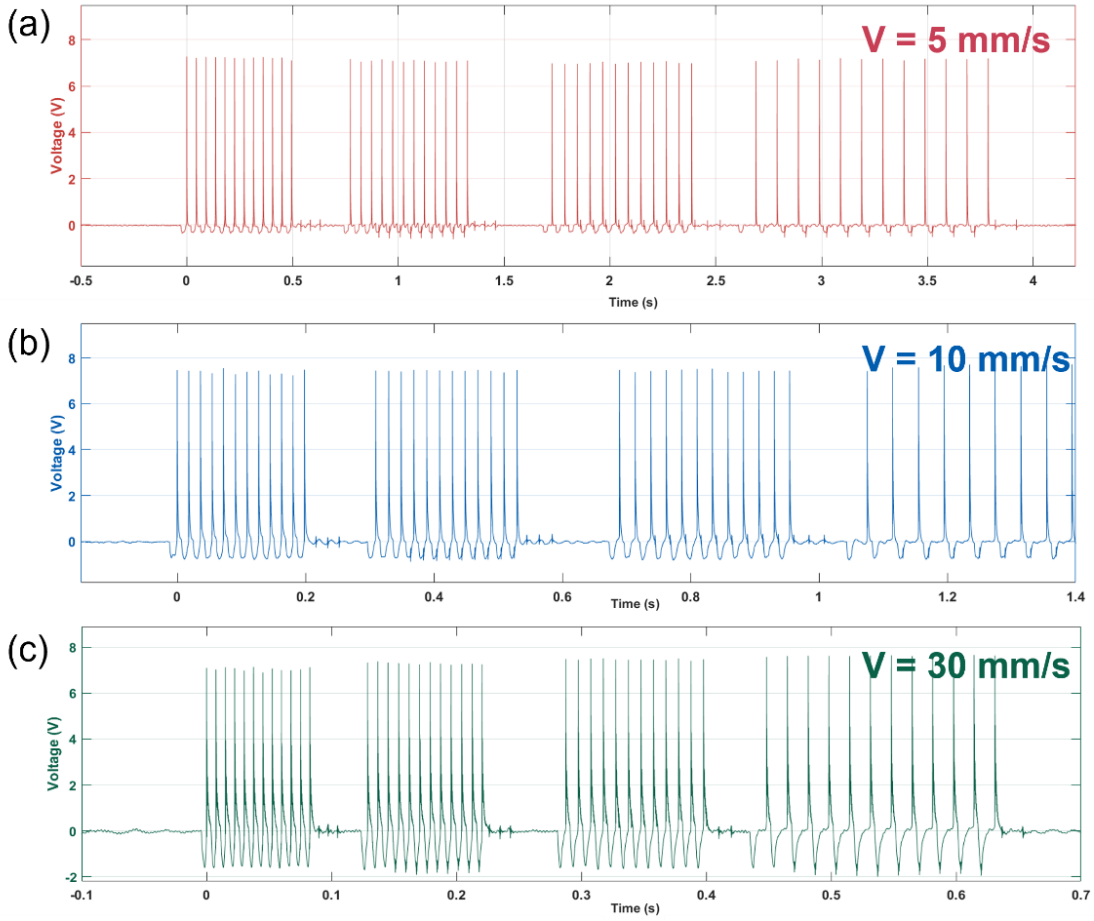

Figure 4.9 Piezoelectric voltage signals while gliding over a grating-texture (d_1 = 100 μm. d_2 = 300 μm) under different speed: (a) 5 mm/s. (b) 20 mm/s. (c) 30 mm/s.

The simplified equivalent circuit of a single piezoelectric vibration sensor in the piezoelectric tactile sensor is illustrated in Figure 4.10a. In this model, the piezoelectric layer is represented as a capacitance connected in parallel with a load resistance. This configuration results in simultaneous charge and discharge behaviors during sensor operation, which can be further analyzed through a differential equation:

$$\frac{dQ}{dt} = I$$

$$\frac{dQ}{dt} = I_{char} - I_{dis}$$

$$\frac{dQ}{dt} = \frac{dq}{dt} - \frac{Q_{dis}^2}{RC}$$

The current generated by the piezoelectric sensor, denoted as dQ/dt, comprises two components: a charging term and a discharging term. Deformation and recovery of the sensor tip induce charging, while the circuit discharges through the load resistance, which includes both internal and external resistances. According to the differential equation governing this system, an increase in the speed of deformation results in a higher rate of change of charge, dQ/dt, leading to an increase in the piezoelectric current (I) and voltage (V). However, for the instantaneous deformation responsible for Peak F, the speed of this deformation is independent of the overall tip movement speed. Consequently, the rate of change of charge, dQ/dt, remains constant, making the amplitude of Peak F a time-independent quantity.

The cyclic scanning test of the device demonstrates the long-term stability of the flexible vibration sensor, indicating that the Joule heating effect in the testing circuit has no impact and confirming the reliability of the sensor.

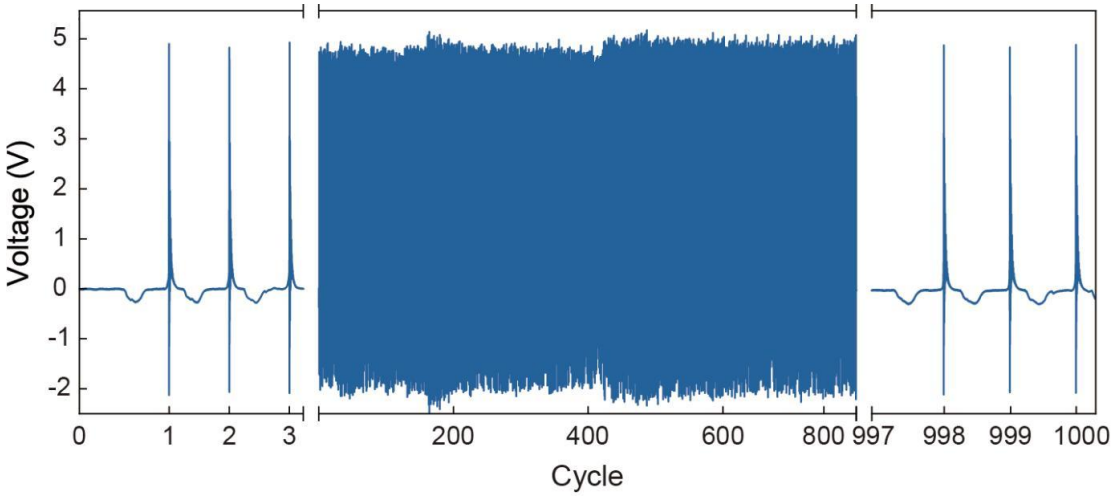

Figure 4.10. Cyclic scanning test of our device on a micro-step showed good durability.

In contrast, the deformation that produces Peak C involves a slower charging process. As the speed of the sensor tip increases, dQ/dt also increases, resulting in a higher amplitude for Peak C. This indicates that the amplitude of Peak C is positively correlated with the movement speed of the sensor tip. This analysis highlights the distinct responses of the piezoelectric sensor to different types of deformations. In a word, the piezoelectricity

aspect provides a deeper understanding of the sensor's speed-independent behavior in dynamic conditions.

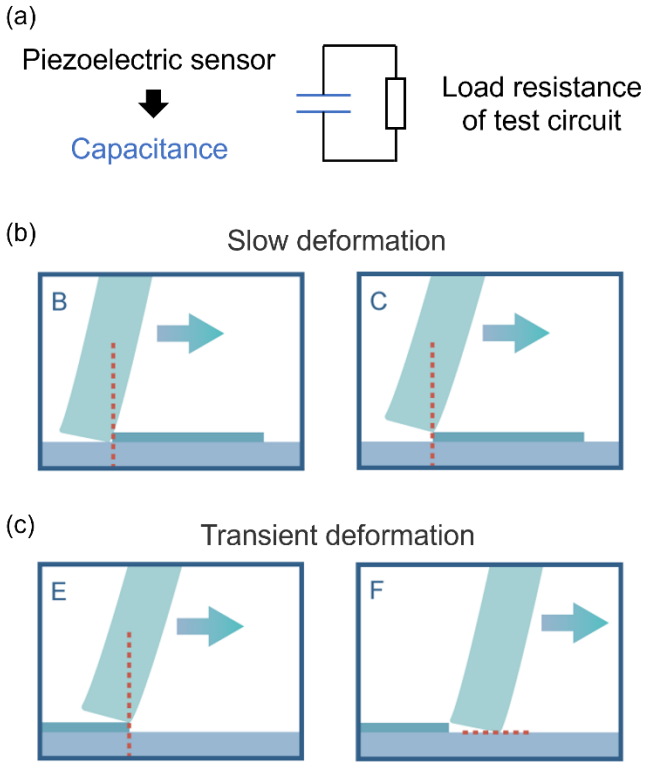

Figure 4.11 Mechanism explanation of the time-independent peak F. (a) Equivalent circuit of a single piezoelectric vibration sensor. (b) Schematic change of slow deformation which generate the peak C. (c) Schematic change of transient deformation which generate the peak F.

4.3.2 Simulation model for piezoelectric tactile sensors

The vibration sensor and grating-textures were modeled and simulated using MATLAB. First, multiphysics interfaces of solid mechanics, electrostatics, and piezoelectric effects were introduced. To calculate the time-dependent deformation and motion of the solid under transient loading, a transient analysis was performed. For the mechanical boundary conditions: (i) fixed constraints — the substrate under test was fixed, and one end of the vibration sensor was fixed while maintaining a constant distance from the substrate; (ii) free boundary — the other end of the vibration sensor was left free, forming a cantilever-like structure. For the electrical boundary conditions, the two ends of the piezoelectric film

on the vibration sensor were connected to a testing resistor and grounded. For the contact conditions, a no-penetration condition was applied between the sensor tip and the substrate. Regarding material models, PET was chosen for the vibration sensor, PVDF for the piezoelectric film, and the substrate was assigned extremely high density and Young's modulus, assuming that it would not deform under the pressure applied by the vibration sensor. Consequently, this investigation is more suitable for hard materials (e.g., silicon-based components in semiconductor processes). For soft materials such as PDMS, the piezoelectric signal would be attenuated due to damping effects. The simulation results, depicted in Figure 4.12b, demonstrate that at various speeds (10, 15, 20, 25, 30 mm/s), the amplitude of Peak F remains nearly constant, indicating a speed-independent phenomenon. This consistency in amplitude supports the hypothesis that Peak F's response is not influenced by the speed of the sensor's movement. In contrast, the simulation shows a clear positive correlation between the absolute value of Peak C's amplitude and the speed of the sensor. As the speed increases, the amplitude of Peak C also increases, aligning with the earlier explanation based on the piezoelectric mechanism. This phenomenon is attributed to the increased rate of deformation, which leads to a higher rate of charge change (dQ/dt), thus increasing the output signal amplitude. These simulation results corroborate the theoretical analysis and provide strong support for the quantitative texture sensing capabilities of the system. The findings validate the use of piezoelectric sensors for dynamic texture sensing, offering a robust method for distinguishing and quantifying surface textures based on sensor response characteristics.

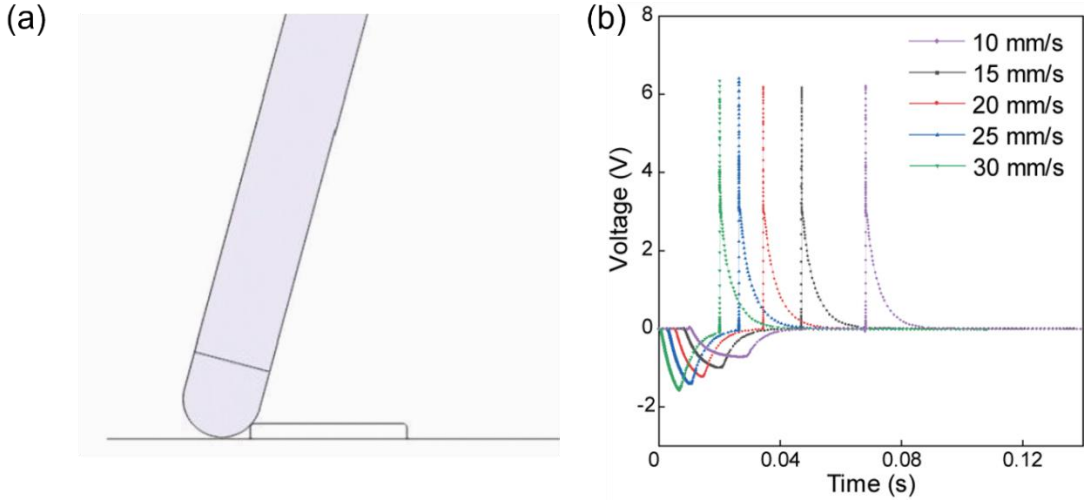

Figure 4.12 Simulation results of piezoelectric vibration sensor. (a) Configuration of

grating-texture testing using MATLAB (b) piezoelectric voltage generated by a single piezoelectric vibration sensor.

To further explore the quantitative texture sensing capabilities of the vibration sensor, the effect of grating thickness on sensor response was investigated. The sensor was moved at a constant speed of 20 mm/s across a series of grating structures with varying thicknesses, ranging from 2 μm to 98 μm. The results demonstrated a linear relationship between the amplitude of Peak F and the thickness of the gratings. This suggests that the amplitude of Peak F can be used as a reliable indicator of grating thickness. Simulation results corroborated these experimental findings, showing a consistent linear relationship between the amplitude of Peak F and the thickness of the grating structures. This agreement between experimental and simulation data confirms the robustness of the vibration sensor system for quantitative texture sensing. The ability to discern differences in thickness with such precision highlights the potential of this system for applications requiring detailed surface characterization.

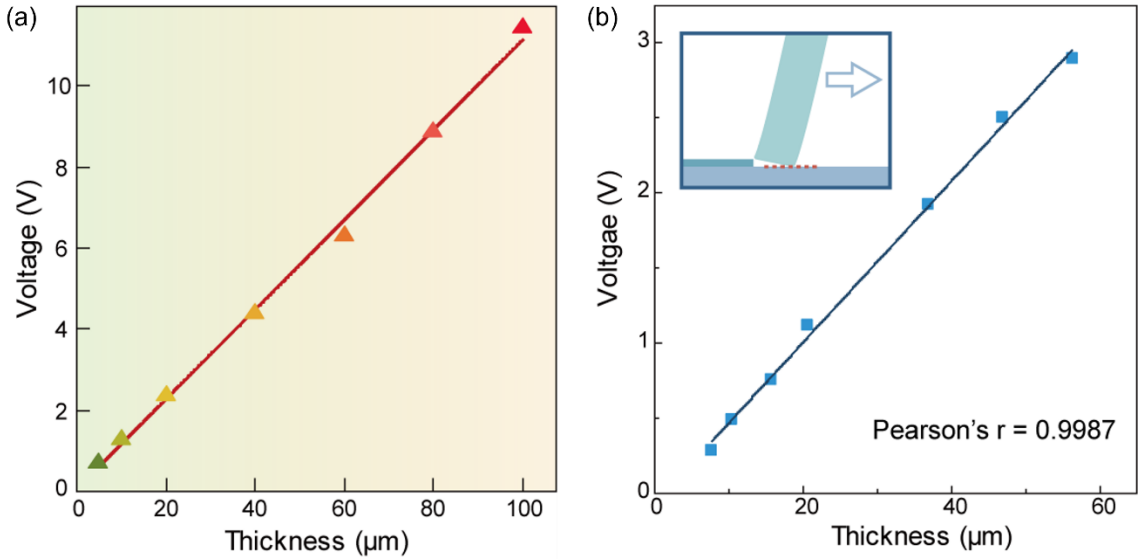

Figure 4.13 Linear relationship between the amplitude of peak F and thickness of gratings. (a) The testing results of peak F changes with thickness of grating. (b) The simulation results of peak F changes with thickness of grating.

Figure 4.14 shows the signals from the two tips of the piezoelectric tactile sensor, where the interlayer distance between the tips is denoted as Δd. By combining Δd with the time

delay (Δt_1), the instantaneous scanning speed can be extracted as $v = \Delta d/\Delta t_1$. Using the instantaneous scanning speed together with the platform movement time (Δt_2), the platform width can be calculated as $w = \Delta d \cdot \Delta t_2/\Delta t_1$. Moreover, as shown in Figure 4.11, the peak voltage is independent of the scanning speed, which enables the sensor to operate under a certain range of random speeds while still capturing the microstructural features.

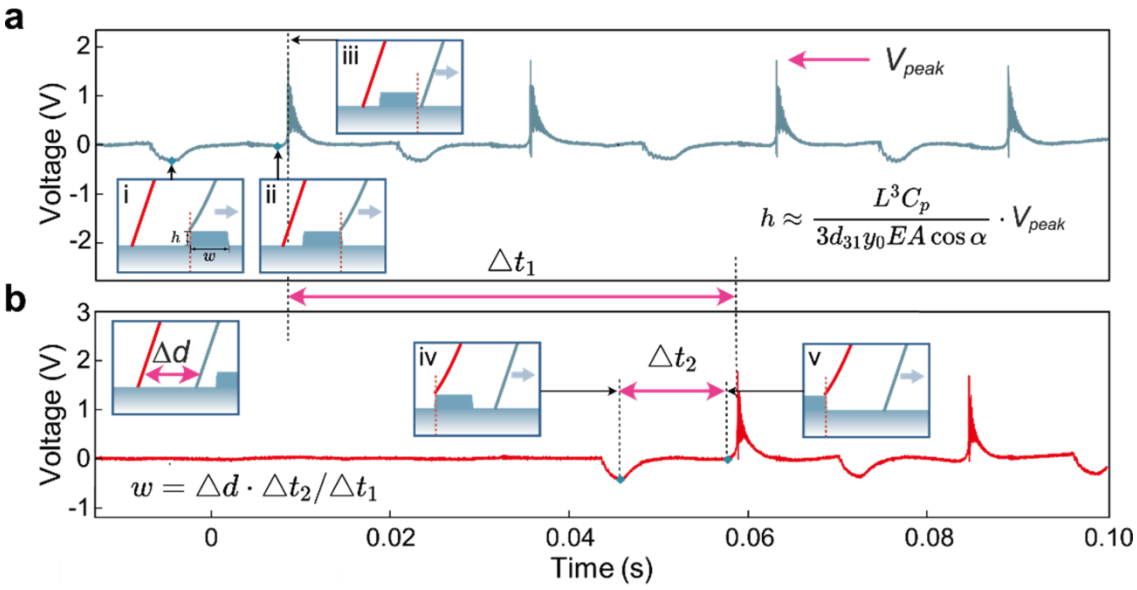

Figure 4.14 Theoretical analysis of the piezoelectric tactile sensor for quantifying height, width of surface features. Height measurement and feature analysis in piezoelectric signal when the first sensing tip (blue) scans across a step-like microstructure. Insets illustrate different states during measurement: state i, the tip fully positioned on the step surface; state ii: the tip is at the point of departing from the step edge; state iii, the tip just returns to the base level. b) Width measurement methodology based on three critical parameters: the spacing between two tips (Δd), time delay in the twin signals (Δt_1), and time interval between two states (Δt_2; states iv and v in (a)). Insets illustrate the states of the second sensing tip (red): it fully positioned on the step surface (state iv), and it is departing from the step edge (v).

4.3.3 3D-reconstruction of Micro-scale structure using piezoelectric tactile sensors

Take Leveraging the speed-independent properties of the piezoelectric tactile sensor, a

portable version of the device was developed for practical applications. The portable piezoelectric tactile sensor was used to test grating textures on a silicon wafer. As depicted in Figure 4.15, the device was operated by hand, gliding the vibration sensors over the textured surface. The first peaks of the signals from the two vibration sensors indicated a time interval of 68.2 ms. Given the distance of 1.6 mm between the sensors, the average tip speed was calculated to be 23.46 μm/ms. The calculated grating dimensions, d_1 = 583 μm and d_2 = 393 μm. were found to closely match the actual dimensions, d_1 = 600 μm and d_2 = 400 μm. This consistency demonstrates the accuracy and reliability of the portable piezoelectric tactile sensor for quantitative texture sensing. The ability of the piezoelectric tactile sensor to maintain consistent measurements even with slight variations in tip speed, up to 30 mm/s, highlights its robustness and suitability for high-speed texture characterization applications. This feature makes the portable piezoelectric tactile sensor a versatile tool for and real-time texture analysis without the requirement of steady speed and force to be applied.

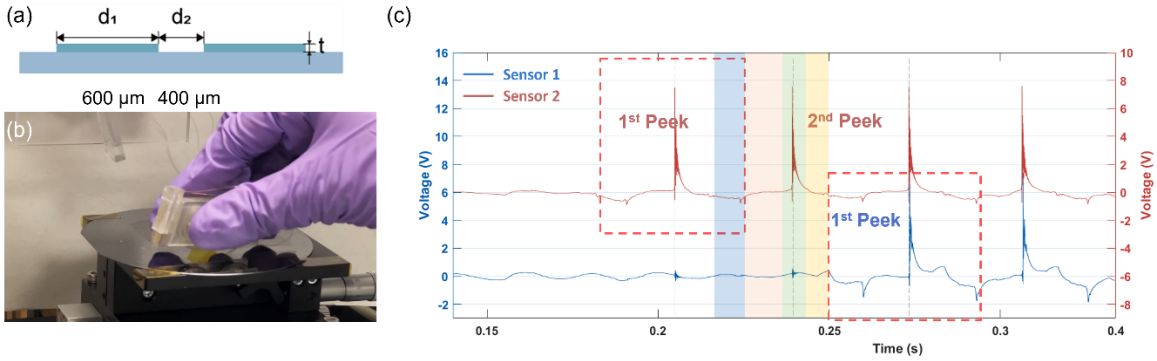

Figure 4.15 Portable piezoelectric tactile sensor and its piezoelectric voltages when operating. (a) Schematic picture of side view of the tested grating structures. (b) Picture of operation of portable piezoelectric tactile sensor. (c) Piezoelectric voltages of portable piezoelectric tactile sensor with two vibration sensors.

The spacing between the films (*Δ*d) is used to calculate the width of microstructures by determining the scanning speed. In principle, this parameter does not influence the device performance. To show this, the influence of the spacing (Δd) on the width (w) was

studied which was measurement by fabricating three devices with different spacing: 0.88 mm, 1.94 mm, 2.66 mm and scanned on micro-steps with designed widths of 200 μm, 400 μm, and 400 μm, respectively. The calculated widths were 197 μm, 398 μm, and 397 μm, respectively, yielding errors of 1.5%, 0.5%, and 0.75%, respectively. The results demonstrate that the spacing between the films does not affect the device performance. Nevertheless, we prefer to use a small spacing to achieve a compact device structure.

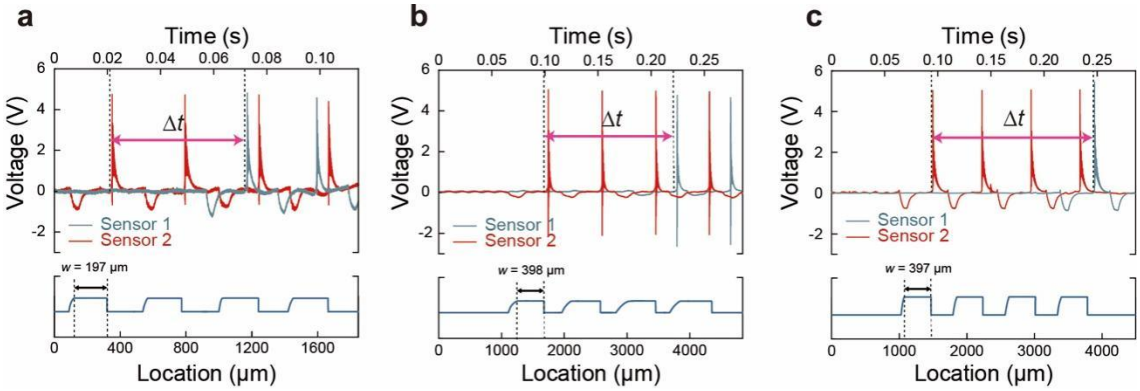

Figure 4.16. The influence of film spacing (*Δd*) on device performance: a) 0.88 mm, b) 1.94 mm, and c) 2.66 mm. Where *Δt* is the time delay between two signals.

A micro-scale Chinese knot pattern, measuring 4.5 mm × 4.5 mm, was used for a 3D reconstruction task to demonstrate the capabilities of the piezoelectric tactile sensor. The piezoelectric tactile sensor was swept over the knot pattern 40 times, capturing data in multiple directions. Three typical directional scans are shown in Figure 4.17c, highlighting the piezoelectric voltage responses. The resulting voltage signals displayed multiple peaks, corresponding to the number of grating crossings by the sensor tips. By analyzing the amplitude and time intervals between these peaks, the thickness of the grating structures was calculated. This data was then used to construct a height profile of the tip's movement over time, effectively mapping the 3D topography of the tested texture.

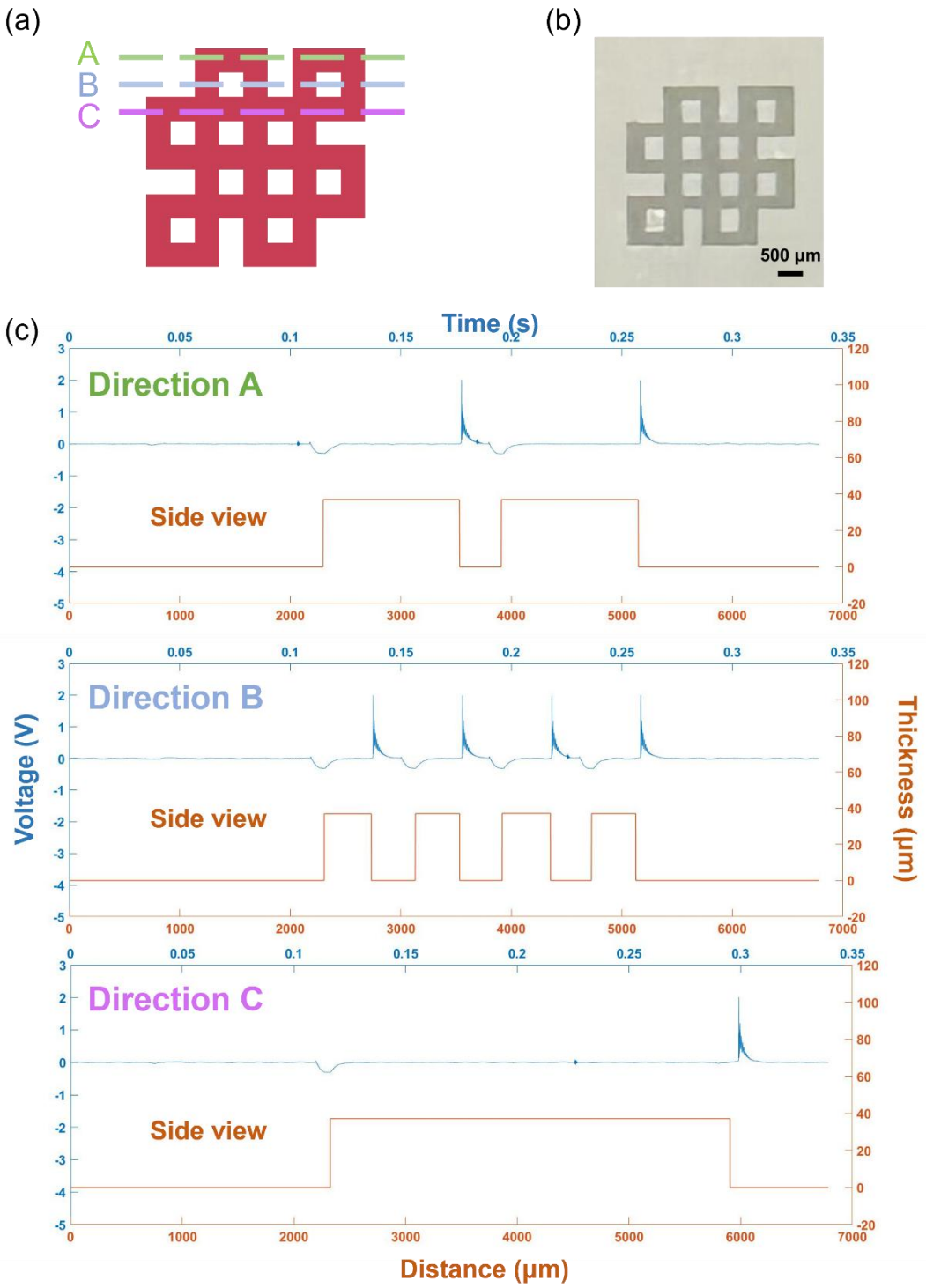

Figure 4.17 Piezoelectric tactile sensor for micro-scale patterns imaging. (a) Schematic picture of a Chinese knot patterns. Three different gliding direction are shown. (b) Optical image of the Chinese know pattern. The scale bar is 500 μm. (c) Piezoelectric voltage of the piezoelectric tactile sensor gliding test with direction A, B, and C. The calculated

thickness changes with time.

Using the piezoelectric tactile sensor, 40 parallel sweeps were conducted with intervals of 100 μm, and the resulting piezoelectric signals were used to plot a 3D heat map (Figure 4.18). This 3D heat map effectively visualizes the reconstructed surface of the micro-scale Chinese knot pattern. This technique enables precise measurement of texture features, such as the height and spacing of individual elements, highlighting the piezoelectric tactile sensor's capability in detailed surface analysis. The successful 3D reconstruction of the Chinese knot pattern using the piezoelectric tactile sensor showcases its potential for advanced tactile sensing and texture characterization applications. This method can be particularly useful in fields requiring precise surface analysis, such as materials science, biomedical engineering, and quality control in manufacturing processes.

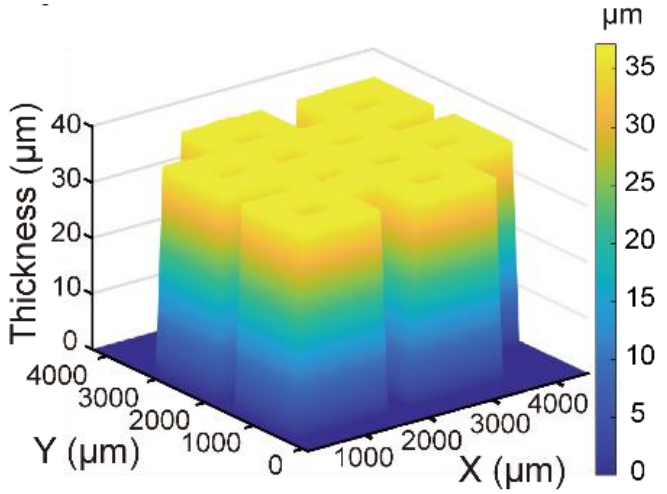

Figure 4.18 3D reconstruction heatmap of micro-scale pattern 3D-reconstruction using piezoelectric tactile sensor.

The piezoelectric tactile sensor offers several advantages over current state-of-the-art texture recognition platforms. Many existing technologies face issues such as sensor hysteresis, which limits the accurate acquisition of morphological information. Additionally, some systems only convert time-domain information into frequency-domain data for texture or roughness recognition. This frequency-domain approach is often statistical, leading to qualitative rather than quantitative texture identification. As a

comparison, we demonstrate a qualitative frequency-domain analysis using our piezoelectric tactile sensor. Figure 4.19 presents the frequency spectra of signals obtained when the sensor slides across six different 3D-printed materials: (I) BMF microArch® S240, (II) Anycubic Photon Mono M5s, (III) Stratasys Object260 Connex3 with Veroclear in glossy mode, (IV) Stratasys Object260 Connex3 with Veroblue on the side plane, (V) Stratasys Object260 Connex3 with Veroclear in matte mode, and (VI) Ultimaker 2+. Feature extraction was performed, where the number of peaks, peak coordinates, and peak amplitudes were used as inputs for LDA analysis of the texture signals, resulting in excellent peak classification with well-separated clusters. Furthermore, classification using an SVM based on the extracted features achieved 100% accuracy, with 480 samples in the training set and 40 samples in the test set (Figure 4.20d). These results demonstrate that our sensor is also capable of performing the qualitative analyses that have typically been achieved by other tactile sensing methods. Moreover, many research methodologies require controlled testing conditions, including specific speeds and forces, thereby limiting their practical application.

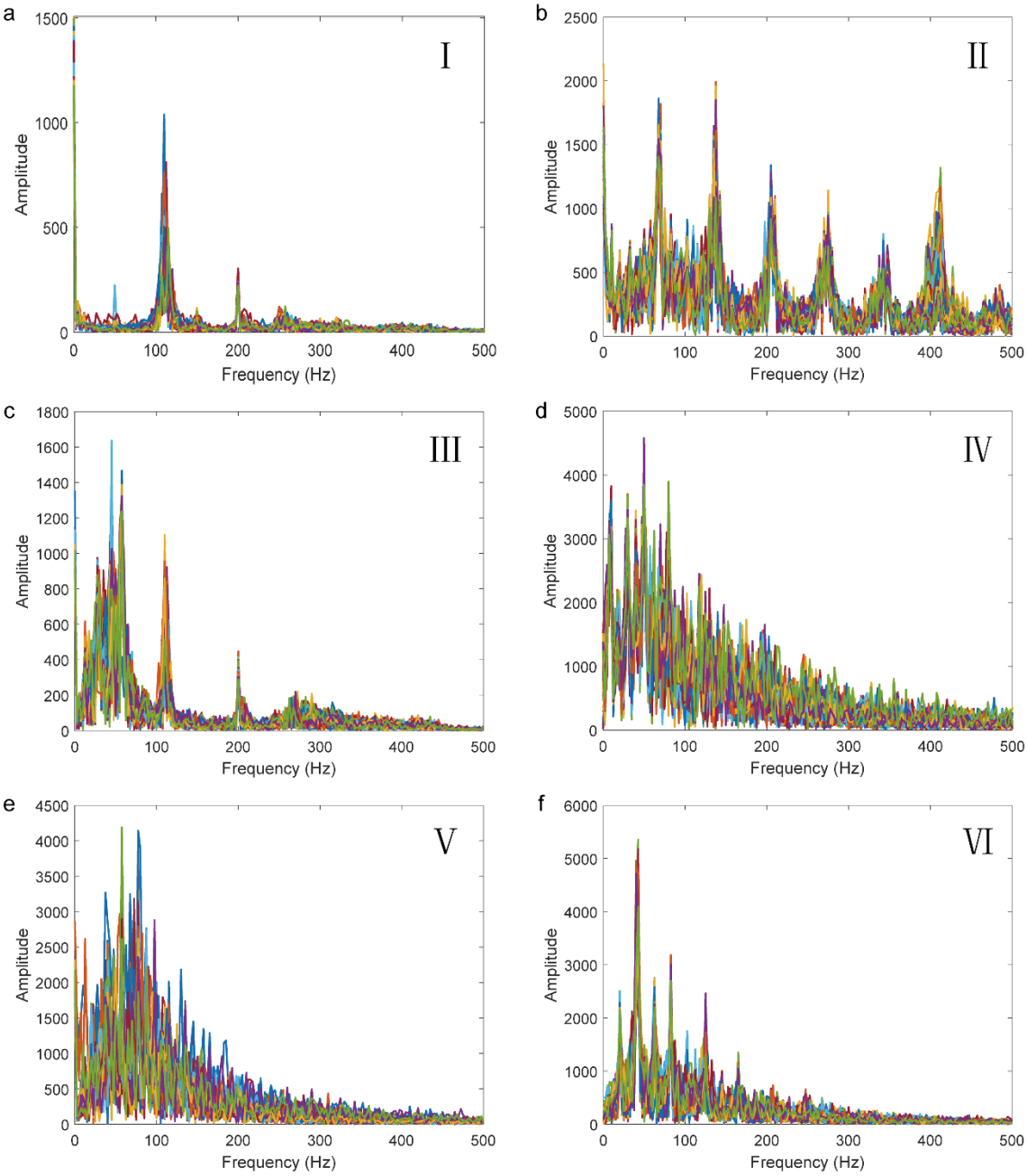

Figure 4.19 Frequency-domain signals of surface scans for six 3D-printed workpieces, obtained via Fourier transform of time-domain voltage signals, each figure containing 80 signals.

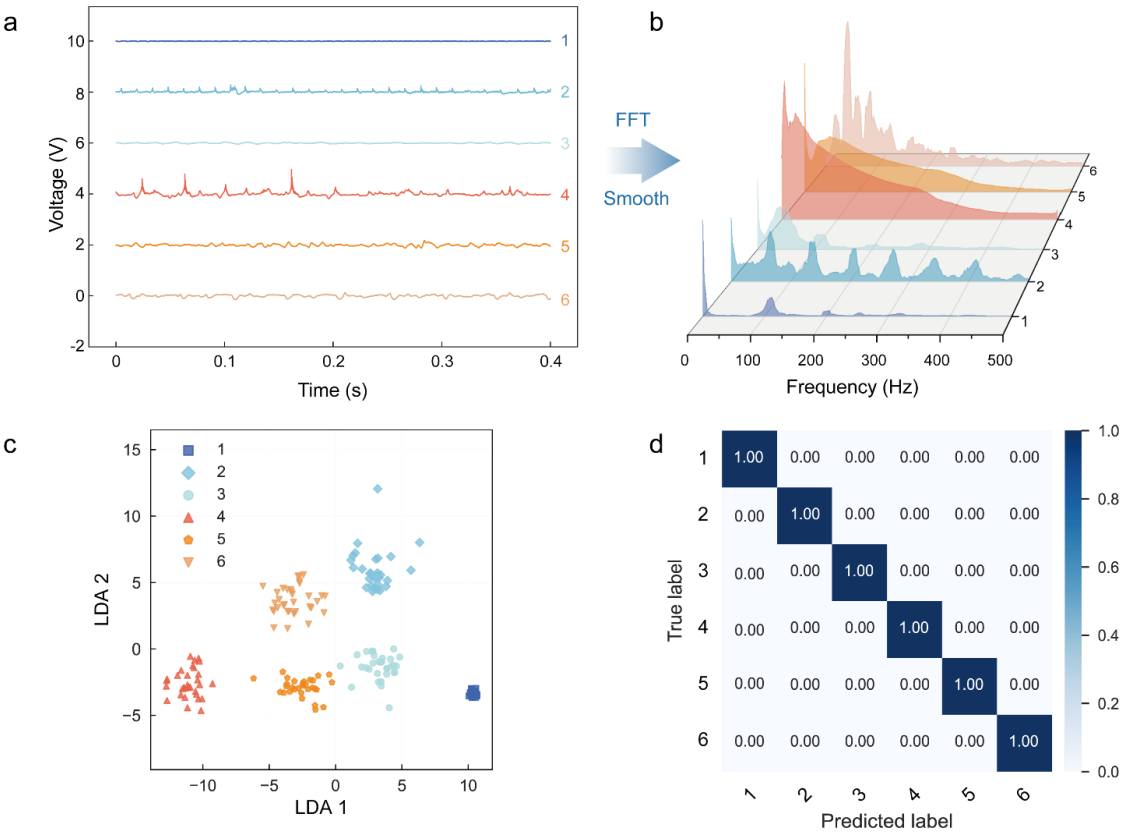

Figure 4.20 Machine learning-based roughness classification training: a) Time-domain piezoelectric signals for different textures. b) Frequency-domain signals obtained through Fourier transform, revealing distinct differences in the number of peaks, peak coordinates, and peak amplitudes. c) Feature extraction where the number of peaks, peak coordinates, and peak amplitudes are used as features for LDA analysis of texture signals, showing excellent peak classification with well-separated points. d) Classification using SVM with the extracted features, achieving 100% classification accuracy. The test set consists of 40 samples, and the training set consists of 480 samples.

In contrast, the piezoelectric tactile sensor is not affected by variations in speed or applied pressure, making it a versatile tool for texture sensing. It covers a wide sensing range, from 1 μm to several millimeters in thickness, and can detect features with widths and distances of 200 μm and above. The piezoelectric tactile sensor not only facilitates texture recognition but also enables detailed pattern imaging, providing a more comprehensive and quantitative analysis of surface textures. This capability positions the piezoelectric tactile sensor as a superior alternative for advanced tactile sensing and texture characterization,

particularly in applications where precise and reliable measurements are critical.

Table 1 Comparison of our work with current tactile technologies

Ref.	Function	Quantitative (Yes/No)	Scanning speed	Delivered results
Ref[18]	Textile classification	No	2 mm/s	20-object-type classification
Ref[19]	Texture recognition, roughness	No	NA	10-object-type classification
Ref[20]	Fabric classification	No	16 mm/s	20-object-type classification
Ref[21]	Spatial recognition, texture recognition	No	NA	Frequency: 1 Hz to 1 kHz
Ref[22]	Fabric classification	No	4.5 mm/s	15-object-type classification
Ref[23]	Texture recognition	No	NA	12-object-type classification
Ref[24]	Texture recognition	No	24 mm/s	12-object-type classification
Ref[25]	Texture recognition	No	NA	9-object-type classification
Ref[26]	Texture recognition	No	NA	5-object-type classification
This work	**Surface microstructure profiling**	**Yes**	**>40 mm/s**	**Height: 1-1000 μm, Weight: 200 μm, Random edge**

4.3.4 Edge profile reconstruction of micro-scale structure using piezoelectric tactile sensors

Furthermore, the reconstruction of microstructure edge profiles using a piezoelectric vibration sensor has been demonstrated to be feasible. In Figure 4.21b, we extract the voltage valleys and perform microelement analysis as illustrated in Figure 4.21c. By calculating the horizontal and vertical displacements of each microelement and integrating them, the random edge can be reconstructed. Several characteristic features of the voltage valley are extracted, including the initial voltage, the maximum derivative at the starting position, and the angle of the edge microelement. Based on these features, data modeling reveals the correlations shown in Figure 4.22.

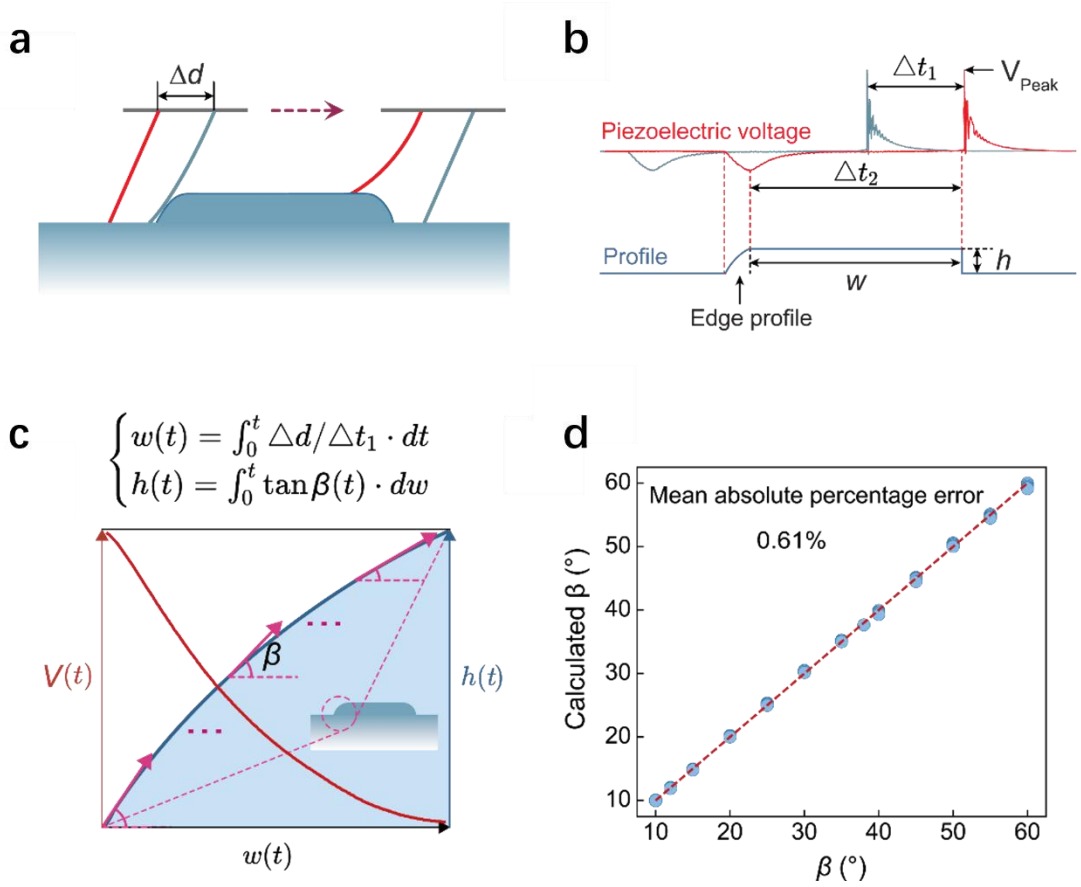

Figure 4.21 Theoretical analysis and modeling of piezoelectric vibration sensor for quantifying height, width, and edge profiles of surface features. a) Schematic showing the piezoelectric twin-film architecture (two tips) with interlayer distance (*Δ*d) as it scans a

surface microstructure. b) Schematic showing piezoelectric twin signals with a time delay (Δt_1), generated by the operation in (d) (top). Key features in the twin signals—such as peaks, valleys and time delay (Δt_1)—are systematically analyzed to extract microstructural characteristics including height (h), width (w) and edge profile. The surface profile is subsequently reconstructed (bottom). c) Schematic representation of the edge profile reconstruction. The slope angle β at each point of the edge profile can be calculated based on the piezoelectric signal $V(t)$. The x-coordinate (w) can be calculated from the t, and the y-coordinate (h) can be calculated by: $w \cdot \tan\beta$. d) The relationship between simulated slope β and calculated β showing a mean average percentage error of only 0.61%.

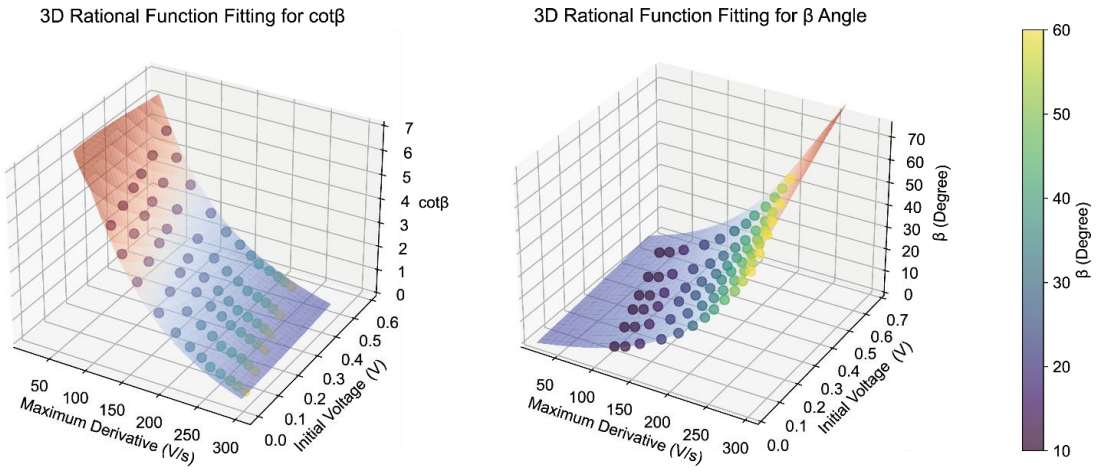

Figure 4.22 Three-dimensional rational function fitting illustrating the relationship between microstructure angle cotβ, maximum voltage derivative, and initial voltage V(0) through comprehensive parametric mathematical modeling, establishing a predictive framework for microstructure geometry characterization.

With the implementation of 3D rational function fitting for β, we analyzed a series of microelements at different angles and found that the predicted error was less than 1%, demonstrating the reliability of our model. Furthermore, we reconstructed three types of edges—convex, linear, and concave—as shown in Figure 4.24. The reconstructed profiles

exhibit high fidelity, with Mean Absolute Percentage Error (MAPE) values of 2.14%, 2.50%, and 1.92%, respectively.

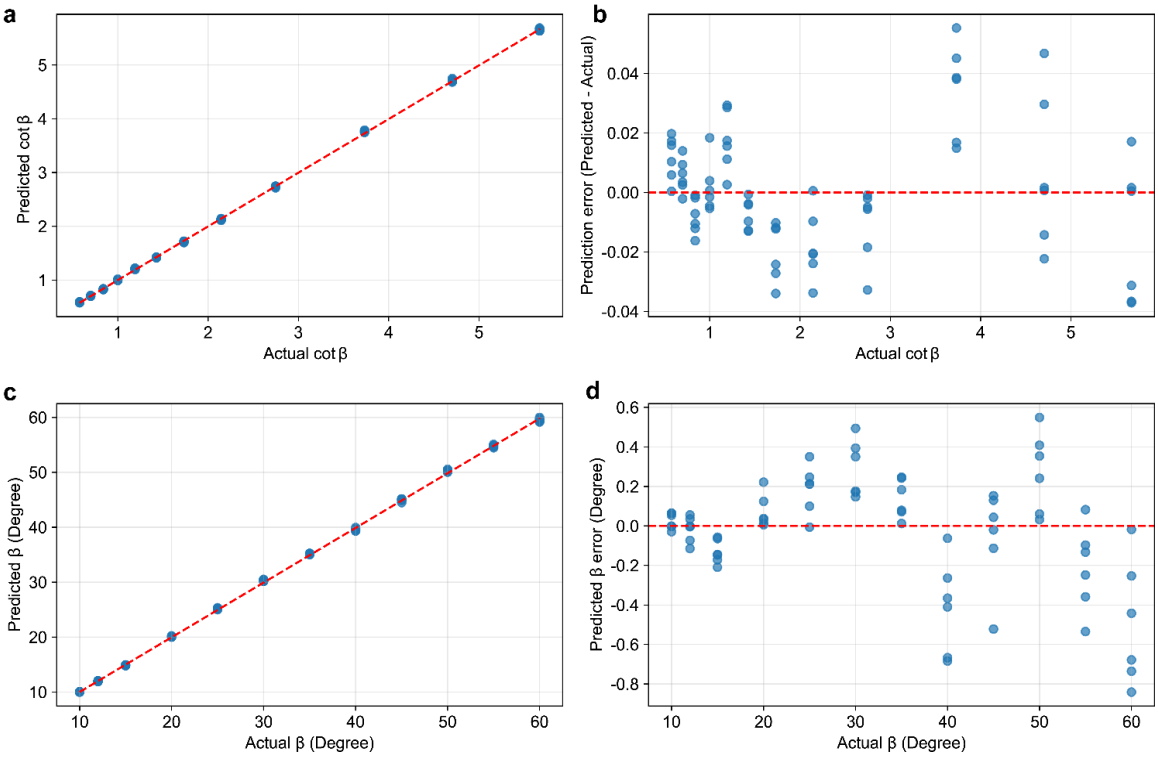

Figure 4.23 Parametric mathematical modeling for trapezoidal edge angle prediction. (a) Correlation between actual and predicted $cot\beta$ values, showing strong linear relationship with $R^2 > 0.99$ across the full range of tested angles. (b) Distribution of $cot\beta$ prediction errors, demonstrating a narrow Gaussian distribution centered near zero with standard deviation < 0.02. (c) Direct comparison between actual and predicted angle β values in degrees, illustrating excellent agreement between measured geometric parameters and model predictions. (d) Histogram of angle β prediction errors showing consistent accuracy below 1% error threshold, with most predictions falling within ±0.5%, validating the reliability of our parametric mathematical model for non-invasive microstructure characterization in flexible electronic systems.

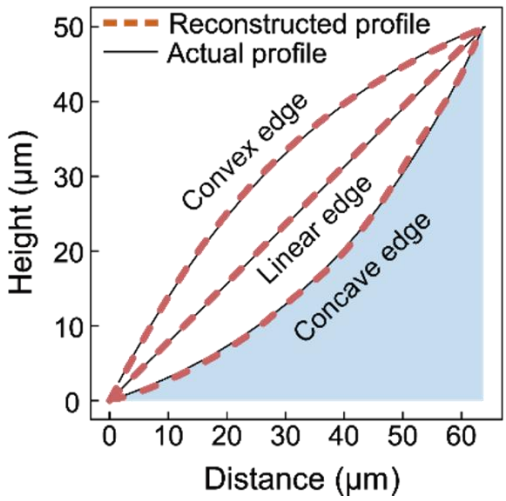

Figure 4.24 Edge profile reconstruction in three distinctive edge configurations (convex, linear, and concave edges) exhibited minimal measurement errors, with MAPE values being 2.14%, 2.50% and 1.92%, respectively. Dashed red curves: reconstructed profiles; dark line: actual edge profiles.

4.4 Conclusion

In this chapter, we have detailed the design and implementation of a piezoelectric tactile sensor tailored for the quantification of two-dimensional information from grating textures. The sensor, comprising two piezoelectric vibration sensors, features parallel PET tips mounted with flexible piezoelectric PVDF films. This configuration allows the sensor to bend and recover while sliding over uneven surfaces, with the PVDF films converting vibrations into voltage signals. The dual-tip design is crucial, as it facilitates the identification of instantaneous speed, thereby enabling accurate characterization of texture features such as groove width, bar width, and groove depth.

Furthermore, we achieved in-situ measurement of micro-scale surface profiles through a sweeping test. By correlating voltage signals with the actual movement and calculated instantaneous speed, the sensor provided detailed time-domain information. This capability was demonstrated by integrating the sensor into a robotic hand, which allowed for real-time 3D reconstruction of fine micro-scale patterns. The advancements discussed in this

chapter highlight the sensor's potential for applications requiring precise texture characterization and real-time surface profiling, underscoring the significant progress made in the field of haptic sensing technology.

References

[1] Dahiya RS, Metta G, Valle M and Sandini G. *IEEE Transactions on Robotics.* **2010**, 26, 1-20.

[2] Scheibert J, Leurent S, Prevost A and Debrégeas G. *Science.* **2009**, 323, 1503-06.

[3] Johansson RS, Flanagan JR. *Nature Reviews Neuroscience.* **2009**, 10, 345-59.

[4] Chortos A, Liu J, Bao Z. *Nature Materials.* **2016**, 15, 937-50.

[5] Howe RD, Cutkosky MR. 1989;145-50 vol.1. DOI: 10.1109/ROBOT.1989.99981

[6] Fagiani R, Massi F, Chatelet E, Berthier Y and Akay A. *Tribology International.* **2011**, 44, 1100-10.

[7] Van Boven RW, Johnson KO. *Neurology.* **1994**, 44, 2361-61.

[8] Han S, Liu C, Huang Z, Zheng J, Xu H, Chu S, Wu J and Liu C. *Advanced Materials Technologies.* **2019**, 4, 1800640.

[9] Dai H, Thostenson ET. *ACS Applied Materials & Interfaces.* **2019**, 11, 48370-80.

[10] An BW, Heo S, Ji S, Bien F and Park J-U. *Nature Communications.* **2018**, 9, 2458.

[11] Yoo J-Y, Seo M-H, Lee J-S, Choi K-W, Jo M-S and Yoon J-B. *Advanced Functional Materials.* **2018**, 28, 1804721.

[12] Lipomi DJ, Vosgueritchian M, Tee BCK, Hellstrom SL, Lee JA, Fox CH and Bao Z. *Nature Nanotechnology.* **2011**, 6, 788-92.

[13] Ho DH, Sun Q, Kim SY, Han JT, Kim DH and Cho JH. *Advanced Materials.* **2016**, 28, 2601-08.

[14] Kim M-O, Pyo S, Oh Y, Kang Y, Cho K-H, Choi J and Kim J. *Smart Materials and Structures.* **2018**, 27, 035001.

[15] Jin H, Kim Y, Youm W, Min Y, Seo S, Lim C, Hong C-H, Kwon S, Park G, Park S and Kim HJ. *npj Flexible Electronics.* **2022**, 6, 82.

[16] Qiao H, Sun S, Wu P. *Advanced Materials.* **2023**, 35, 2300593.

[17] Liu W, Yu P, Gu C, Cheng X and Fu X. *IEEE Sensors Journal.* **2017**, 17, 6867-79

[18] N. Bai, Y. Xue, S. Chen, L. Shi, J. Shi, Y. Zhang, X. Hou, Y. Cheng, K. Huang, W. Wang, J. Zhang, Y. Liu, C. F. Guo, Nat. Commun. 2023, 14, 7121.

[19] X. Guo, Z. Sun, Y. Zhu, C. Lee, Adv. Mater. 2024, 36, 2406778.

[20] S. Chun, J.-S. Kim, Y. Yoo, Y. Choi, S. J. Jung, D. Jang, G. Lee, K.-I. Song, K. S. Nam, I. Youn, D. Son, C. Pang, Y. Jeong, H. Jung, Y.-J. Kim, B.-D. Choi, J. Kim, S.-P. Kim, W. Park, S. Park, Nat. Electron. 2021, 4, 429.

[21] H. Jin, Y. Kim, W. Youm, Y. Min, S. Seo, C. Lim, C.-H. Hong, S. Kwon, G. Park, S. Park, H. J. Kim, NPJ Flex. Electron. 2022, 6, 82.

[22] Y. Qiu, F. Wang, Z. Zhang, K. Shi, Y. Song, J. Lu, M. Xu, M. Qian, W. Zhang, J. Wu, Z. Zhang, H. Chai, A. Liu, H. Jiang, H. Wu, Sci. Adv. 2024, 10, eadp0348.

[23] X. Qu, Z. Liu, P. Tan, C. Wang, Y. Liu, H. Feng, D. Luo, Z. Li, Z. L. Wang, Sci. Adv. 2022, 8, eabq2521.

[24] S. Chun, W. Son, H. Kim, S. K. Lim, C. Pang, C. Choi, Nano Lett. 2019, 19, 3305.

[25] H. Qiao, S. Sun, P. Wu, Adv. Mater. 2023, 35, 2300593.

[26] S. Shu, Z. Wang, P. Chen, J. Zhong, W. Tang, Z. L. Wang, Adv. Mater. 2023, 35, 2211385.

Chapter 5

An intelligent piezoresistive tactile system for in-situ quantifying object features

This chapter details the design, fabrication, characterization and application of stability-enhanced tactile gloves. The tactile gloves are fabricated by integrated pressure sensing arrays onto fabric gloves. The pressure sensing array are fabricated by hot-pressing method to laminate piezoresistive layers onto interdigital electrodes. A bimodal stability-reinforced method containing surface modification and encapsulation is utilized for sensor optimization. Herein, a robust 142-channels tactile glove is introduced. A healthcare related classification task is carried out. The machine learning results show that tactile gloves are promising candidates for application on palpation-related diagnosis.

---

*This section was published substantially as:

Jiaqi Tu, Ming Wang, Wenlong Li, Jiangtao Su, Yanzhen Li, Zhisheng Lv, Haicheng Li, Xue Feng, Xiaodong Chen. Electronic skins with multimodal sensing and perception. *Soft Sci* 3:25 (2023). DOI: 10.20517/ss.2023.15. (No written permission from OAE Publishing Inc. is necessary for thesis purpose)

5.1 Introduction

In recent years, the development of tactile sensing arrays and tactile gloves has shown significant promise in healthcare-related applications. These innovative technologies combine advanced materials, precise sensor design, and sophisticated data analysis methods to create systems capable of detailed and accurate tactile sensing. This thesis explores the design, fabrication, and application of a tactile glove integrated with an interdigital circle-patterned electrode array and flexible printed circuits (FPCs), aiming to enhance the stability and reliability of tactile feedback in medical diagnostics and other healthcare applications.

The core of this research involves surface modification and encapsulation method to enhance the working stability of the pressure sensors. With the integration of the flexible pressure sensing array and fabric glove, a tactile glove was introduced. It features a user-friendly data acquisition system, equipped with a Bluetooth-enabled flexible PCB powered by a lithium battery. The system includes an interactive User interface (UI) that visualizes force distribution and sensor resistance changes in real-time, offering modes such as profile mode and thermal mode. These visualization tools allow for easy data readout, saving, and automatic sensor calibration, enhancing the usability of the glove in various applications.

One of the key applications of this tactile sensing system is in healthcare, particularly for object classification tasks related to medical diagnostics. By interacting with silicone gel breast models that simulate healthy and abnormal conditions, the glove can distinguish between different types of nodules based on their tactile properties. Besides, there are 8 geometric solids to be classified, which demonstrates the possibility of quantitative analysis in the field of medical palpation. The classification tasks demonstrated high accuracy, with a support vector machine (SVM) method achieving a recognition accuracy of 99.18% on a test set. Principal component analysis (PCA) further validated the system's capability to differentiate between various object types, including medical models and geometric solids.

This research highlights the potential of tactile gloves in medical diagnostics, offering non-invasive methods for assessing tissue properties and detecting abnormalities. The integration of advanced sensing technology, machine learning algorithms, and real-time data visualization paves the way for further advancements in tactile sensing and interactive technologies. The stability-enhanced tactile sensing array, combined with the versatility and accuracy of the tactile glove, represents a significant step forward in developing intelligent and responsive healthcare tools.

5.2 Experimental methods

5.2.1 Preparation of functional sensing materials and sensor protrusion for pressure sensors

For the functional sensing materials, we selected Velostat (Custom Materials, 3M) piezoresistive film. To create the pressure sensing layer, we used a 2 mm drift pin to punch out circular pieces with a diameter of 2 mm (Figure 5.1). SIL-POXY™ (SMOOTH-ON) was chosen for the preparation of the protrusions. The process involved applying SIL-POXY to a mold containing a 10x10 array of semicircular holes, each with a diameter of 2 mm. After allowing the SIL-POXY to cure completely for 5 minutes, we obtained hemispherical protrusions. Subsequently, SIL-POXY was used to bond these protrusions to the polyurethane (PU) layer, ensuring a secure attachment and creating the desired pressure sensing structure.

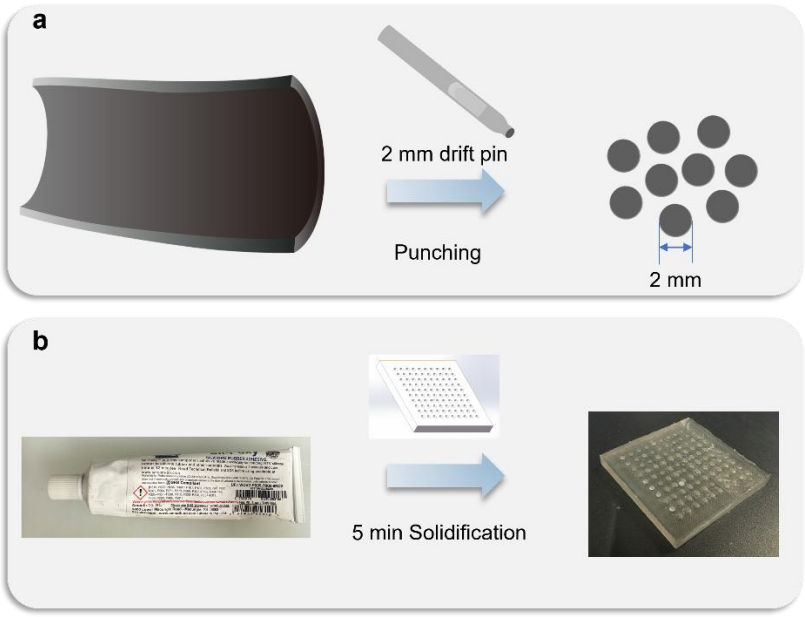

Figure 5.1 Preparation steps of pressure sensors

5.2.2 Surface modification of piezoresistive layer and flexible printed circuits

The previously prepared functional sensing layer underwent oxygen plasma treatment on both sides using a plasma surface treatment machine (nano, Diener) for 3 minutes at 70% power. Following the plasma treatment, the layer was placed in a sealed container alongside an independent small container containing (3-mercaptopropyl) trimethoxysilane (3-MPT) ($HS(CH_2)_3Si(OCH_3)$; Sigma-Aldrich). The sealed container was then heated at 80°C for 3 hours. After heating, the layer was rinsed with ethanol and soaked in ethanol for 30 minutes.

In parallel, the customized flexible printed circuit (FPC) also underwent oxygen plasma treatment and was subsequently immersed in alcohol with a concentration of 10 mmol/L for 3 hours. After this immersion, the FPC was rinsed with ethanol, soaked for 30 minutes, and then dried at 60°C.

5.2.3 Preparation of pressure sensors

4g Waterborne PU (HydroMed D7, AdvanSource) particles are added into 36g ethanol

To prepare the adhesive solution, 4g of waterborne polyurethane (WPU) particles (HydroMed D7, AdvanSource) were added to 36g of ethanol (Sigma-Aldrich). The mixture was sonicated using an ultrasonic machine to completely dissolve the WPU particles. The resulting 10 wt% WPU solution was then applied to the surfaces between 50-μm PU films (sourced from Taobao) and the flexible printed circuit (FPC). The FPC and PU film were integrated using a hot press at 110°C and 2 MPa for 2 minutes. The same WPU/ethanol solution was used to adhere the surfaces between the PU films and the piezoresistive films. This was achieved by hot pressing at 80°C for 1 minute. After forming these two layers, they were adhered together using hot pressing at 80°C for 1 minute, leveraging the residual WPU on the PU layers. Finally, the protrusions were adhered to the assembled layers, completing the fabrication of the tactile sensing array (as illustrated in Figure 5.2). This process ensures strong bonding and structural integrity, essential for reliable tactile sensing performance.

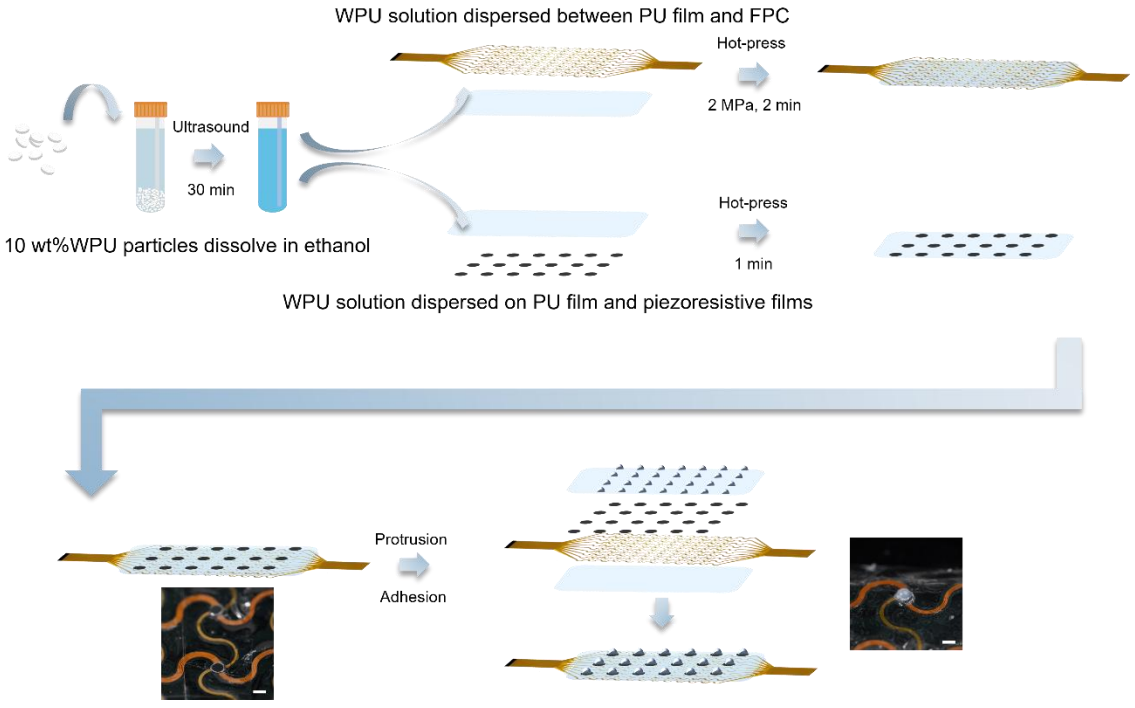

Figure 5.2 Preparation steps of tactile sensing array.

5.2.4 Mechanical characterization of pressure sensors

The pressure and bending sensing capabilities were evaluated using a custom-built mechanical testing platform. Resistance changes during bending and pressing were measured with a parameter analyzer (Keithley 2450). For pressure sensing, the platform's moving head oscillated back and forth over a distance of 0.35 mm at a strain rate of 10% strain/s. This setup allowed for precise measurement of resistance changes under pressure. For bending tests, the samples were subjected to shear strength testing using a mechanical tester (MTS Criterion model C42). The testing samples were stretched until desorption occurred at a strain rate of 50 mm/min. These tests ensured the reliability and robustness of the pressure and bending sensing functions of the tactile sensing array, providing critical data for further optimization and application in healthcare-related settings.

5.2.5 Characterization of surface modification results

For FTIR (Fourier Transform Infrared) spectrometer in Attenuated Total Reflectance (ATR) mode, begin by placing the sample, such as the Velostat film, onto the ATR crystal. Ensure good contact between the sample and the crystal for optimal signal transmission. Set the spectrometer (FTIR, Perkin Elmer Frontier) to the desired scanning range, covering both the C-H vibration region and low-frequency region (e.g., 4000 cm^{-1} to 600 cm^{-1}). Start the measurement and record the spectrum, identifying key peaks such as the asymmetric and symmetric stretching vibrations of methylene groups, the silicon-oxygen-silicon bond stretching modes, and the deformation mode of methyl groups. Analyze the data to confirm the successful bonding of functional groups, which is crucial for the enhanced interfacial adhesion and performance of the sensor. Save the spectra and interpret the results to assess the chemical modifications made to the sample.

For X-ray Photoelectron Spectroscopy (XPS) analysis (using Thermo Fisher K-Alpha Photoelectron Spectrometer), start by preparing the samples, including the modified Velostat film and gold electrodes on the flexible printed circuit (FPC). Place the samples in the XPS chamber and evacuate the chamber to achieve a high vacuum environment. Set the XPS to analyze the Si and S 2p regions, which are key indicators of the presence of 3-Mercaptopropyltrimethoxysilane (3-MPT). Using a monochromatic Al Kα source,

irradiate the sample surface and collect the emitted photoelectrons. Record the spectra, focusing on the binding energy peaks corresponding to silicon (Si 2p) and sulfur (S 2p). Analyze the spectra to confirm the presence of these elements, indicating successful surface modification with 3-MPT. Finally, interpret the data to verify the formation of gold-sulfur bonds and the overall modification of the samples.

5.2.6 DSC analysis for encapsulation parameter

To measure the thermal properties of the piezoresistive film using Differential Scanning Calorimetry (DSC), begin by preparing a sample of the film. Place the sample in a DSC pan and seal it. Load the pan into the DSC instrument along with a reference pan. Set the temperature range for the analysis, typically from room temperature to a specified upper limit, in this case, above the softening temperature of the piezoresistive film. Program the DSC to heat the sample at a controlled rate, such as 10°C per minute. As the temperature increases, the DSC records the heat flow associated with phase transitions, such as softening or melting. Analyze the resulting thermogram to identify key thermal properties, such as the softening temperature. Use the data to set process temperatures below these thresholds to maintain material integrity and ensure strong adhesion in multi-layer structures.

5.3 Results and discussion

5.3.1 Optimization and characterization of pressure sensor arrays for tactile sensing systems

The electrodes are designed in interdigital circle patterns. As shown in Figure 5.3a, the diameter of each sensor electrode is 2 mm. The distance of the counter electrodes is 200 μm. With the μm-scale electrodes design, double-layer FPC with electrodes arrays are introduced. There are two layers of copper circuits. One is embedded in PI layers, and the other is laminated on the top of PI encapsulation layer. Two copper circuit layers are electrically connected with holes at corresponding locations (Figure 5.3a). With the

fabrication processes, one double-layer FPC is designed in a square array with 100 channels for sensor characterization. The other double-layer FPC is designed in hand-shape array for further integrated on fabric gloves. As shown in Figure 5.3c, the hand-like FPC contains 7 parts. Four parts are 3X7 electrode arrays which refer to index finger, middle finger, ring finger, and pinky finger. One part is a 3X6 electrode array which refers to thumb finger. Additionally, there are two sections with 4x5 electrode arrays representing the left and right palms. The distance between electrodes is 5 cm in horizontal spacing or 9 cm in horizontal spacing. Among the palm parts, the distance between electrodes is 10 cm in horizontal spacing or 12 cm in horizontal spacing. These variations in distances indicate different sensor distribution densities. The sensor distribution is denser in the finger areas, aligning with the higher density of mechanoreceptors in human fingers compared to palms.

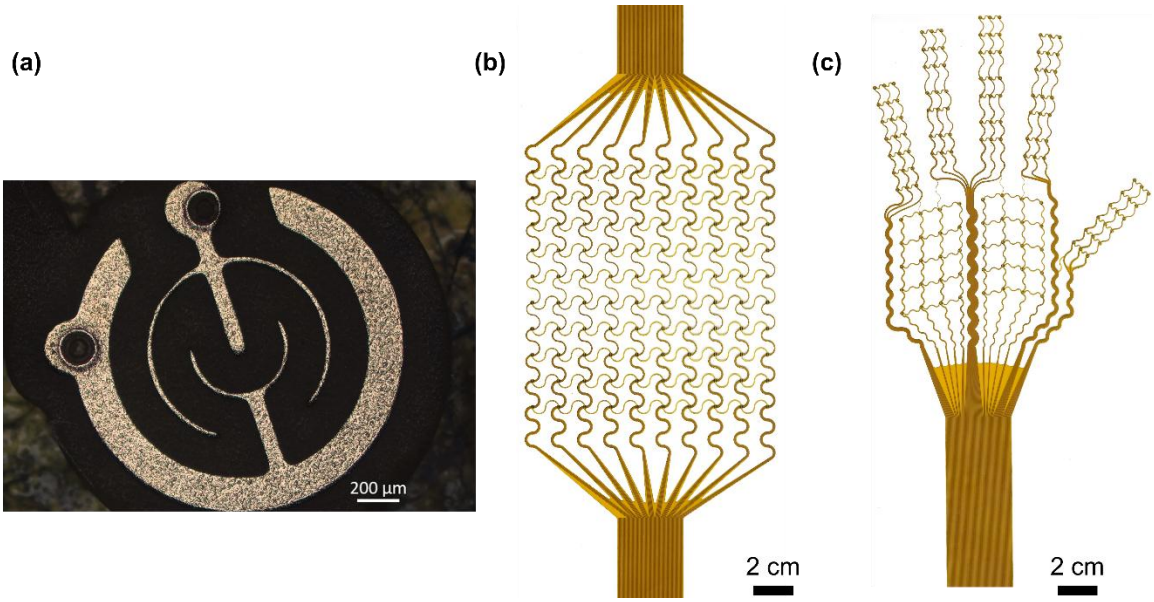

Figure 5.3 Images of single electrodes and electrodes array. (a) Optical microscope image of a single interdigital circle-like electrodes. Scale bar is referred to 200µm. (b) Image of a double-layer FPC with electrodes containing 100-channels. (c) Image of a hand-like double-layer FPC with electrodes containing 142 channels.

After surface modification, the piezoresistive layers and the gold electrodes on the FPC layers are expected to bond with (3-Mercaptopropyl)trimethoxysilane (3-MPT). To confirm the successful reaction between 3-MPT and Velostat films, which primarily

contain polypropylene and carbon black, FTIR was employed to analyze the related chemical bonds. Due to the inherent high noise of carbon materials, the untreated Velostat film was used as a baseline for comparison.

The FTIR spectra of the samples were measured in Attenuated Total Reflectance (ATR) mode. The FTIR-ATR spectrum for the C-H vibration region is presented in Figure 5.4a. The two peak structures at 2916 cm^{-1} and 2849 cm^{-1} correspond to the asymmetric and symmetric stretching vibrations of methylene groups ($\nu_a(CH_2)$ and $\nu_s(CH_2)$, respectively). Additionally, the broad bands near 1008 cm^{-1} and 791 cm^{-1} are attributed to the stretching modes of silicon-oxygen-silicon (ν(Si−O−Si)) bonds. The sharp peak at 1265 cm^{-1} is due to the deformation mode of methyl groups ($\delta(CH_3)$) from the two $Si-CH_3$ groups (Figure 5.4b). Therefore, the presence of characteristic peaks in both the C-H vibration region and the low-frequency region of the FTIR-ATR spectrum indicates successful bonding of 3-MPT to the surface of the Velostat film. This bonding is essential for enhancing the interfacial adhesion between the piezoresistive layers and the gold electrodes, thereby improving the overall performance and reliability of the sensor.

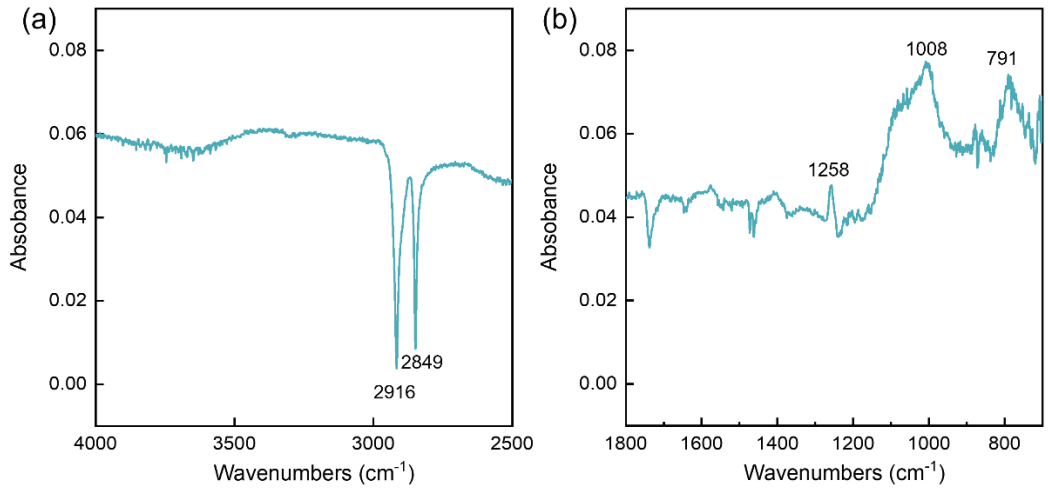

Figure 5.4 FTIR-ATR spectrum of Velostat film samples. (a) ν(C−H) region. (b) Low-frequency region.

Due to the strong binding energy between gold and thiol groups, forming a gold-sulfur bond, 3-Mercaptopropyltrimethoxysilane (3-MPT) is expected to successfully modify the gold electrodes on the flexible printed circuit (FPC). To further ensure the surface

modification of the Velostat film, we treated its surface with plasma and placed it in a sealed container with 50 µL of 3-MPT at 80°C for 4 hours.

To verify the modification, X-ray photoelectron spectroscopy (XPS) was conducted on the modified piezoresistive film and the gold electrodes on the FPC. The XPS spectra for the Si and S 2p regions of both the Velostat film and the gold electrodes confirmed the presence of silicon and sulfur, which can only originate from 3-MPT. These results conclusively demonstrate the successful surface modification of both the Velostat film and the gold electrodes on the FPC with 3-MPT.

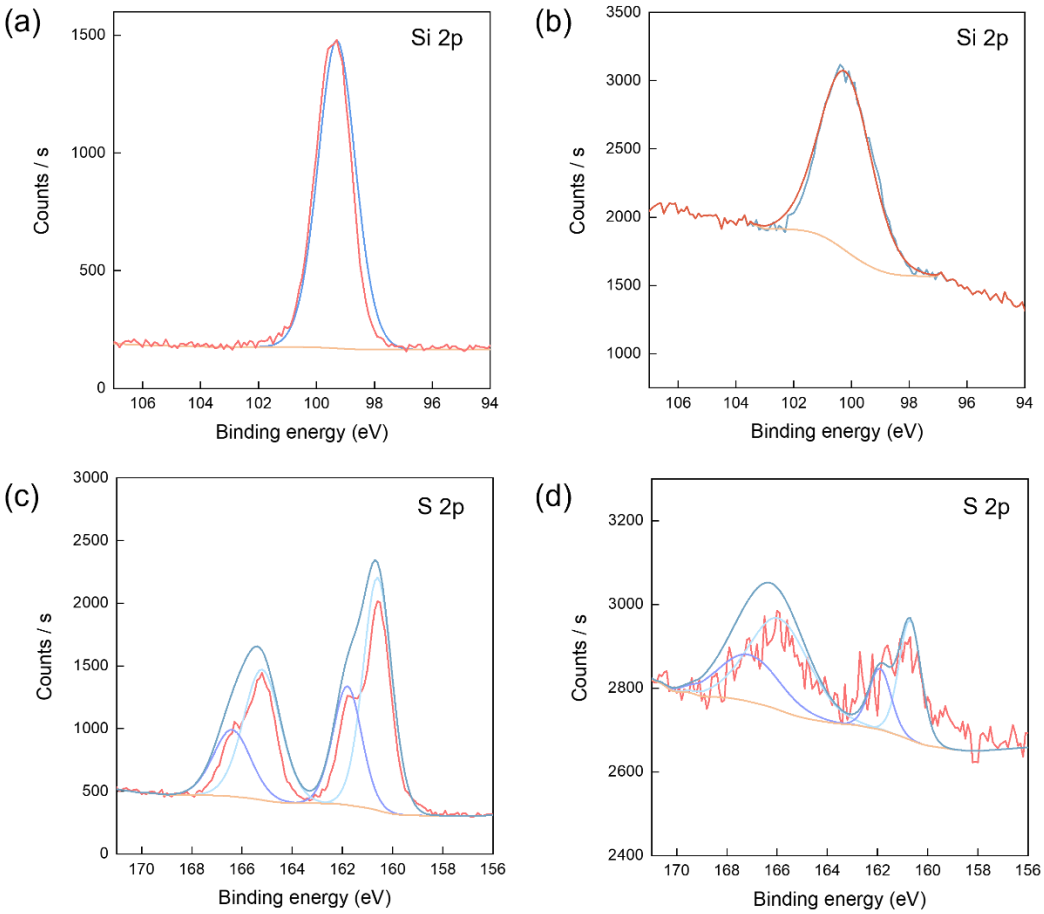

Figure 5.5 XPS spectrum of element analysis of the modified piezoelectric film and gold electrode on FPC. (a) Si 2p spectra of Velostat piezoelectric film. (b) Si 2p spectra of gold electrode on customized FPC. (c) S 2p spectra of Velostat piezoelectric film. (d) S 2p spectra of gold electrode on customized FPC.

The thermal properties of the piezoresistive film were measured using differential scanning calorimetry (DSC). The results indicate that the softening temperature of the piezoresistive film is approximately 100°C. Therefore, the process temperatures related with the piezoresistive films are all set to below 100°C. Additionally, the softening temperature of PU is around 110°C. This softening temperature suggest that a strong adhesion can be achieved when using a hot-press technique under 110°C to bond the PU layer with PI layer. This firm adhesion is crucial for maintaining the integrity and performance of the layered structure in various applications, ensuring durability and reliability of pressure sensors.

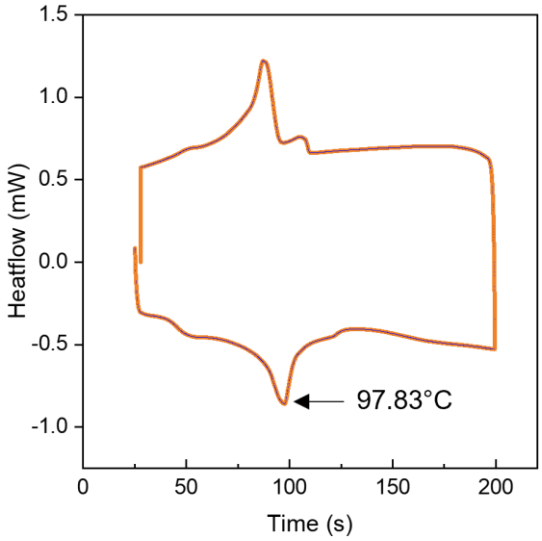

Figure 5.6 Thermal property of the piezoresistive film by DSC

To assess the stability of the pressure sensors, the initial resistance of the sensors was compared between the first version of the tactile arrays[1] and the new tactile sensing arrays. Specifically, the coefficient of variation of the initial resistance values was analyzed for both versions (Figure 5.7).

For the new version, the mean initial resistance was found to be 19,093.56 Ω, with a standard deviation of 9,367.69. The calculated coefficient of variation (defined as the ratio of the standard deviation to the mean) was 0.49. This value is lower than that of the previous version, indicating an improvement.

The reduced coefficient of variation in the new version signifies enhanced consistency in the initial resistance values of the pressure sensors. This improvement in consistency is indicative of higher stability in the sensor performance. Such stability is crucial for the reliable operation of tactile devices, as it ensures more accurate and repeatable force measurements across different sensors and usage scenarios.

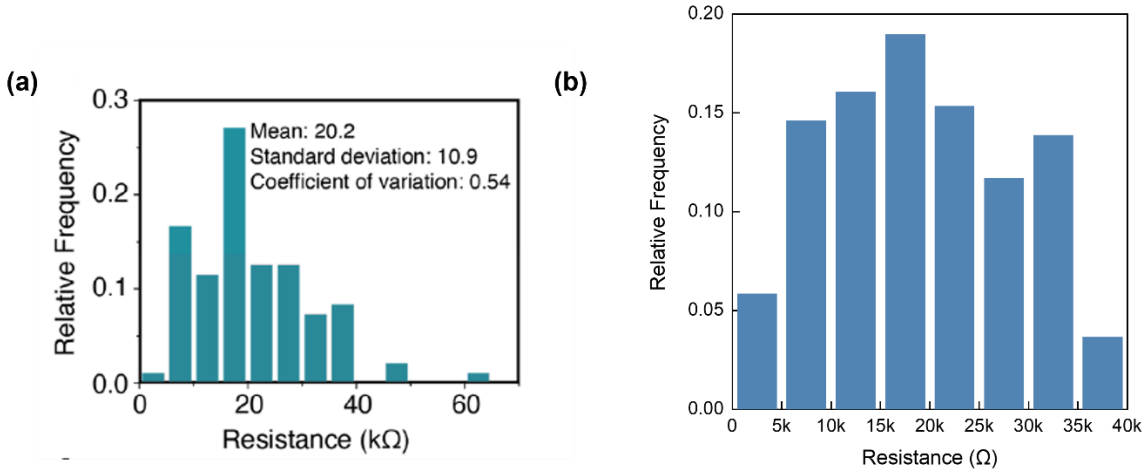

Figure 5.7 Consistency comparison between stability-enhanced pressure sensors and sensors from first version of tactile arrays. Coefficient of variation (ratio of standard deviation/mean) of the statistical initial resistance values of (a) First version (112 sensors). (b) New version (100 pressure sensors).

As a tactile glove primarily designed to capture force-related information during interactions between objects and the glove, it is crucial to minimize undesired signals generated by finger movements without object contact. To address this, the bending stability of a single pressure sensor was tested first. A laboratory-built bending test platform was utilized for this purpose. This platform is capable of performing both positive and negative bending tests. For stable bending conditions, a pressure sensor array was mounted on a 100 μm PET substrate. The sensor array was securely fixed to the moving part of the platform using magnetic rings to ensure consistent positioning during the bending tests. The bending test of a single pressure sensor involved bending the sensor from 0 to -30° and then from 0 to +30°. As illustrated in Figure 5.8, the change in resistance ($\Delta R/R_0$) was only 0.28%. This negligible change in synchronous resistance during the bending test demonstrates the high bending stability of the pressure sensor. This high stability is

essential for the reliable performance of the tactile glove, ensuring that the sensors provide accurate force measurements during object interactions while minimizing false signals from finger movements.

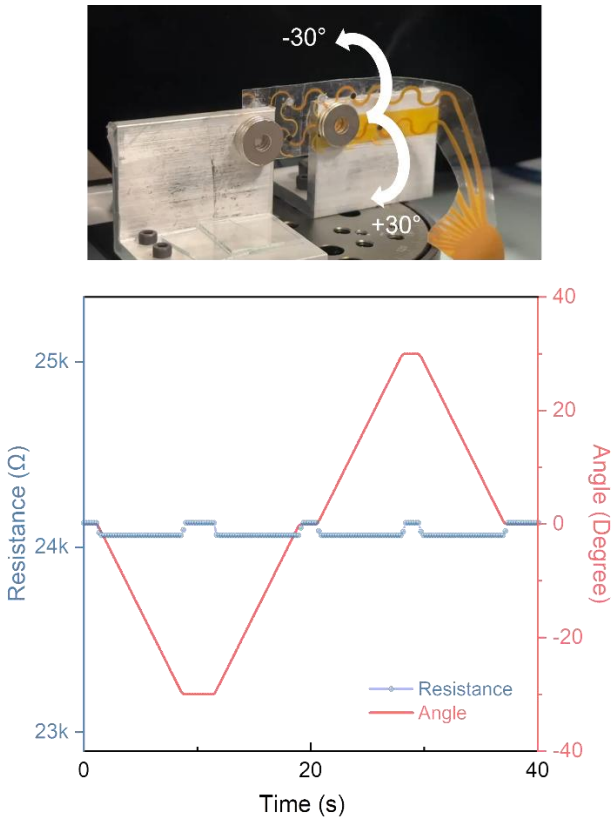

Figure 5.8 Bending test of a single pressure sensor. The sensor is bended from 0 to -30° and then from 0 to +30°. The synchronous resistance change is shown.

Following the bending test of the single pressure sensor, the bending stability of the sensors under working conditions was evaluated. A 142-channel hand-shaped pressure sensor array was integrated into a fabric glove to facilitate this test. The tester wore the tactile glove and performed various gestures, including the natural states '5', '4', '3', and '2'. The signal changes over a 4-second period for all 142 sensors are depicted in Figure 5.9. The majority of the channels exhibited a resistance change ($\Delta R/R_0$) of less than 5%. A few sensors showed relatively larger resistance changes, though still below 10%. The sensors that exhibited larger resistance changes, up to 10%, is due to contact between the sensors and the palms. This interference, however, is expected to be minimized in practical applications,

as the fingers will primarily interact directly with objects rather than with other fingers or the palms. In real-world scenarios, the primary function of the tactile glove is to detect forces exerted on the fingertips during object manipulation. Therefore, the occasional contact between the sensors and the palms, which contributes to the observed resistance fluctuations, will have a minimal impact on the glove's overall performance. These results indicate good stability of the pressure sensors during hand movements without object interaction. The minimal resistance changes across most channels demonstrate the robustness and reliability of the sensors in dynamic conditions, ensuring accurate performance of the tactile glove in real-world applications.

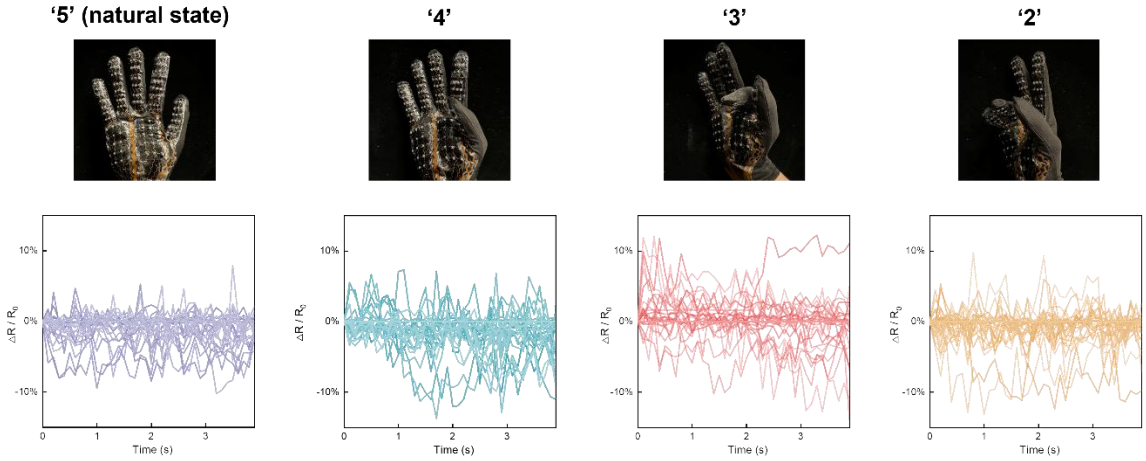

Figure 5.9 stability test of glove bending test. The signals changes within 4 seconds under 4 different postures are presented (containing 'five', which is a natural posture, 'four', 'three', and 'two').

In addition to surface modification, an encapsulation method was employed to enhance sensor stability. As the FPC is embedded inside two layers of TPU and adhered by Waterborne PU, there are two kinds of interfaces of the pressure sensors including PU/WPU/PU and PU/WPU/PI. According to the processes of encapsulation, five shear strength testing samples were fabricated to measure the package stability, including 1. PU+PI+WPU adhered under 120°C using hot-press (0.1 MPa); 2. PU + PU + WPU adhered under 80°C; 3. PU + PI + WPU adhered under 80°C; 4. PU + PU adhered under 80°C; 5. PU + PI + WPU adhered under room temperature. The schematic preparation of shear

strength testing is shown in Figure 5.10a. Each adhesion layer is fixed within a rectangular area of width W and length L. Layer 1 and Layer 2 in Figure 5.10b were further adhered on metal sheets using Cyanoacrylate Adhesive Super Glue 502 to prevent slip when MTS testing. Two different layers are stretched in opposite directions. This testing setup allows for the measurement of package stability by evaluating the shear strength of the adhesive bonds under various conditions[2]. The results provide insight into the optimal encapsulation methods for ensuring long-term durability and performance of the pressure sensors.

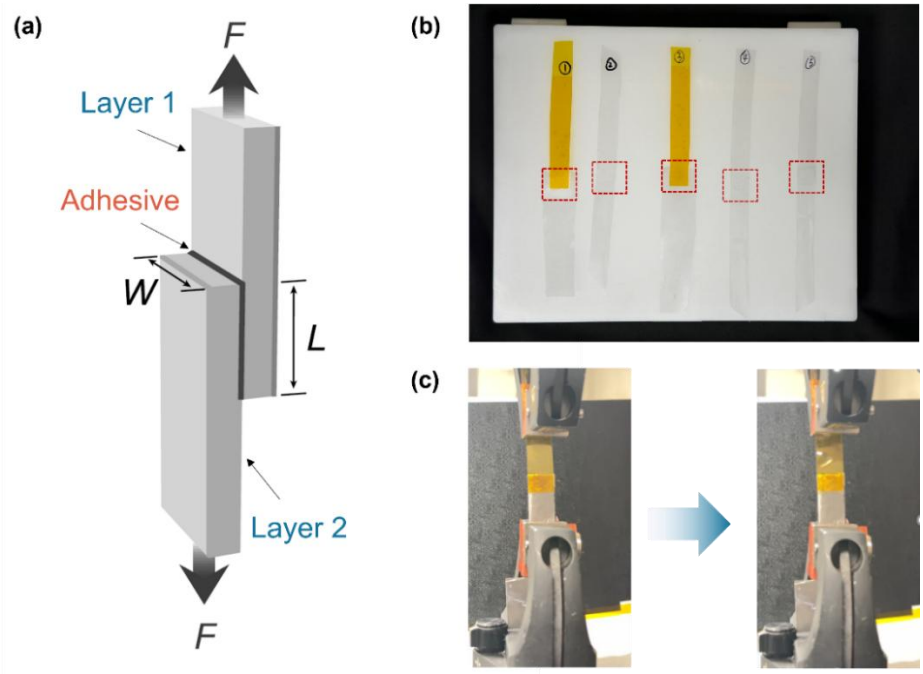

Figure 5.10 Shear strength test. (a) Setups for mechanical testing of adhesion performance. (b) Five testing samples. 1. PU + PI + WPU adhered under 120°C using hot-press (0.1 MPa); 2. PU + PU + WPU adhered under 80°C; 3. PU + PI + WPU adhered under 80°C; 4. PU + PU adhered under 80°C. 5. PU + PI + WPU adhered under room temperature. (c) The moment of stretch failure under MTS testing.

Using the setup for mechanical testing of adhesion performance, the prepared samples were tested at a strain rate of 50 mm/min. The force-displacement curves for the samples are shown in Figure 5.11a. All samples exhibited an immediate break point under the applied strain. Shear strength was defined as the maximum force at the break point divided by the adhesion area ($W \times L$). The shear strengths of samples 1 and sample 2 were notably high,

measuring 370 kPa and 500 kPa, respectively. In contrast, the shear strength of sample ○4 was significantly lower, at only 118 kPa.

These results indicate excellent adhesion performance for both sample 1 and sample 2, which utilized waterborne PU as the adhesive layer. The process of hot-pressing and heating likely contributed to this enhanced adhesion by volatilizing the solvent in the waterborne PU/ethanol solution. Additionally, the similar surface energy between PI and PU facilitates the formation of a stable bond. These findings underscore the effectiveness of using waterborne PU in conjunction with hot-pressing and heating to achieve strong and durable adhesion in the pressure sensors. This method not only improves the mechanical stability of the sensors but also ensures their reliability and longevity in practical applications.

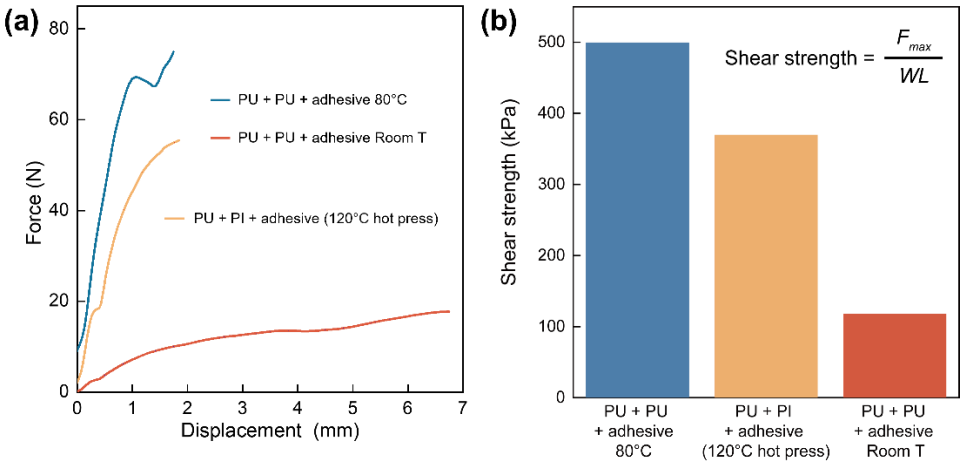

Figure 5.11 Mechanical testing of adhesion performance. (a) Stretching force changes with the displacement of three samples, including 1. PU + PI + WPU adhered under 120°C using hot-press (0.1 MPa). 2. PU + PU + WPU adhered under 80°C. 4. PU + PU adhered under 80°C. (b) Sheer strength comparison of the samples.

To estimate the stability improvement of the pressure sensors, the mechanical response of single pressure sensors was tested using a laboratory-made pressure testing platform, as shown in Figure 5.12a. Cyclic pressure testing was conducted to compare sensors with and without surface modification. The results indicate that sensors with surface modification

exhibit more stable initial resistance as the pressure returns to the initial level, even after numerous pressure cycles. The resistance change-pressure curve for a single cycle demonstrates consistent resistance changes, showing that the resistance reliably returns to the pre-pressure levels. The response and recovery resistance change curves are illustrated in Figure 5.12f. The response time and recovery time are both under 89 milliseconds, corresponding to the time interval setting of the Keithley 2450 source meter, which was configured to 89 milliseconds. For subsequent testing with the glove set, the time interval is set to 100 milliseconds. This rapid response and recovery time are crucial for ensuring reliable signal detection, which is essential for the object classification task. Furthermore, the fast response and recovery times contribute to minimizing latency in the data acquisition process, allowing for smoother and more precise control in dynamic environments. These findings highlight the effectiveness of surface modification in enhancing the stability and reliability of the pressure sensors, ensuring accurate and repeatable performance under cyclic loading conditions.

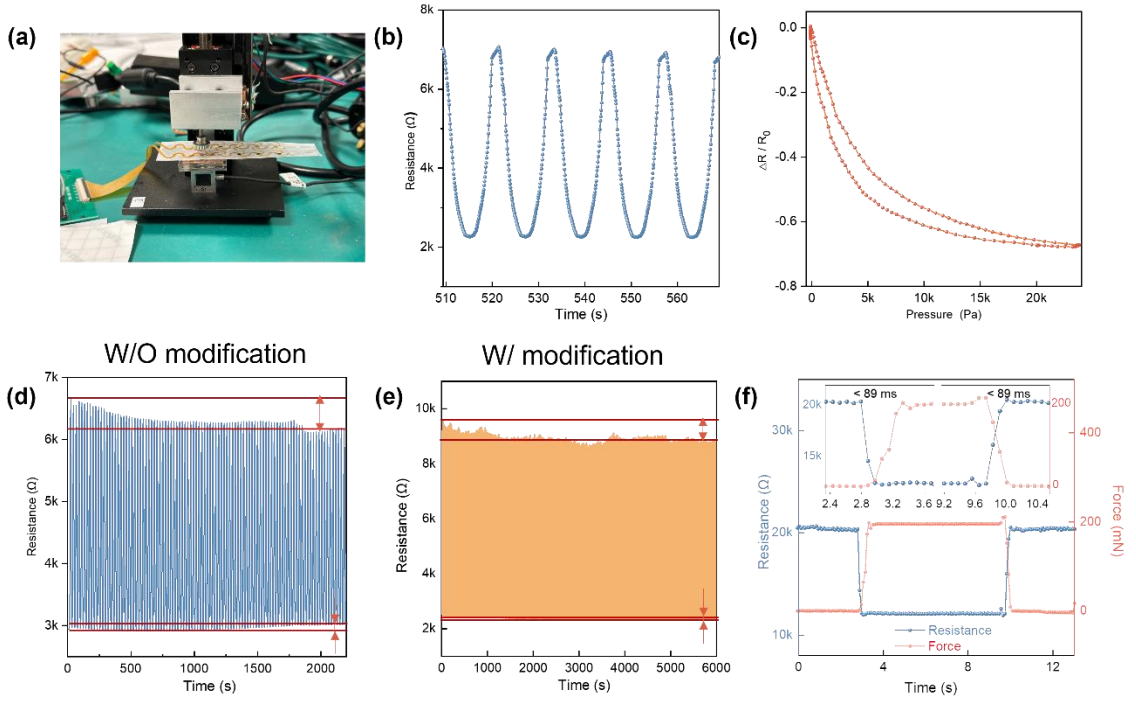

Figure 5.12 Cyclic mechanical test of the stability-enhanced pressure sensor. (a) Picture of a laboratory-made pressure testing platform. (b) Four cycles of pressure testing. All cycles are processed under moving speed of 35 μm/s, (c) Resistance change with pressure. (d) 100 cycles of contrast pressure sensors without surface modification. (e) 300 cycles of

contrast pressure sensors with surface modification. (f) The response times of stability-enhanced pressure sensor.

When acquiring signals from the 142 channels of the hand-like tactile gloves, a shorter time interval ensures the extraction of more detailed information. However, designing the multimodal signal reading circuits introduces the possibility of crosstalk effects, which may compromise the accuracy of the readout. To better understand the crosstalk effect, Figure 5.13a illustrates a scenario where a path composed of three resistances—Rim, Rsm, and Rsj—in parallel to Rij, alters the measured value[3]. Drawing inspiration from the grounding-based array readout design, in which each row is driven by a constant voltage source Vi through independent buffers, the trans-resistance amplifiers' inputs act as a virtual ground. This design ensures that columns not currently active are grounded, minimizing interference. A Bluetooth acquisition circuit design for the hand-like tactile gloves was introduced, featuring time-division multiplexers that read the currents of each row in a sweeping mode.

In this design, a potential difference as close to zero as possible is imposed across the elements not being read, preventing crosstalk between sensors. This approach is critical for maintaining the integrity of the signal acquisition process, ensuring that each sensor's data is accurately captured without interference from neighboring sensors. By implementing such measures, the tactile gloves can deliver precise and reliable tactile feedback, which is essential for applications such as robotic manipulation, prosthetics, and advanced human-machine interfaces. This design ensures that the system can handle the high data throughput required for real-time signal processing and interpretation, making it a robust solution for complex tactile sensing tasks.

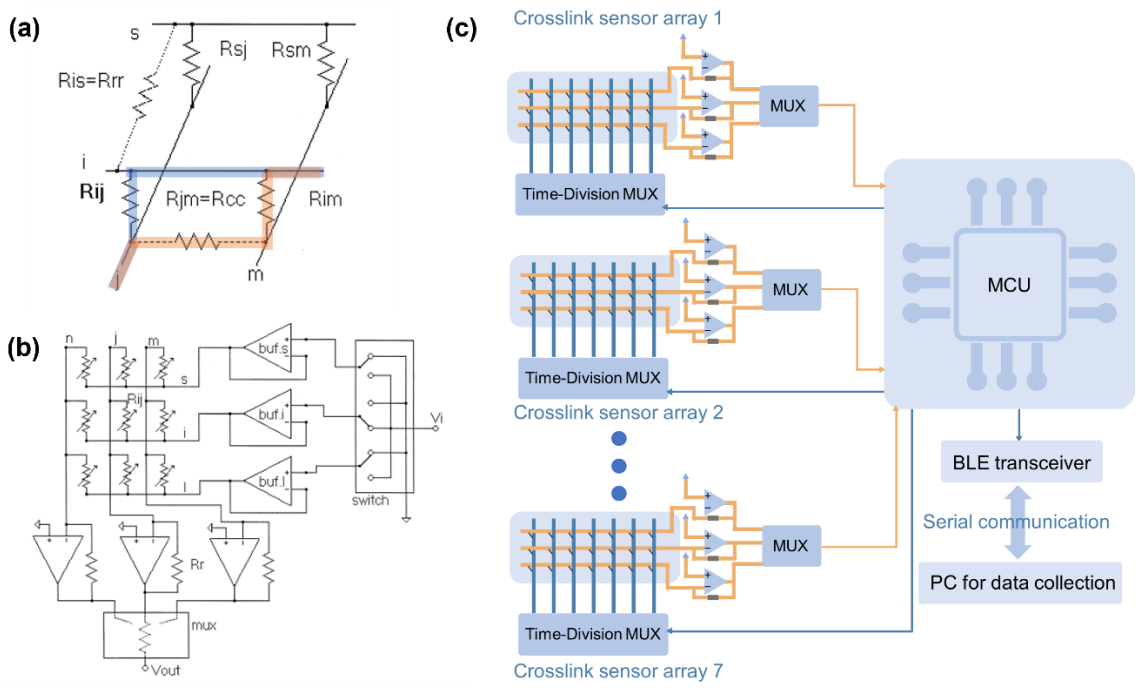

Figure 5.13 Data acquisition designs of hand-like tactile gloves. (a) The schematic crosstalk effect in traditional arrays of piezoresistive sensors. (b) Circuit based on grounding design for sensor arrays data acquisition against crosstalk. (c) The Bluetooth data acquisition circuit design of hand-like tactile gloves contains time-division multiplexers with 10 Hz data reading rate for 142 channels. Reproduced with permission from ref.[3]. Copyright 1999 Elsevier.

This hardboard PCB is equipped with Bluetooth transmission capabilities and a USB interface. The Bluetooth functionality allows for wireless data transfer, enabling seamless connectivity with various devices and enhancing the system's versatility. The USB interface provides an additional option for wired connections, ensuring compatibility with a wide range of data acquisition setups. The robust construction of the hardboard PCB ensures durability and reliable performance across different environments, making it suitable for both stationary and mobile applications. The flexible PCB is designed for applications requiring high mobility and power efficiency. It is connected to a 3000 mAh lithium battery, which provides extended operational time. This configuration is ideal for wearable and portable data acquisition systems, where the flexibility and lightweight nature of the FPCB are crucial.

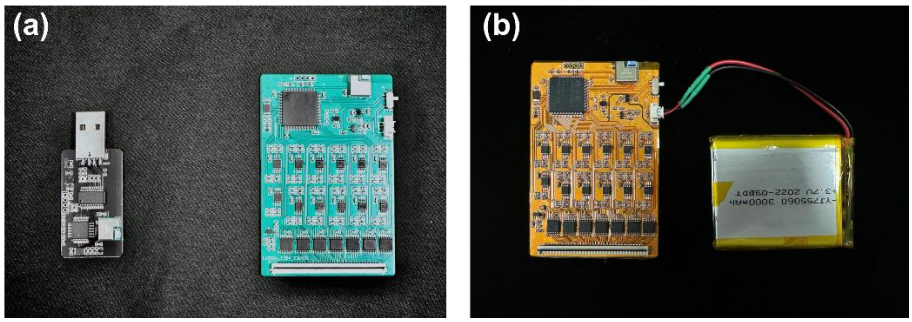

Figure 5.14 PCB & Flexible PCB for data acquisition systems. (a) Hardboard PCB with Bluetooth transmission USB interface. (b) Flexible PCB connected with 3000 mA·h Lithium battery.

Figure 5.15a displays the tactile glove along with the corresponding serial port channel numbers. To facilitate data acquisition, a user-friendly interface (UI) has been developed for easy data readout and storage. This UI application offers two distinct modes: profile mode and thermal mode. Profile Mode: In profile mode, sensor resistance changes are visualized using a color gradient. Red indicates low resistance, while green represents high resistance. This visual representation allows users to quickly interpret sensor data and understand the distribution of resistance changes across the glove. Thermal Mode: Thermal mode presents the resistance changes in the form of a heatmap. This mode provides a comprehensive view of the sensor data, highlighting areas of varying resistance with different colors, similar to a thermal image. This can be particularly useful for identifying patterns and anomalies in sensor readings.

In addition to these visualization modes, the UI also includes an automatic sensor calibration feature. This function ensures that the sensors are properly calibrated before data collection begins, enhancing the accuracy and reliability of the data. The calibration process adjusts the sensors to their optimal operating conditions, compensating for any drift or variability in sensor performance. By integrating these features, the UI provides a powerful tool for users to interact with the tactile glove data acquisition system. It simplifies the process of monitoring and analyzing sensor data, making it accessible to users with varying levels of technical expertise. This comprehensive interface enhances the functionality of the tactile glove, making it suitable for a wide range of applications, from

research and development to practical, real-world use cases.

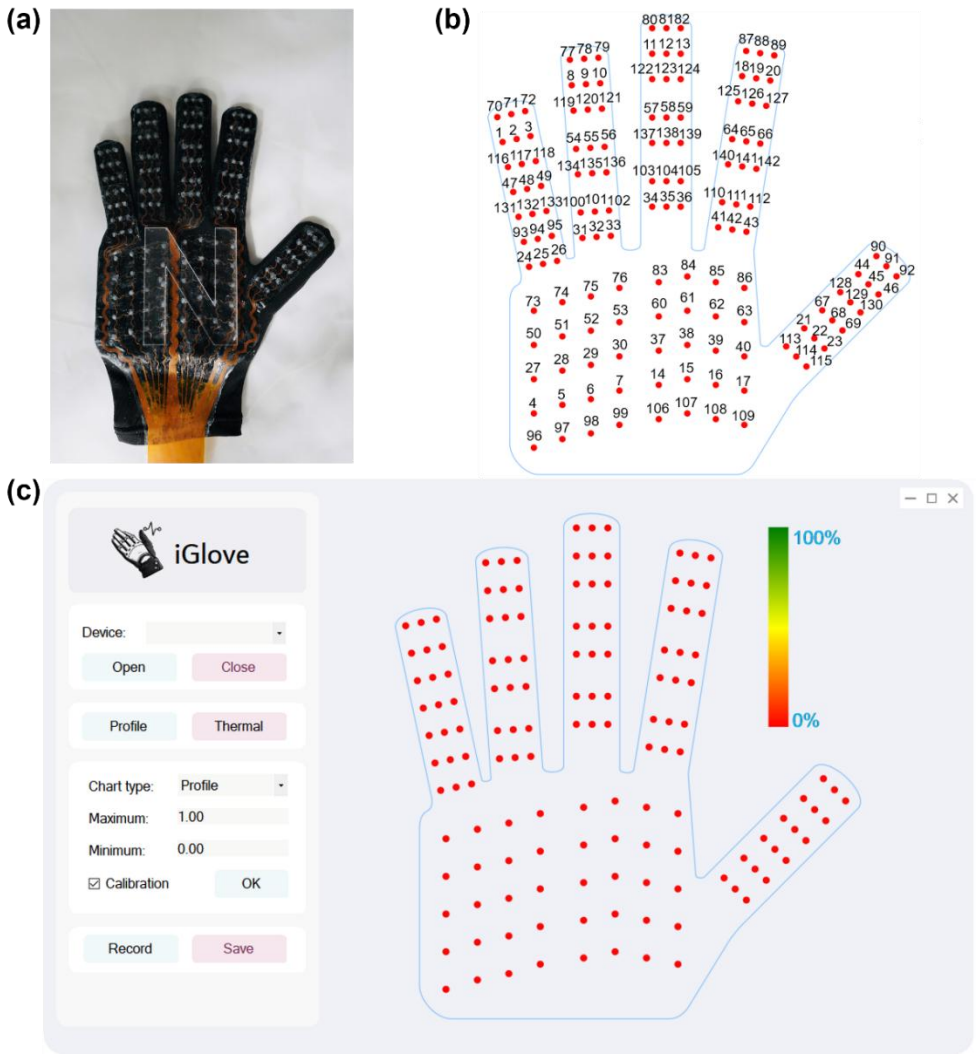

Figure 5.15 The stability-enhanced tactile gloves and the array signals User-Interface (UI). (a) Picture of the tactile glove. (b) The distribution of sensors on the palm and the corresponding serial port channel numbers. (c) Data-visualized UI of the tactile glove.

With the data-visualized user interface (UI) of the tactile gloves, the force distribution when interacting with different objects can be clearly observed. In this study, acrylic sheets were cut into various shapes using a laser cutter. Specifically, acrylic sheets in the shapes of the letters 'N', 'T', and 'U' were created using a UNIVERSAL laser cutter PLS6.150D with a 150W power output. The schematic figures illustrate the positions of these word-shaped acrylic sheets. When these shapes were placed under the tactile glove's sensors, different sensors responded according to the specific locations and shapes of the sheets. This

correlation between sensor responses and the positions of the acrylic shapes demonstrates the reliability and accuracy of the tactile glove system.

The different shapes of the acrylic sheets induce varying pressure distributions, which are captured and displayed in real-time by the tactile glove's sensors. The sensors' ability to detect and accurately represent these force distributions validates the effectiveness of the system in practical applications. By using these specific shapes, we were able to test the glove's sensitivity and precision in detecting distinct force patterns. This experimental setup highlights the glove's potential for a wide range of applications, including robotic manipulation, tactile sensing in prosthetics, and human-computer interaction. The reliable data visualization provided by the UI enhances the usability of the tactile glove, making it a valuable tool for researchers and practitioners who require precise and detailed feedback on force distribution during object interactions.

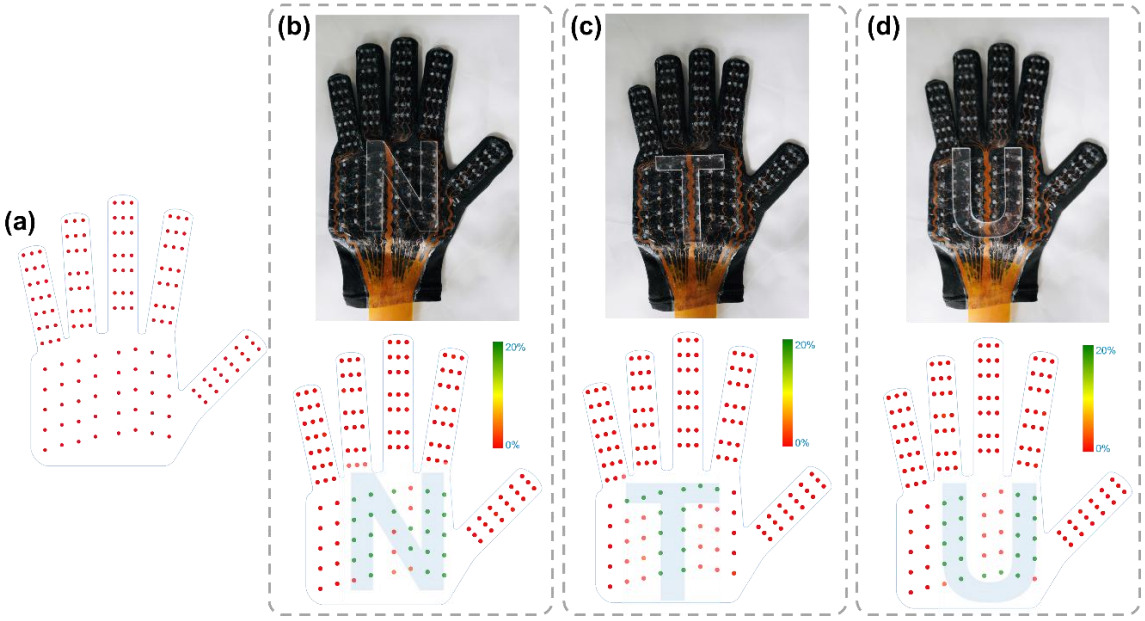

Figure 5.16 Force distribution analysis of tactile gloves. (a) Initial state of force detection UI. (b) New state when ‘N’ word-shape acrylic sheet placing on tactile glove. (c) New state when ‘T’ word-shape acrylic sheet placing on tactile glove. (d) New state when ‘U’ word-shape acrylic sheet placing on tactile glove.

5.3.2 Palpation-related diagnosis classification task using tactile sensing gloves

Here is a picture of the tactile glove wearing on tester's hand. The FPC's end was connected to the customized flexible PCB. The flexible PCB was powered by lithium battery for Bluetooth transmission. A feature extraction example is shown in Figure 5.17b. Since applied force will lower the resistance of pressure sensor, a complete signal curve contains baseline and a downward peak. Two features including amplitude and time are selected for further machine learning. The amplitude refers to maximum change of the signal and time refers to full width at 85% maximum value.

Figure 5.17a presents an image of the tactile glove worn on the tester's hand. The end of the FPC is connected to a customized flexible PCB, which is powered by a lithium battery to enable Bluetooth transmission. This setup allows for wireless data collection and real-time monitoring of the glove's sensor outputs. An example of feature extraction is illustrated in Figure 5.17b. When a force is applied to the pressure sensors, the resistance decreases, resulting in a characteristic signal curve that includes a baseline and a downward peak. From this signal curve, two key features are extracted for further machine learning analysis: 1. Amplitude: this feature represents the maximum change in the signal, indicating the magnitude of the applied force. It is measured as the difference between the baseline and the lowest point of the peak. 2. Time: this feature refers to the full width at 85% of the maximum value of the peak. It captures the duration of the force application, providing information about the temporal characteristics of the interaction.

These features are critical for accurately characterizing the sensor responses and are used as input variables for machine learning algorithms. By analyzing the amplitude and time features, the system can learn to recognize different force patterns and improve the accuracy of object classification and other tasks.

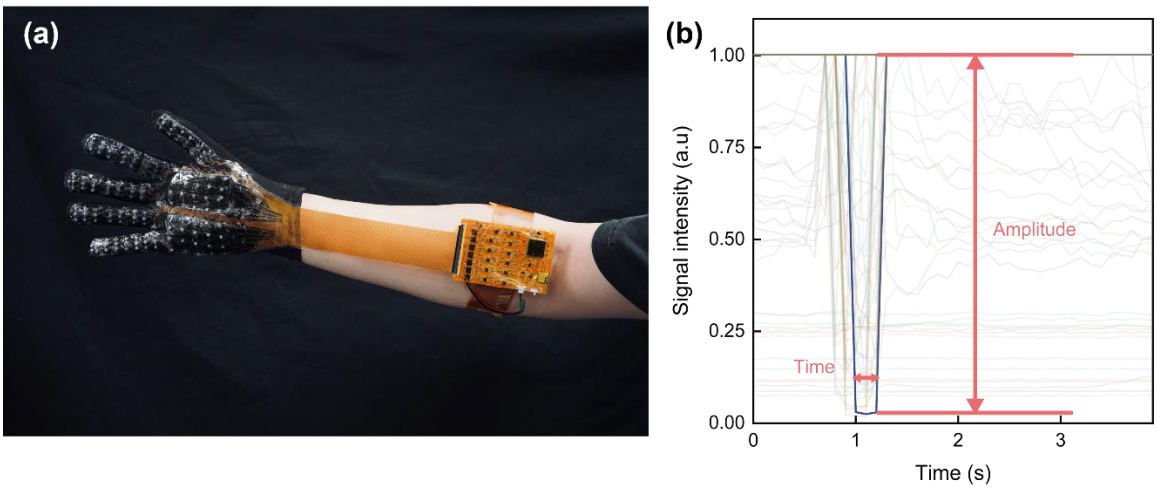

Figure 5.17 Structure and feature extraction for machine learning (a) A photo showing the tactile glove consisting of 142 pressure sensing channels and the customized flexible PCB are worn on the forearm. (b) Feature extraction of the 142 channels.

For the purpose of healthcare-related object classification, two medical breast models made from silicone gel were selected for data collection. Figure 5.18a and 5.18b depict the tactile gloves interacting with these breast models. In the healthy breast model, there are no hard parts representing medical nodules, providing a baseline for comparison. In contrast, the abnormal breast model contains three types of simulated nodules, each representing different medical conditions, which are designed to mimic the higher young's modulus of pathological tissues. The three types of simulated nodules in the abnormal breast model are as follows:

Fibrocystic Change: These nodules have blurred edges, making them less distinct from the surrounding tissue. This condition often presents with a diffuse texture that is challenging to delineate.

Tumor (Cancer): Tumorous nodules are characterized by clear edges, making them distinct and easier to identify. These nodules typically represent malignant growths and have a significantly higher stiffness compared to normal tissue.

Plugged Duct: This condition is simulated by hard nodules located around the nipple area.

These nodules are indicative of blockages in the milk ducts and present a localized increase in tissue stiffness.

Each of these nodules has a much higher Young's modulus than the surrounding silicone gel, allowing the tactile gloves to detect variations in stiffness and texture. The gloves capture these differences through their sensors, providing data that can be used for object classification. By analyzing the data collected from interactions with these breast models, the tactile glove system can help in distinguishing between healthy and abnormal tissues. The ability to identify different types of nodules based on their tactile properties can contribute to more accurate and early diagnosis of breast conditions. This approach demonstrates the potential of tactile gloves in medical applications, offering a non-invasive method to assess tissue properties and detect abnormalities.

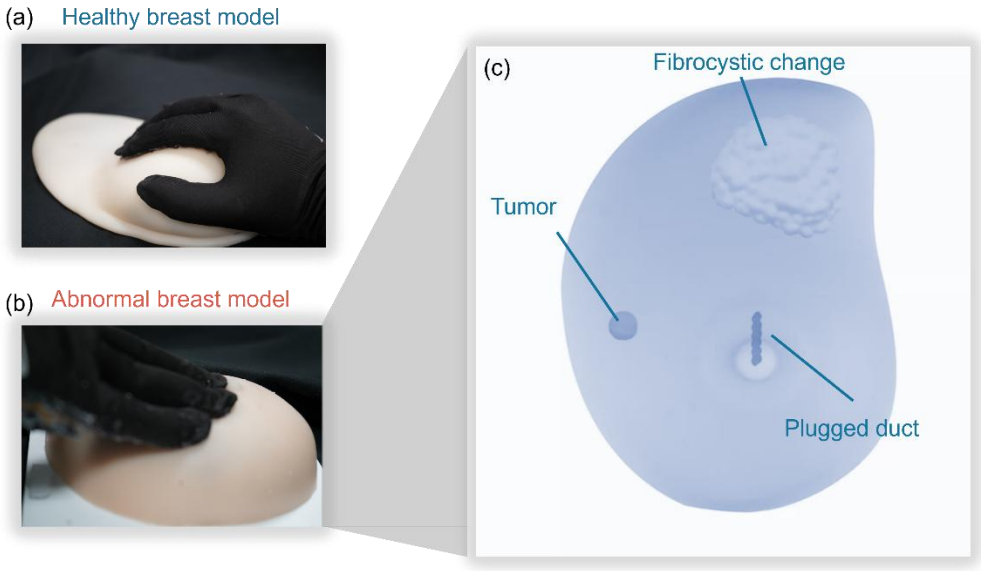

Figure 5.18 Medical breast model and distribution of the simulated nodules. (a) Healthy breast model. (b) Abnormal breast model. (c) Distribution of three different simulated nodules of the abnormal breast model, including tumor, fibrocystic change, and plugged duct.

Figure 5.19 presents the results of a comprehensive classification task involving 12 different object types. The 12 object types included in the dataset are categorized as follows: medical model (healthy breast, tumor, fibrocystic change, and plugged duct) and 8 types

of geometric solids (small foam ball, medium foam ball, big foam ball, small sponge ball, cube, cylinder, cone, and cuboid). To ensure accurate prediction with a medium-sized dataset, K-fold cross-validation was applied for a total of 2487 samples. Specifically, approximately 40 samples from each of the 12 classification targets were selected to form a testing set of 487 samples. The remaining 2000 samples were used for training and validation. For a 10-fold cross-validation approach (k=10), each fold contained 200 samples. Training was repeated 10 times, with nine folds used for training and one fold for validation in each iteration. The model with the best performance across the cross-validation process was then retrained using all 2000 samples. Finally, this optimized model was used to predict the 487 testing samples.

The feature extraction results, as depicted in Figure 5.19, clearly show distinct differences between the various object types. Within each type, the features exhibit consistency across different samples, indicating reliable sensor readings and robust data collection. The successful extraction and utilization of these features underscore the potential of the tactile glove system for sophisticated data analysis and machine learning applications. By accurately distinguishing between different object types, including both medical models and geometric solids, the system demonstrates its capability for nuanced tactile sensing.

The tactile glove system's ability to consistently capture and analyze tactile data positions it as a valuable tool for a wide range of applications, from medical diagnostics to robotic manipulation and beyond. The integration of advanced machine learning algorithms with high-fidelity sensor data from the tactile gloves opens new possibilities for real-time, accurate classification tasks. This technology holds promise for improving the effectiveness of tactile sensing devices and expanding their use in various sectors, ultimately contributing to the development of more intelligent and responsive systems.

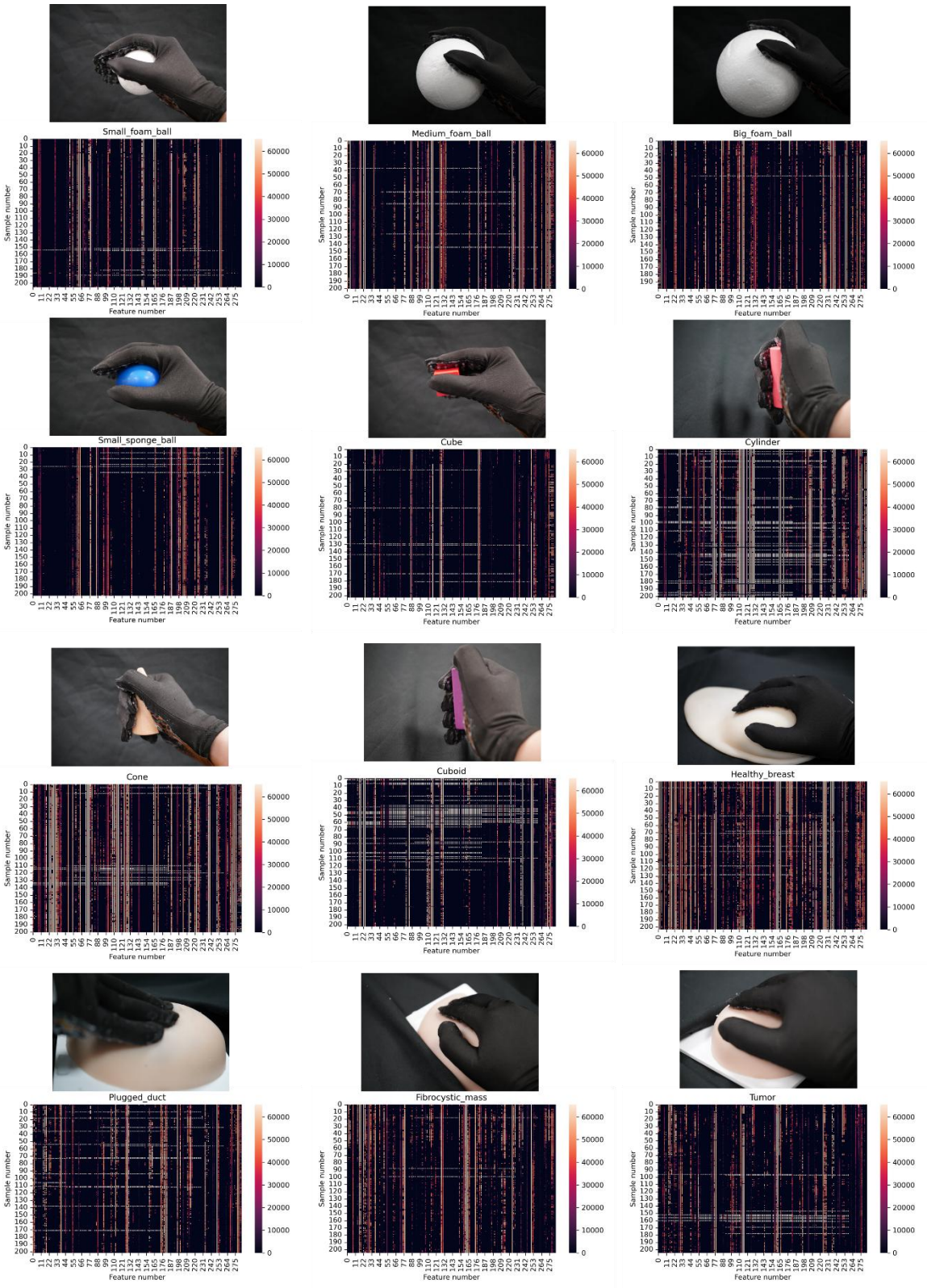

Figure 5.19 Classification task involving 12 different object types and feature extraction

results.

From the feature extraction results, three foam balls of different diameters—small (7 cm), medium (9 cm), and large (12 cm) are extracted for quantification analysis. As each ball was grasped 200 times, resulting in a total of 600 data samples. The analysis of the activated sensors for each grasp revealed a clear trend: as the size of the ball increased, the number of activated sensors also increased (Figure 5.20). This observation supports the theoretical premise that the tactile glove's size resolution capability is proportional to the object's size. Specifically, larger objects activate more sensors, enhancing the glove's ability to accurately discern size variations. These findings provide valuable evidence for the design and application of tactile gloves in tasks requiring precise size discrimination, such as medical diagnostics and robotic manipulation. The positive correlation between object size and the number of activated sensors underscores the importance of optimizing sensor arrays to improve the performance and accuracy of tactile sensing systems.

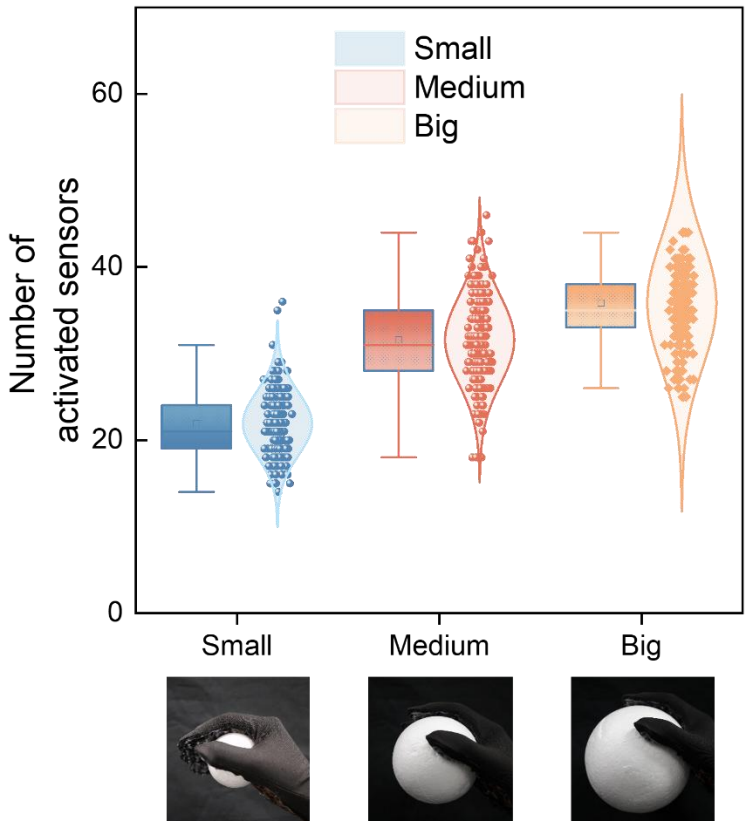

Figure 5.20 Number of activated sensors on tactile glove systems changing with ball size (Diameter of small foam ball: 7 cm; medium foam ball: 9 cm; big foam ball: 12 cm)

Figure 5.21 illustrates the feature correlations identified using the SVM method. As shown in Figure 5.21a, features 11 and 88 were selected to demonstrate the limited correlations between different features. This indicates that the chosen features provide distinct and non-redundant information, which is crucial for accurate classification. The PCA results further support this finding by showing that the 12 types of samples can be easily distinguished into different groups. The PCA visualization demonstrates that the 12 types of grasp tasks can be clearly differentiated, even among similar items. Specifically: 1. Small, medium, and large sponge balls; 2. Small foam and small sponge balls. 3. Cuboid and cylinder.

The test set, consisting of 487 samples, achieved an impressive accuracy of 99.18%. This high recognition accuracy underscores the system's capability to accurately distinguish between different objects based on their shapes and softness. The ability to distinguish between different types of objects, particularly those with subtle differences, showcases the potential of this tactile glove system in various applications. For instance, in the medical field, the system's high accuracy in recognizing different objects can translate to distinguishing symptoms based on the shape and softness of tissues. This could greatly enhance diagnostic processes, enabling more precise and reliable identification of medical conditions.

Overall, the successful application of SVM and PCA in this context highlights the advanced capabilities of the tactile glove system for sophisticated data analysis and machine learning. The high accuracy and distinct feature correlations demonstrate the system's effectiveness in tactile sensing and its potential for further advancements in interactive and diagnostic technologies.

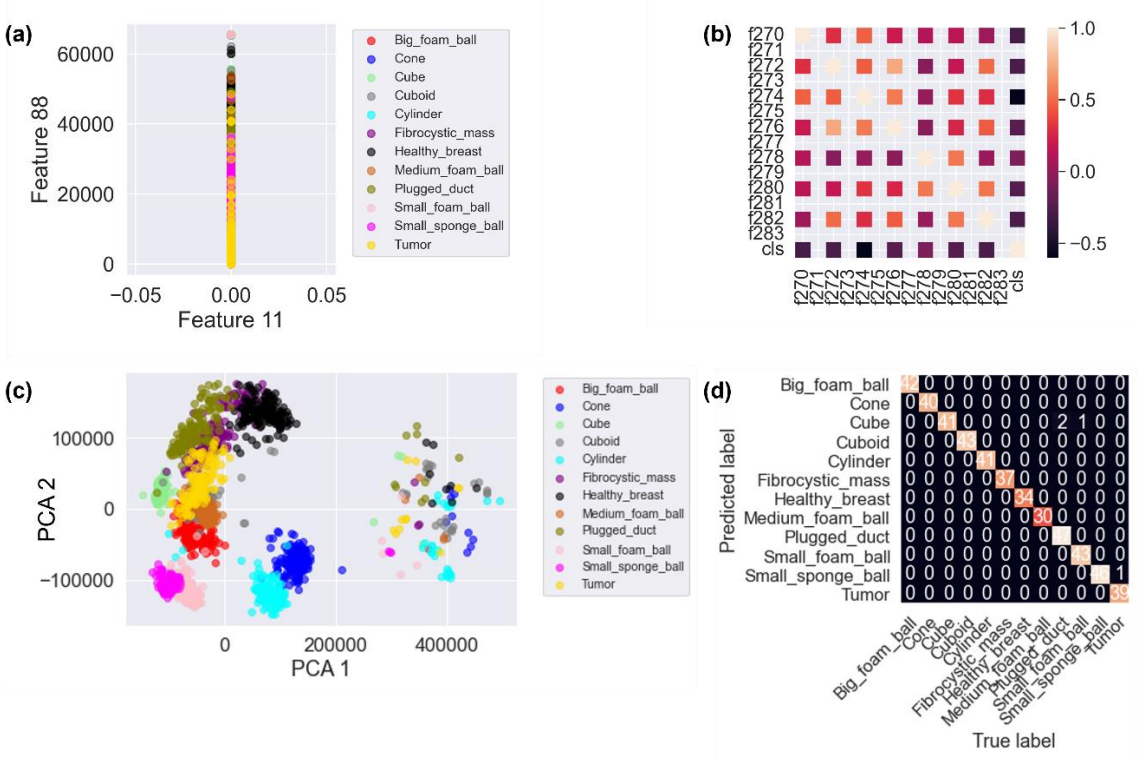

Figure 5.21 Feature correlations and classification accuracy using SVM (a) Two features correlation. (b) Several feature correlations. (c) PCA of the 12-types classification task. (d) Machine learning test result.

The impact of sensor density on classification accuracy was systematically investigated using a 142-channel tactile glove. Various numbers of pressure sensors were activated to create different sensor densities. The activation levels tested were 1, 6, 20, 46, 68, 96, and the full 142 sensors. The results are illustrated in the accompanying figure 5.22, which depicts the accuracy of the tactile glove in performing classification tasks involving 3 classes and 12 classes at each sensor density. The data clearly demonstrate a positive correlation between sensor density and classification accuracy. Higher sensor densities consistently resulted in improved accuracy, underscoring the importance of sensor density in enhancing the performance of tactile sensing systems. This finding highlights the potential for optimizing sensor arrays to achieve superior classification outcomes in various applications, including medical diagnostics and robotic manipulation.

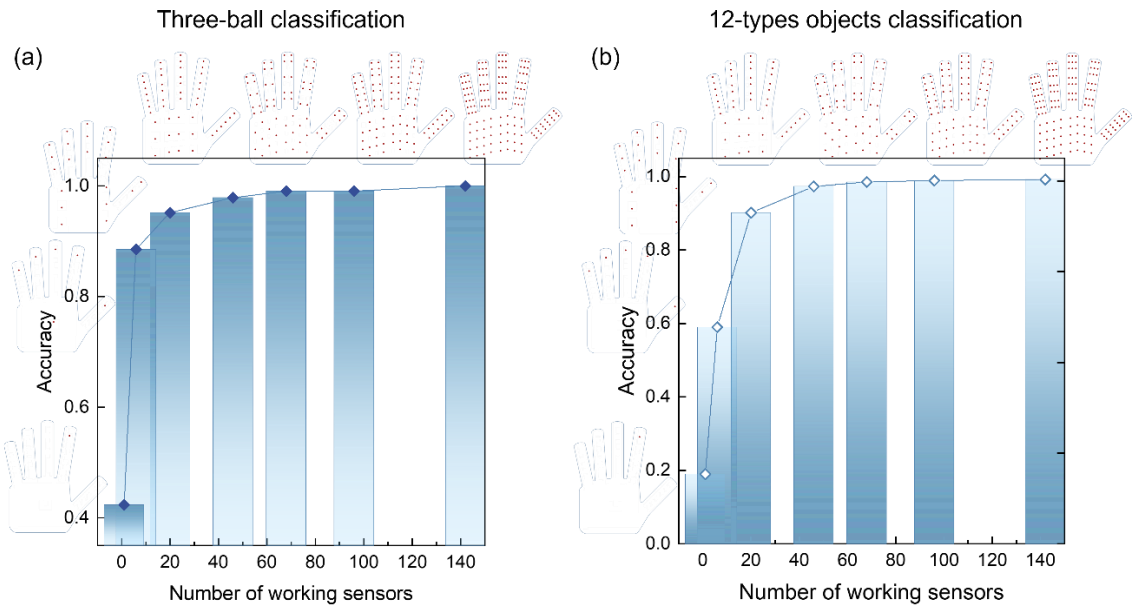

Figure 5.22 The effect of sensor density on classification accuracy (a) Three-class accuracy curve. (b) Full-class accuracy curve.

5.4 Conclusion

In this chapter, we explored significant advancements in the development and application of tactile sensing systems, particularly focusing on medical diagnostics and healthcare applications. First, we demonstrated that pressure sensors exhibit improved stability when subjected to surface modification and encapsulation techniques. These enhancements protect the sensors from environmental factors and mechanical wear, ensuring reliable and consistent performance over time. Second, our clinical classification tasks involving 12 distinct classes showcased the high accuracy of the tactile sensing gloves, achieving an impressive 99.18%. This result underscores the potential of these gloves in accurately distinguishing various physical properties, which is crucial for precise diagnostic applications in healthcare. Third, we discussed the potential of the tactile sensing systems in more sophisticated healthcare scenarios, particularly in size and shape classification tasks. The system's ability to accurately classify different sizes and shapes demonstrates its utility in assessing complex tissue properties and abnormalities, offering non-invasive diagnostic solutions. Lastly, we established a positive correlation between the size of the objects being sensed and the number of active sensors, as well as between classification

accuracy and the density of sensors. This finding suggests that increasing the number of sensors can enhance the system's resolution and accuracy, making it more effective in detailed and complex sensing tasks.

Overall, this chapter highlights the promise of tactile gloves in medical diagnostics, facilitated by the integration of advanced sensing technologies, machine learning algorithms, and real-time data visualization. The stability-enhanced tactile sensing system, combined with the glove's versatility and precision, marks a significant advancement in developing intelligent and interactive healthcare tools.

References

[1] Cui Z, Wang W, Xia H, Wang C, Tu J, Ji S, Tan JMR, Liu Z, Zhang F, Li W, Lv Z, Li Z, Guo W, Koh NY, Ng KB, Feng X, Zheng Y and Chen X. *Advanced Materials.* **2022**, 34, 2207016.

[2] Yuk H, Varela CE, Nabzdyk CS, Mao X, Padera RF, Roche ET and Zhao X. *Nature.* **2019**, 575, 169.

[3] D'alessio T. *Sensors and Actuators A: Physical.* **1999**, 72, 71.

Chapter 6

Conclusions and Recommendations

This chapter summarizes the research findings on advanced tactile sensing technologies. Two hypotheses were tested: (1) Dynamic force sensing for in-situ measurement of micro-scale surface profile and (2) Tactile system for in-situ quantifying object features. Results confirmed that piezoelectric sensors accurately sense textures regardless of speed, and pressure-sensing gloves with 142 sensors achieved 99.18% accuracy in distinguishing stimuli. The research introduces a piezoelectric tactile sensor for in-situ quantifying object textures and outlines future work on integrating the sensors with robotic systems for real-time surface analysis. Additionally, it proposes a ChatGPT-based interactive diagnostic glove to enhance patient interaction and diagnostic precision. Future studies will focus on refining these technologies for broader industrial and medical applications.

6.1 Discussion and conclusion

6.1.1 Testing hypotheses

The two hypotheses proposed previously include:

Hypothesis 1: Dynamic force sensing for in-situ measurement of micro-scale surface profile

The hypothesis posits that piezoelectric tactile sensor can effectively characterize textures through dynamic force sensing, and thus realize quantitative texture sensing. The use of two vibration sensors, calibrated for speed, is proposed to ensure accurate texture characterization without requiring machine-controlled systems to maintain a steady speed. This approach suggests that the sensors' ability to capture variations in vibration frequency and amplitude, induced by different textures, can provide detailed information about the surface properties. The hypothesis implies that the system can operate under variable speed conditions, offering a more flexible and practical solution for real-world applications.

Hypothesis 2: Tactile system for in-situ quantifying object features

This hypothesis suggests that gloves equipped with a pressure sensing array can facilitate quantitative sensing, with potential applications in various fields, including medical diagnostics. The relationship between the size of an object and the number of activated sensors is hypothesized to be proportional, meaning larger objects would trigger more sensors. Additionally, the accuracy of the sensing system is hypothesized to be directly related to the precision and density of the sensors. A higher density of sensors is expected to provide more detailed and accurate data, enhancing the glove's capability to quantify different characteristics, such as size, shape, and surface properties. The hypothesis further suggests that such gloves could significantly impact medical diagnostics, enabling precise measurement of tissue properties and abnormalities through non-invasive means, thus offering great potential for advancements in healthcare technology.

6.1.2 Major findings

The major findings of the thesis are summarized below:

1. A novel tool designed to distinguish and calculate two-dimensional information of grating textures. This device provides a sensitive and accurate method for sensing fine textures by detecting variations in force at the fingertip. One of the significant findings is the speed-independence response of the piezoelectric tactile sensor, which allows it to deliver consistent results regardless of the scanning speed over the textured surface. This characteristic is particularly valuable in practical applications where consistent speed control may be challenging.

2. The piezoelectric tactile sensor is capable of grating-texture sensing without the need for controlled systems. This approach simplifies the sensing process, making it more accessible and practical for various applications, including robotics and tactile feedback systems. The research further explores the capability of the piezoelectric tactile sensor to achieve three-dimensional pattern imaging. By employing a sweeping test, the piezoelectric tactile sensor can capture detailed 3D representations of textured surfaces, offering a comprehensive understanding of the surface characteristics.

3. The enhanced stability of pressure sensors through surface modification and encapsulation techniques, which protect the sensors from environmental factors and mechanical wear, ensuring consistent performance over time. A novel tactile glove design featuring 142 crosslink-designed pressure sensors was fabricated, providing comprehensive and precise detection of pressure distributions. This configuration significantly improves the glove's sensitivity and accuracy.

4. In classification tasks involving 12 different classes, the tactile glove achieved an outstanding accuracy of 99.18%, underscoring its capability to distinguish between

various stimuli with minimal error. This high level of precision indicates the glove's potential for sophisticated applications, particularly in healthcare scenarios where accurate detection and classification of physical properties are crucial. The research also revealed a positive correlation between the size of objects being sensed and the number of active sensors, with larger objects activating more sensors, thus capturing more detailed information. Additionally, a direct correlation was observed between sensor density and classification accuracy, suggesting that increasing the number of sensors could further enhance performance.

6.1.3 Implication of current work

The research presented showcases significant advancements in tactile sensing technology, with particular emphasis on quantitative texture sensing and the development and integration of pressure sensors into tactile gloves. The key findings have several critical implications:

1. Innovative texture sensing technology: The development of the piezoelectric tactile sensor introduces a novel approach to texture sensing. The piezoelectric tactile sensor's ability to distinguish and calculate two-dimensional information of grating textures, coupled with its speed-independent response, provides a robust method for texture analysis. This capability is particularly useful in applications where consistent speed control is challenging, such as in manual inspection processes or robotic exploration.

2. Advanced 3D imaging capabilities: The piezoelectric tactile sensor's capability to achieve three-dimensional pattern imaging offers a comprehensive understanding of surface characteristics, which is invaluable in fields such as quality control and material science. This technology allows for detailed inspection and analysis of surface textures, which can be critical in industries where surface finish and texture are of utmost importance.

3. High-precision sensing in medical diagnostics: The novel design of the tactile glove, featuring 142 crosslink-designed pressure sensors, allows for comprehensive and

precise detection of pressure distributions. This configuration not only improves the glove's sensitivity but also significantly enhances its accuracy in detecting and differentiating various stimuli. The achievement of a 99.18% accuracy rate in classification tasks involving 12 different classes demonstrates the glove's potential for high-precision applications, such as in healthcare settings for detecting subtle changes in tissue properties or abnormalities.

6.2 Future work

6.2.1 Real-time in-situ workpiece topography characterization

One promising avenue for future research is the real-time in-situ characterization of workpiece topography using the piezoelectric tactile sensor integrated onto robotic arms or assembly lines. This application aims to provide immediate feedback on the surface quality of workpieces as they are being processed or assembled, which is crucial for maintaining high-quality standards in manufacturing.

The integration of piezoelectric tactile sensor technology onto robotic arms allows for continuous monitoring and characterization of workpiece surfaces. As the robotic arm moves across the workpiece, the piezoelectric tactile sensor can collect detailed surface data, including micro-scale patterns, roughness, and other topographical features. This capability is particularly valuable in industries such as semiconductor manufacturing, aerospace, and automotive, where surface precision and finish are critical.

The real-time in-situ characterization offers several advantages. From the aspect of quality Control, the piezoelectric tactile sensor systems can provide real-time feedback and enable immediate detection of surface defects or deviations from desired specifications. This allows for prompt corrective actions, reducing the likelihood of defective products reaching the next stages of production or the market. In turn, this can lead to significant cost savings by minimizing waste and rework[1].

With the ideal property of fast scanning speed and large-scale morphology characterization compared to atomic force microscopy and surface profiler, the piezoelectric tactile sensor's integration into robotic systems facilitates automation, allows for scalable deployment across multiple production lines. This technology can be customized to suit different types of workpieces and materials, making it a versatile tool for various manufacturing environments[2]. The ability to automate surface inspection also reduces the need for manual inspection, freeing up human resources for other tasks.

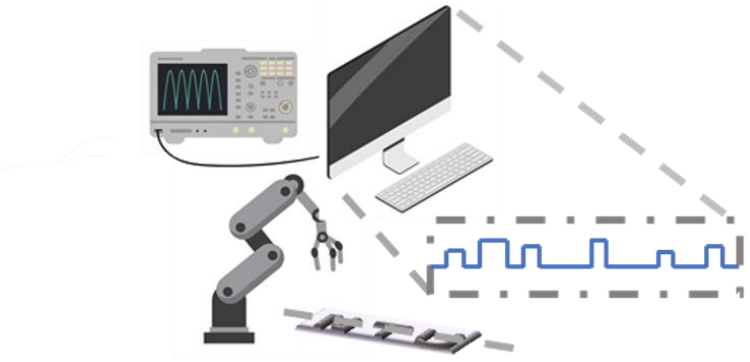

Figure 6.1 Schematic diagram of real-time in-situ workpiece topography characterization.

6.2.2 ChatGPT-based interactive diagnostics by tactile sensing gloves

In the realm of medical diagnostics, traditional methods such as inspection, listening, inquiry, and palpation are crucial[3-5]. To advance digital palpation in robotic diagnostic scenarios, it is essential to integrate these techniques seamlessly. The proposed tactile glove doctor represents a novel approach by combining an intelligent tactile glove with conversational AI (Figure 6.2c). This system leverages ChatGPT to enhance interactive diagnostics, making the process more interactive and effective. The Tactile Glove Doctor functions as a sophisticated diagnostic tool that not only performs palpation but also engages in dialogue with the patient to gather relevant information, thus enabling a more comprehensive assessment.

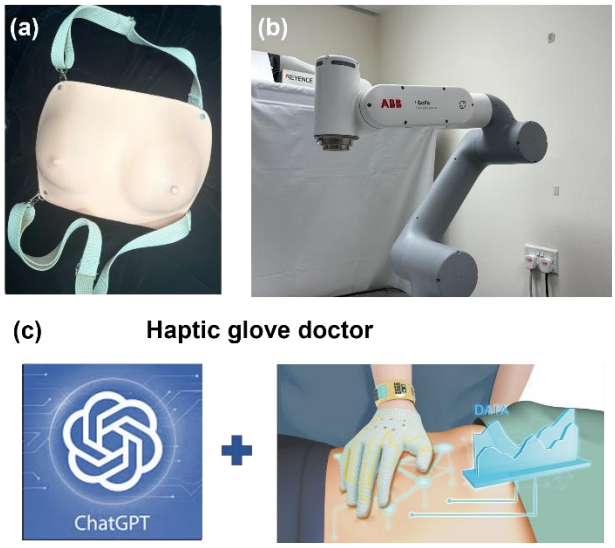

Figure 6.2 (a) Wearable breast modal with abnormal modals inside. (b) Robotic arms for integration of 142-channels tactile gloves. (c) Schematic diagram of tactile glove doctor.

The system is designed to be integrated with robotic arms, which are used to test a wearable breast examination model. These robotic arms are equipped with advanced sensors and actuators to accurately perform palpation based on real-time patient feedback. ChatGPT, embedded within the system, acts as a virtual assistant that guides the diagnostic process through conversational prompts. For example, it might ask, "What specific area would you like to examine?" or "Could you describe the symptoms you're experiencing?" Based on the patient's responses, the system employs voice recognition to interpret the answers and directs the robotic arms to the appropriate location for examination (shown in Figure 6.3).

This approach aims to enhance the accuracy and user experience of digital palpation by combining tactile feedback with patient interaction. Future work will focus on refining the voice recognition capabilities and improving the integration between the tactile glove and robotic arms. Additionally, exploring other medical applications and diagnostic scenarios will be crucial in expanding the system's capabilities. The ultimate goal is to create a versatile diagnostic tool that can offer both precise physical examination and responsive, patient-centered interaction, thereby advancing the field of non-invasive medical diagnostics.

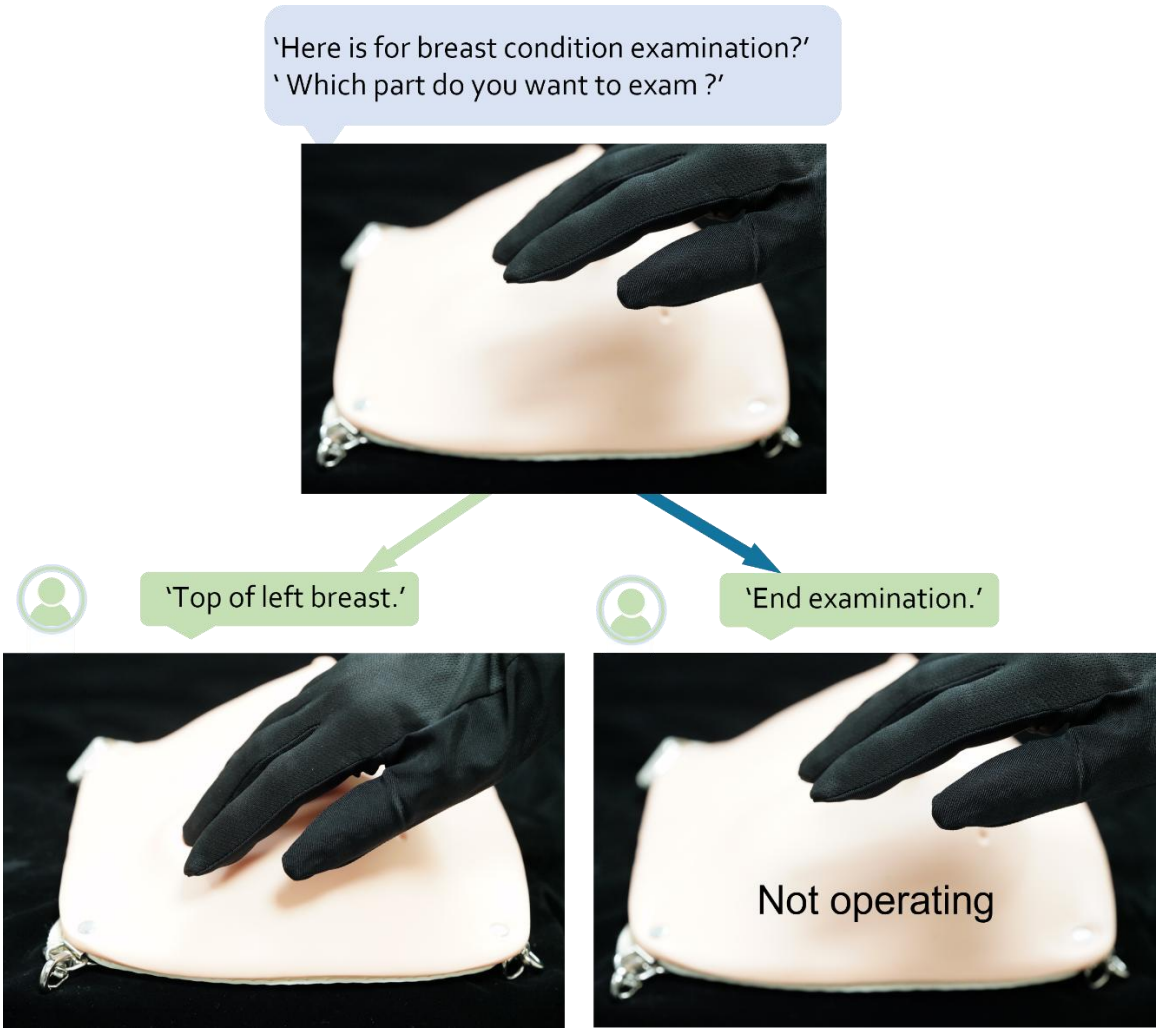

Figure 6.3 ChatGPT as a trigger for guidance of interactive diagnostics

References

[1] Babalola SA, Mishra D, Dutta S and Murmu NC. *Computers in Industry*. **2023**, 148, 103891.

[2] Rebergue G, Blaysat B, Chanal H and Duc E. *Measurement.* **2022**, 187, 110301.

[3] Tian D, Chen W, Xu D, Xu L, Xu G, Guo Y and Yao Y. *Computers in Biology and Medicine*. **2024**, 170, 108074.

[4] Eigenschink M, Dearing L, Dablander TE, Maier J and Sitte HH. *Wiener klinische Wochenschrift.* **2020**, 132, 260.

[5] Moir FC. *Chinese Medicine and Culture.* **2024**, 7,